PROTON-DEUTERON ELASTIC SCATTERING AT VERY LOW ENERGY

by

Timothy Charles Black

A dissertation submitted to the faculty of the University of North Carolina at Chapel Hill in partial fulfullment of the requirements for the degree of Doctor of Philosophy in the Department of Physics.

Chapel Hill

1995

Approved by

E. J. Ludwig
Advisor

W. J. Thompson
Reader

Hugas J. Karwowski
Reader

TIMOTHY CHARLES BLACK. Proton–deuteron elastic scattering at very low energy (under the direction of Edward J. Ludwig).

ABSTRACT

Contemporary nuclear theory is unable to furnish an adequate quantitative description of the three-nucleon system. The non-relativistic, nucleons-only dynamical theory—whether utilizing dispersion-theoretic, meson field-theoretic, or phenomenologically derived nuclear potentials—fails to replicate the trinucleon binding energies without the inclusion of three-body forces characterized by ad hoc parameters. Attempts to replicate three-nucleon continuum observables below the deuteron breakup threshold have been fairly successful in the case of the n–d system, but significant failures have attended these attempts for the p–d scattering system. The most serious such failure is a discrepancy between the theoretical and phenomenological values of the p–d S-wave scattering lengths. Besides suggesting the existence of subtle interactions between the nuclear and electrostatic forces in the three-body system, this discrepancy has challenged a long-held, though as yet incompletely understood, assumption that approximately linear correlations exist between the trinucleon binding energy and various parameters characterizing the three-nucleon system.

A consensus has emerged among theorists that these discrepancies are the result of a singularity in the doublet S-wave effective range function near the two-body threshold that hinders the ability to infer the scattering length on the basis of measurements made at excessively high scattering energies. Since the doublet and quartet S-wave eigenphaseshifts are coupled in the cross section, errors in inferring the former are reflected in erroneous determinations of the latter. Relative differential cross sections for the $^{2}H(p,p)^{2}H$ reaction have been measured at a number of (center-of-mass) angles between 36.9° and 140.5° at a proton laboratory energy of 315 keV. These data are part of a larger set that also includes measurements of the relative cross section at 240 keV. The data are compared with theoretical calculations of the cross sections that explore the influence of various partial wave eigenphaseshifts and spin mixing parameters, preparatory to a global phase shift analysis being undertaken by the author and his collaborators.

ACKNOWLEDGEMENTS

My advisor, Professor Edward Ludwig, has surely served above and beyond the call of duty. I have been a rebellious, unruly and arrogant graduate student and Professor Ludwig's patient and persistent guidance have revealed him to be nearly as talented a psychologist as he is a physicist. I owe special gratitude to Professor Hugon Karwowski for sharing his mastery of experimental technique with me and for providing encouragement to my creative impulses. His humor, spirit, warmth and generosity have given me pleasure and inspiration in equal measure. Both Dr. Ludwig and Dr. Karwowski have led from the trenches, devoting uncounted hours in the control room to this experiment. I thank Professor William Thompson for his wise counsel. His erudite wit (and witty erudition) have simultaneously entertained and humbled me.

Professor James York and Professor Y. Jack Ng of UNC-Chapel Hill and Professor Mark Silverman of Trinity College are heroic teachers who, in sharing with me some part of their scientific vision, have given me a gift of inestimable value. I will be forever grateful to Professors Paul Hubbard and Vic Briscoe for their kindness to me in the darkest moments of this journey. Professors Werner Tornow and Calvin Howell of Duke University have generously given of their expertise in the field of few-nucleon physics.

A number of graduate students and postdocs have devoted their toil and talent to bring this work to fruition; Dr. Eric Crosson, Dr. Rupak Das, Dr. Zeid Ayer, Dr. Beata Kozlowska, Dr. Kurt Fletcher, Dr. Jeff Blackmon, Lijun Ma, Kevin Veal, Bill Giest and Brian Hendrix have given much of themselves, both personally and professionally. Daniel Kozlowski provided important assistance with the design of some of the instruments.

I have benefited greatly from the skill of the craftsmen of the UNC-Chapel Hill and Duke University Instrument shops; Hal Mann, Bo Sanford, Harold Ellis, the late Dave Lashley, and Paul Hogan made

especially important contributions to this project. Paul Carter not only possesses a (possibly magical) ability to make things that don't work, or shouldn't work, to work but he is a funny and kind man of rare personality. I am also grateful to John Dunham and Richard O'Quinn for their technical expertise delivered night or day at no extra charge. Sidney Edward's "one-ness" with electronic life-forms is truly awesome, as is his unnaturally sunny demeanor.

So many friends in high, low and in-between places have given me a place in their hearts that I can only fathom it by believing that, as Maria says in *The Sound of Music* , "...I must have done something good." I also want to thank God for giving me such gifts as I have and for keeping faith with me. I owe debts to my parents, James and Elizabeth Black, that I can never repay in a dozen lifetimes. They have nurtured me, loved me and supported me in all my varied ventures. I hope they are as proud of me as I am of them. My wife Lynn has been extravagantly patient with me and my career and I owe her special thanks. Finally, I want to thank my beloved and darling children, Chelsea and Kevin, for sharing their Daddy with his work and for making the world such a beautiful place for me to live in.

TABLE OF CONTENTS

LIST OF TABLES

LIST OF FIGURES

Chapter I: The Proton–Deuteron Effective Range Parameters

"Now I re-examine philosophies and religions,
They may prove well in lecture rooms, yet not prove at all under the
spacious clouds and along the landscape and flowing currents."
Walt Whitman

1.1.1 Parametric descriptions of nuclear dynamics

Despite the complexity of the nuclear interaction, in many instances the essential characteristics of a nuclear scattering system can be synopsized by a relatively small number of parameters. Parametric descriptions of nuclear reactions may serve many purposes. They provide a basis for organizing phenomenological information. They furnish benchmarks against which theoretical models can be tested. Descriptions of this type are especially useful when some physical picture can be associated with the parameters, at least in an approximate fashion: Rather than attempting to hold in one's mind the complex interplay of nuclear interactions, one can contemplate their combined influence only as it manifests itself in the model parameters.

One parametric model that has proven especially useful in the study of nuclear reactions at low energies is the effective range expansion. This model provides a means of parametrizing the energy dependence of the S-matrix, or scattering matrix, of a particular reaction channel. In some instances, one can assign a simple physical interpretation to these parameters, but whether or not this is the case, the effective range expansion retains the distinct virtue of efficiently encapsulating the leading-order dynamics of a scattering system.

The object of this experiment is to determine the lowest-order effective range parameters for the proton-deuteron elastic scattering system. This system is simple in many ways. There are only two particles in the incident and outgoing channels. All particles are energetically stable. The relevant kinetic energies are small enough that non-relativistic quantum mechanics adequately describes the reaction dynamics. But because the nuclear Hamiltonian couples different spin and orbital angular momentum components of the asymptotic scattering states, the elementary single-channel scattering theory is inadequate to describe this reaction: one is compelled to express the dynamical problem in terms of the multichannel scattering theory.

The presence of long-range electrodynamic forces that cannot naturally be described within the framework of standard scattering theory further complicates the analysis of this reaction. Well-known modifications to the formal theory permit the extraction of parametric information regarding effectively two-body nuclear dynamics when Coulomb forces act between the charge centers of the reaction products. This modified theory is sufficient so long as the internal coordinates of the interacting particles do not depend asymptotically upon any long-range forces.

But although the asymptotic scattering state consists of only two fragments, inert with respect to nuclear forces, the repulsion between the two protons couples the short-range neutron-proton interaction to the long-range proton-proton interaction. The result is a long-range polarization potential which distorts the deuteron internal wavefunction in the asymptotic region. The polarization potential raises some important questions about the interpretation of proton-deuteron scattering at low energy. Do the calculated and phenomenologically-extracted effective range parameters measure the same thing? Is the modified effective range theory computationally tractable and possessed of the quality of parametric efficiency that, in the elementary theory, is its principle merit? It will be seen that the answer to both of these questions is a qualified yes.

A complete treatment of effective range theory, one that accounts for the multichannel aspects of the p–d scattering system as well as the modifications induced by the inclusion of long-range interactions, will be deferred to the next chapter. In order to give concrete form to the issues discussed in this chapter, however, in the following section I describe the effective range formalism as it applies to the elementary case of two-body quantum scattering through a short-range, central potential. Many, though not necessarily all, of the mathematical results of this theory can be taken over to the more realistic case of multichannel scattering. Nonetheless, one should bear in mind that the heuristic rationale for many results of the single-channel theory are not applicable to the theory of multichannel processes, even where the results themselves may be identical.

1.1.2 Elementary formulation of the single channel effective range function

If the interaction does not couple different spin and orbital angular momentum states, then the Schrödinger equation is separable in spherical coordinates. One can individually consider the reduced radial Schrödinger equation for each orbital angular momentum partial wave [New82].

In the absence of long-range interactions, the solution to the reduced radial Schrödinger equation for a given partial wave ℓ is a superposition of the solutions to the free-field Schrödinger equation that are regular and irregular at the origin:

$$u_\ell(k) \sim A_\ell(k)G_\ell(kr) + B_\ell(k)F_\ell(kr)$$

where $F_\ell(kr)$ is the regular free-field solution and $G_\ell(kr)$ is the irregular free-field solution. Because the $\mathcal{S}$-matrix is assumed to satisfy elastic unitarity[1], the scattering wavefunction in the asymptotic region has the form

---

[1] The complete scattering operator is unitary for all "time-independent" Hamiltonians. Violation of probability flux conservation is sometimes introduced as a formal device within a

$$u_\ell(k) \sim \exp(i\delta_\ell(k))\left[\sin\delta_\ell(k)G_\ell(kr) + \cos\delta_\ell(k)F_\ell(kr)\right] \qquad (1.1)$$

where $\delta_\ell(k)$ is a real angle called the nuclear phase shift [Lan90]. All of the information that a scattering experiment undertaken at a given energy can provide regarding the nuclear interaction is epitomized by some finite collection of the partial wave phase shifts.

If only short-range forces are present, the effective range function $K_\ell(k)$ for the ℓ^{th} partial wave is defined by

$$K_\ell(k) = k^{2\ell+1}\cot(\delta_\ell(k)). \qquad (1.2)$$

If Coulomb repulsion also acts between the two scattering bodies, one has instead the Coulomb modified effective range function [Eyr77],

$$K_\ell(k) = C_\ell^2(\eta)k^{2\ell+1}\left(\cot(\delta_\ell(k)) + \frac{2\eta h(\eta)}{C_0^2}\right) \qquad (1.3)$$

where the Coulomb penetrability factor is given by

$$C_\ell^2(\eta) = C_{\ell-1}^2(\eta)\left[1 + \left(\frac{\eta}{\ell}\right)^2\right],$$

with

$$C_0^2(\eta) = \frac{2\pi\eta}{\exp(2\pi\eta) - 1}.$$

The auxiliary Coulomb function, $h(\eta)$, is given by

---

particular reaction channel, even though the complete scattering operator is unitary. Elastic unitarity is more restrictive, implying that each open reaction channel rigorously conserves probability. In this section, the normalization of [Lan90] is used.

$$h(\eta) = -\ln(\eta) + \mathrm{Re}\{\psi(1 + i\eta)\},$$

where ψ is the digamma function and

$$\eta = \frac{Z_1 Z_2 e^2 \mu}{\hbar^2 k}$$

is the usual Coulomb parameter. Since the Coulomb interaction has infinite range, the total scattering phase shift never converges to a unique value for any radial separation of the scattering centers. The Coulomb modified nuclear phase shift instead measures the total scattering phase shift *relative* to the Coulomb phase shift.

1.1.3 The interpretation of the effective range parameters in the case of point particles scattering through a short-range central potential

The standard effective range expansion, valid for a wide range of short-range potentials between point particles, is a series expansion in k^2 about the channel threshold [Bla49]:

$$K_\ell(k) \approx -\frac{1}{a_\ell} + \frac{r_\ell k^2}{2} + P_\ell k^4 + \cdots \qquad (1.4)$$

The parameter a_ℓ is called the scattering length. The Taylor coefficient of the second term, r_ℓ, is denoted the effective range parameter, while the factor appearing in the third term, P_ℓ, is sometimes referred to as the first "shape-dependent" parameter of the expansion. Truncation of the series following the first two terms results in the so-called "shape-independent" expansion.

The shape-independent effective range expansion, first derived upon a semi-empirical basis by Landau and Smorodinsky [Lan44] and

later rigorously demonstrated by Schwinger[2] using his variational method, was originally developed as an analytic tool to exploit a striking feature of low-energy, ($E_N \leq 10$ MeV), neutron-proton scattering [Bla49]:

> ". . . *except for unusual well shapes likely to be excluded by other considerations, the experimental data about the neutron-proton system at very low energies tell us nothing at all about the shape of the nuclear potential well.*" [3]

Similar conclusions regarding proton-proton scattering made it clear that the low-energy nucleon-nucleon scattering observables depended upon no more than two parameters of the nucleon-nucleon potential—its strength and its "range", the latter being suitably defined. It was shown that the two parameters of the shape-independent effective range expansion completely characterized all "reasonable" potential models[4].

The fact that the effective range expansion converges very rapidly in k^2 is its most salient feature. There are many definite parity functions, analytic over some reasonably extended domain about the channel threshold, that characterize the scattering: the phase shift itself is an example. Because of its origin in the variational principle, however, the effective range expansion is guaranteed to be accurate to second order—the scattering length and effective range are uniquely characteristic of the

---

2 Apparently Dr. Schwinger never published this work. It was promulgated by means of his lectures at Harvard University and, in addition, was reported at a conference [Sch47]. The theoretical sections of [Bla49] constitute a report of Schwinger's work.

3 The italics appear in the original.

4 The requirements on the potential stated in [Bla49] are somewhat vague. It is presumed that the wavefunction vanishes at the origin, which implies an infinitely repulsive core. It is explicitly required that the potential be central. Furthermore, the authors require that the effective range, as defined by their equation 3.9, be finite. This requirement seems to be equivalent to the condition that the zero-energy radial wavefunction converge to a linear form; i.e., that $u(k=0) \sim 1 - \alpha r$ for some constant α, in the limit that $r \gg b$, for finite b. This would seem, in turn, to be included in the definition of a "scattering system" as defined by [New82]. In this latter reference, rigorous requirements on the potential for fulfilling this constraint are enumerated.

leading-order dynamics of the scattering system, at least in the elementary case. If only two parameters are necessary to characterize these dynamics, then the scattering length and effective range parameter indeed completely describe the scattering system. In the case of nucleon-nucleon scattering, "shape-independence" is a reflection of the dominance of pion exchange at low energies. For more complex systems, shape-independence may or may not be a good approximation.

For S-wave scattering, it is fairly easy to interpret the physical meaning of the effective range parameters. Suppose that the potential does not permit zero-energy resonances or bound states, so that the scattering length is finite. Combining equations (1.2) and (1.4), one has

$$\frac{\exp(2i\delta_0(k)) - 1}{2ik} = \frac{1}{k\cot\delta_0(k) - ik}$$

$$= -a_0 + ik(a_0)^2 - \frac{(a_0)^2 r_0 k^2}{2} + (a_0)^3 k^2 + O(k^3). \quad (1.5)$$

according to which

$$a_0 = -\lim_{k\to+0}\left\{\frac{\exp(2i\delta_0(k)) - 1}{2ik}\right\}.$$

If we assume that $\lim_{k\to+0}\left\{\frac{\exp(2i\delta_\ell(k)) - 1}{2ik}\right\} = 0$ for all $\ell \neq 0$, then it follows that the zero-energy angle-integrated cross section is given by

$$\sigma_{tot}(k=0) = 4\pi a_0^2 .$$

The scattering length is thus primarily a measure of the strength of the interaction.

It is generally understood that the $\ell = 0$ effective range parameter r_0 provides, in some sense, a measure of the intrinsic range of the

scattering potential. For the square well potential, the identification can be made exact. Given a square well of strength $-V_0$ and range R_0, the scattering length is

$$a_0 = R_0 - \frac{\tan(R_0\sqrt{V_0})}{\sqrt{V_0}}$$

and the effective range parameter is

$$r_0 = R_0\left\{1 - \frac{(R_0\sqrt{V_0})^3 + 3\left[R_0\sqrt{V_0} - \tan(R_0\sqrt{V_0})\right]}{3R_0\sqrt{V_0}\left[R_0\sqrt{V_0} - \tan(R_0\sqrt{V_0})\right]}\right\}.$$

Then $r_0 = R_0$ if and only if $R_0\sqrt{V_0} = \frac{(2n+1)\pi}{2}$ for integral n, which is just the requirement for a zero-energy resonance [Alb83].

In general, however, the effective range parameter is *not* equal to the intrinsic range of a potential which yields a finite scattering length. In fact, for an arbitrary choice of R_0 and V_0, r_0 is not necessarily positive. For example, if the square well potential parameters are such that $R_0\sqrt{V_0} = \pi$, then

$$r_0 = R_0\left(1 - \frac{\pi^2}{3} - \frac{1}{\pi}\right) \approx -\frac{7R_0}{3}.$$

Blatt and Jackson proposed to *define* the intrinsic range of a potential as the effective range parameter of that potential, after adjusting the potential strength to yield the first zero-energy resonance [Bla49], thereby making the intrinsic range a measure of some standard effective range parameter, rather than the reverse. This is sensible—the effective range parameter, unlike the intrinsic range of a generic potential, has an unambiguous meaning.

1.1.4 Non-central potentials, composite systems and Coulomb forces

Realistic nuclear interactions couple different spin and orbital angular momentum quantum states while preserving parity and total angular momentum. It will be shown that the single channel effective range theory can be modified to handle multichannel scattering systems of this type. In the multichannel theory, the S-matrix and by extension, the effective range matrix, can be *formally* factored by means of an orthogonal transformation into spin/orbital angular momentum preserving and spin/orbital angular momentum changing operators in such a way that the spin/orbital angular momentum preserving components of the S-matrix are described in terms of the real parameters ${}^{2S+1}\delta^{j}_{\ell}(k)$, called eigenphaseshifts [New82].

The effective range function of the single channel theory can then be formally regarded as the representation of an effective range matrix element which is diagonal in the angular momentum and channel spin. One defines the multichannel effective range function by

$$ {}^{2S+1}K^{j}_{\ell}(k) = k^{2\ell+1}\cot({}^{2S+1}\delta^{j}_{\ell}(k)) \qquad (1.6) $$

where the channel spin S, the orbital angular momentum ℓ, and the total angular momentum j completely label the quantum state.

The eigenphaseshifts of the multichannel theory are not generally equivalent to the phase shifts of single-channel theory[5]. Instead, they are the single-channel phase shifts of an imaginary quantum system in which the spin and orbital angular momentum are good quantum numbers. The eigenphaseshift representation of the scattering matrix must also be supplemented by a set of dynamical parameters, called mixing parameters

---

5 For nucleon-nucleon scattering, the assumption that higher partial waves are suppressed at sufficiently low energies is rigorously true. At sufficiently low energy, the separate spin states couple to states of distinct total angular momentum and therefore the eigenphaseshifts and the "physical" phase shifts are identical in this case.

or mixing angles, which describe those components of the scattering matrix that do not preserve the spin and orbital angular momentum.

The effective range expansion for the quantum state labeled by channel spin S, orbital angular momentum ℓ and total momentum j is just

$$
\begin{aligned}
{}^{2S+1}K^{j}_{\ell}(k) &= k^{2\ell+1}\cot({}^{2S+1}\delta^{j}_{\ell}(k)) \\
&\approx -\frac{1}{{}^{2S+1}a^{j}_{\ell}} + \frac{{}^{2S+1}r^{j}_{\ell}k^{2}}{2} + {}^{2S+1}P^{j}_{\ell}k^{4} . \qquad (1.7)
\end{aligned}
$$

A simple interpretation in terms of certain partial-wave amplitudes, analogous to equation (1.5), cannot be made for the multichannel effective range parameters—not even the S-wave parameters. Rather, the importance of the effective range expansion for the analysis of multi-channel scattering systems resides in its parametric economy.

Because the connection between the dynamical parameters and scattering observables is more complicated for multichannel scattering systems than for single channel scattering, the effective range expansion plays a more vital role in the comparison between theory and experiment for multichannel scattering. For single channel scattering, one can generally infer a unique set of phase shifts at a single energy from a relatively small complement of experimental data. As one introduces strong coupling between various amplitudes present in the asymptotic scattering states, it becomes increasingly difficult to make such inferences without conducting elaborate experiments involving both first and second order polarization observables. By using the effective range expansion to parametrize the energy dependence of the various spin and orbital angular momentum amplitudes, one imposes a strong set of constraints that may render the inferential problem tractable even if only limited experimental data is available. Whether a given set of data is adequate depends upon the dynamics of the nuclear system.

The Coulomb-modified effective range expansion in the eigenphaseshift model can be obtained by re-labeling equation (1.3) with the appropriate channel spin and orbital angular momentum quantum numbers:

$$ {}^{2S+1}K^{j}_{\ell}(k) = C^{2}_{\ell}(\eta)k^{2\ell+1}\left(\cot({}^{2S+1}\delta^{j}_{\ell}(k)) + \frac{2\eta h(\eta)}{C_0^2}\right) $$

$$ \approx -\frac{1}{{}^{2S+1}a^{j}_{\ell}} + \frac{{}^{2S+1}r^{j}_{\ell}k^{2}}{2} + {}^{2S+1}P^{j}_{\ell}k^{4}. \qquad (1.8) $$

1.2.1 Calculations of the S-wave effective range parameters

Within the past decade and a half, a number of theoretical groups working independently in a number of nations; Germany, Italy, Switzerland, the Russian Federation and the U.S.A.; have calculated the proton–deuteron low energy S-wave phase shifts and zero energy S-wave scattering lengths[6]. A variety of "exact" methods were used in these calculations including: solution of the Faddeev equations in configuration space by means of partial wave expansion and reduction of the integro-differential scattering equation to differential form at zero energy [Fri83, Fri84, Che86, Fri90, Che91] and at finite energies [Che89], solution of the AGS form of the Faddeev equations in momentum space [Ber86], solution of the Kohn variational equations for the Faddeev amplitudes as expanded in a basis of correlated hyperspherical harmonic functions [Kie94][7], and solution of the momentum space Faddeev equations with explicit renormalization of the singularities arising from both the Coulomb interaction and the deuteron electric polarizability [Kar90, Kar93].

---

6 Throughout this work, all energies are taken with respect to the p–d elastic threshold. Furthermore, all such energies are assumed to be below the deuteron breakup threshold. The unqualified term "threshold" refers to the elastic threshold.

7 The Kohn equations were also solved in [Che91], presumably using an uncorrelated basis. These were referred to in the text as "estimates".

Some of these results are reproduced in Table 1.1. Those values printed in boldface were obtained from potentials whose parameters were adjusted to reproduce either the tri-nucleon binding energy or the n–d doublet scattering length.

Table 1.1 Calculated p–d and n–d scattering lengths

Reference	Potential model	$^2a_{pd}$ (fm)	$^4a_{pd}$ (fm)	$^2a_{nd}$ (fm)	$^4a_{nd}$ (fm)
[Fri83]	Yukawa	-3.6	13.6	-2.1	6.39
	Exponential	-7.6	13.4	-6.4	6.33
	MT I–III	**0.15**	**13.8**	**0.70**	**6.44**
[Fri84]	RSC–5	2.23		1.76	
	AV14	1.42	13.57	1.35	6.38
	SSCC	1.35	13.67	1.32	6.41
	RSC–5/1.11V($^1S_0$)[8]	**0.06**		**0.60**	
[Che91]	RSC	1.569	13.550	1.520	6.302
	RSC/TM	-0.509	13.568	0.393	6.308
	AV14	0.967	13.764	1.200	6.372
	AV14+BR	-1.133	13.764	0.001	6.378
	RSC+TM	**≈ 0**	**13.52**	**0.66**	**6.30**
	AV14+BR	**≈ 0**	**13.76**	**0.57**	**6.38**
[Ber86]	Yamaguchi	0.257	13.68	0.656	6.27
[Che89]	MT I–III	**0.17**	**13.8**	**0.71**	**6.43**
[Kie94]	MT I-III	**0.003**	**13.96**	**0.702**	**6.442**
	AV14	0.954	13.779	1.196	6.380
[Kie95a]	AV14+BR	**–0.178**		**0.575**	
	AV18+UR IXb	**–0.022**		**0.626**	
[Kar93]	Yamaguchi	-0.1			

The spin-doublet n–d scattering lengths calculated with the adjusted potentials lie roughly between 0.6 and 0.7 fm. The p–d

8 For this potential model, the triplet S-wave potential has been adjusted so as to replicate the trinucleon binding energies.

scattering lengths obtained from the adjusted potentials cluster about 0 fm, with a spread of about ±0.2 fm. For both the n-d and the p-d systems, the calculated spin-quartet scattering lengths do not depend upon whether the potential replicates the trinucleon binding energy and are insensitive to the nuclear potential employed and the method used to perform the calculation. This lack of sensitivity reflects the repulsive character of the dominant single-nucleon exchange mechanism in the spin quartet state.

1.2.2 Experimentally derived scattering lengths

The accepted values for the experimental n–d S-wave scattering lengths are [Dil71]

$$^4a_{nd} = 6.35 \pm 0.02 \text{ fm}$$

and

$$^2a_{nd} = 0.65 \pm 0.04 \text{ fm},$$

which are in good agreement with the calculated values. The phase shift analysis from which these results were extracted entailed little ambiguity because it was possible to perform measurements of the spin-correlation coefficients very near to threshold using thermal neutrons. By contrast, the calculated proton-deuteron S-wave effective range parameters substantially disagree with the extant experimental results. The doublet and quartet scattering lengths obtained from phase shift analyses of the experimental data are shown in Table 1.2.

Table 1.2 Proton-deuteron scattering lengths extracted from experimental data

Analysis	$^2a_{pd}$ (fm)	$^4a_{pd}$ (fm)	Lowest energy data included in analysis
[Van67]	1.3 ± 0.2	11.4 + 1.8 – 1.2	1.510 MeV
[Arv74]	2.73 ± 0.10	11.88 + 0.4 – 0.1	1.000 MeV
[Hut83b]	4.0 + 1.0 – 0.67	11.11 + 0.25 – 0.24	0.400 MeV

Although inconsistent with the theoretical calculations, the quartet state experimental results are in fairly good agreement with one another. The doublet experimental results agree neither with the theory nor with one another. It is unclear whether the apparent historical trend toward larger scattering lengths—in the opposite direction from the theoretical predictions—which could be correlated with the inclusion of progressively lower energy data in the phase shift analysis, is meaningful or not.

The most recently reported experimental results date to 1983 [Hut83a, Hut83b]. The disagreement between these results and the calculations of [Fri83] and [Fri84] precipitated a flurry of speculation as to the nature of the problem. It was suggested, for instance, that the long-range electric polarization potential caused the usual Coulomb-modified scattering lengths to be infinite [Ber65]. This supposition was proved by Bencze and Chandler [Ben85], who thereupon introduced an alternate definition of the Coulomb-modified scattering length in the presence of the polarization potential and showed that the extant calculated results were numerically consistent with the revised definition [Ben87]. Except at very low energies, the effective range function calculated with and without the polarization potential should give nearly identical results. A number of calculations of the p–d scattering observables were undertaken in the late 1980's and early 90's, seeking to clarify the situation. By the turn of the decade, the theoretical consensus was that the experimental findings were in error.

1.3.1 S-wave doublet scattering and the "anomalous" effective range function

It was first proposed by Chen et. al. that the discrepancy may arise from the existence of a pole in the p–d S-wave doublet effective range function just below the two-body scattering threshold [Che89]. Hence, instead of the conventional expansion of the $\ell = 0$ effective range function given by equation (1.8), one has instead the parametric form

$$ {}^2K_0(k^2) = \frac{-\frac{1}{{}^2a_0} + \frac{{}^2r_0 k^2}{2} + {}^2P_0 k^4}{1 \pm \frac{k^2}{k_0^2}} , \qquad (1.9) $$

where the – or + sign in the numerator is used depending on whether the singularity lies in the physical or unphysical region of the complex k plane, respectively. If the analysis of the experimental data—obtained at small but finite energies—were undertaken without accounting for this singularity, then it would not be possible to correctly infer the scattering length. This was not a completely surprising development: The n–d S-wave doublet effective range parameter is known to exhibit a sub-threshold simple pole singularity [Del60, Rei69, Adh82], and the possibility of an analogous singularity in the p–d S-wave doublet effective range function was numerically tested and rejected by the authors of [Hut83b] in the course of their phase shift analysis. Nonetheless, the conjecture that the p–d S-wave spin doublet effective range function has the form given by equation (1.9) has been endorsed by other theorists [Kar93, Kie94] and is consistent with the numerical results of [Ber86, Eyr77, Tom87] and most recently, a series of calculations undertaken by A. Kievsky et. al. [Kie95a, Kie95b].

A simple pole in the effective range function does not imply the existence of some bizarre physical phenomenon. Such a pole will exist wherever the eigenphaseshift vanishes at some point in the complex plane other than at the origin[9]. It is easy to see how this leads to the anomalous effective range expansion of equation (1.9). The effective range expansion has the mathematical form of a Taylor series expansion in k^2 about $k = 0$ in the complex momentum plane[10]. Within this radius of convergence, it will *always* have the standard form given by equation

---

9 Being an odd function of the momentum, the eigenphaseshift always vanishes at the origin.

10 A discussion of the analytic properties of the phenomenological S-matrix and the effective range matrix, along with an investigation of the significance of the "anomalous effective range" represented by equation 1.9, will be presented in the second chapter.

(1.7) or (1.8) for short-range or Coulomb-modified short-range interactions respectively. If the eigenphaseshift in a given channel vanishes for some non-zero value of k, then the effective range function for that channel will be singular there. The smallest absolute value of |k| for which the effective range function becomes singular defines the radius of convergence of the Taylor series (1.7) and (1.8). It may happen that the phase shift vanishes for some very small |k|, so that the radius of convergence is too small for the Taylor series expansion to be a useful parametric representation of the available experimental data. The radius of convergence can be extended by re-formulating the Taylor series as a Frobenius-type series expansion, obtained by explicitly dividing out the pole. The order of the pole depends upon how quickly the phase shift vanishes at the singular point.

The p–d spin doublet effective range functions predicted in [Hut83b] and [Arv74] on the basis of experimental data are shown in Figure 1.1 along with the effective range functions calculated in [Che89] and [Ber86]. The "data points" shown in the figure are located at energies where cross section data were measured. The error bars reflect the reported uncertainties in the effective range fits. Note that linear forms[11] for the energy dependence of the experimental effective range functions were *assumed*. The authors of both [Hut83b] and [Arv74] attempted to fit the data to singular expansions of the form given by equation (1.9), but in each case believed that the result was inconclusive.

Huttel, et. al. noted that in case one chooses the pole parameter $k_0^2 < 0.05$ fm^{-2}, the χ^2 increased considerably. If it was chosen so that $k_0^2 > 0.05$ fm^{-2}, then the χ^2 is unchanged, since the effect of the pole and the consequent small scattering length is compensated by an increase in the effective range parameter r_0. The authors of [Hut83b] therefore concluded that the pole parameter k_0^2 was almost certainly larger that 0.05 fm^{-2}, basing this conclusion on the large χ^2 obtained for smaller values of k_0^2. They were further influenced by the calculations of [Eyr77], who

---

[11] In the case of the Arvieux analysis, a second order polynomial form was assumed.

found $k_0^2 = 0.0842\ fm^{-2}$. Finally, it was remarked that a Taylor series expansion for $k < k_0$ leads to a conventional form of the expansion, thereby explaining the insensitivity of χ^2 to the selection of pole parameters $k_0^2 > 0.05\ fm^{-2}$. This last comment is trivially true for some value of k_0^2. Within the radius of convergence; that is, for $k < k_0$, the effective range expansion naturally has the conventional form. Undoubtedly k_0^2 is finite, but how small is it?

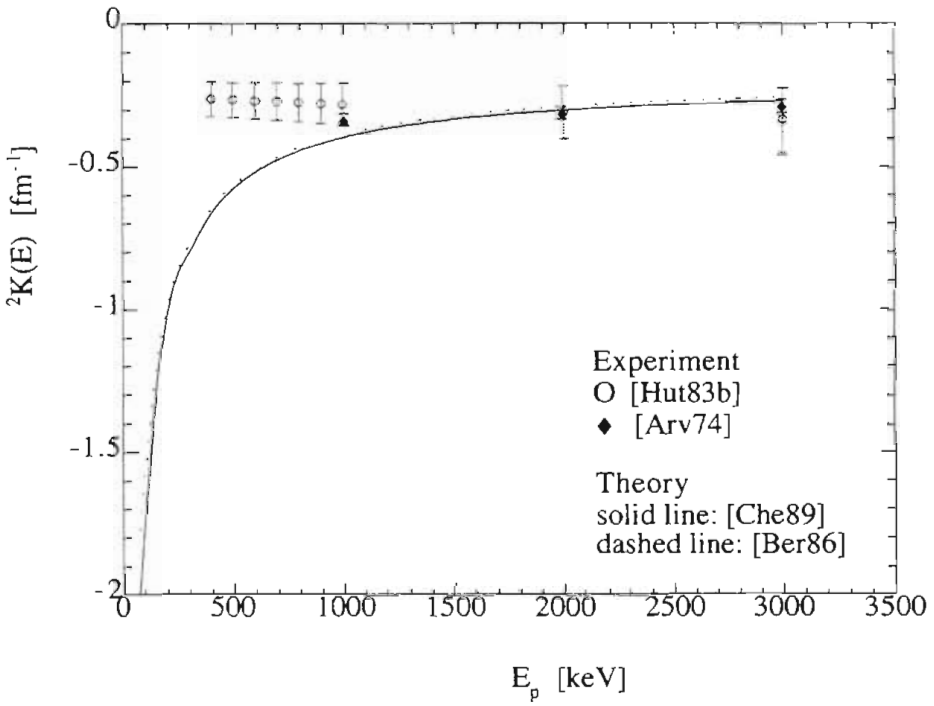

Figure 1.1 Calculated effective range functions from [Che89] and [Ber86] juxtaposed with the experimentally derived effective range expansions of [Hut83b] and [Arv74].

If equation 1.9 is expanded about $\frac{k_0^2}{k^2} = 0$, one has

$$\frac{c_0 + c_1 k^2 + c_2 k^4}{1 + \frac{k^2}{k_0^2}} \approx C_{(-6)} k^{-6} + C_{(-4)} k^{-4} + C_{(-2)} k^{-2} + C_{(0)} + C_{(2)} k^2 + \ldots \quad (1.10)$$

where the scattering length is $a_0 = -\frac{1}{c_0}$, the effective range parameter is $r_0 = 2c_1$, and the coefficients $C_{(n)}$ are

$$C_{(-6)} = k_0^6 c_0$$

$$C_{(-4)} = k_0^6 c_1 - k_0^4 c_0$$

$$C_{(-2)} = k_0^6 c_2 - k_0^4 c_1 + k_0^2 c_0$$

$$C_{(0)} = k_0^2 c_1 - k_0^4 c_2$$

$$C_{(2)} = k_0^2 c_2$$

This expansion is appropriate if the data under consideration were measured at energies much greater than that corresponding to the pole parameter.

Figure 1.2 shows the calculated proton-deuteron doublet S-wave effective range function of [Che89], fitted to an anomalous effective range expansion form. The pole location corresponds to a proton energy of roughly 35 keV. The lowest energy data included in the analysis of [Hut83b] was obtained at 400 keV: at this energy, $\frac{k_0^2}{k^2} \approx 0.0865$. If one attempted to fit the curve of Figure 1.2 to a linear form, which is tantamount to neglecting the first three terms of equation (1.10), one would obtain a constant term of $C_{(0)} = -0.209$, which corresponds to a

scattering length of $a_0 = 4.77$ fm. This value is consistent, within the quoted uncertainty, with the scattering length obtained by [Hut83b].

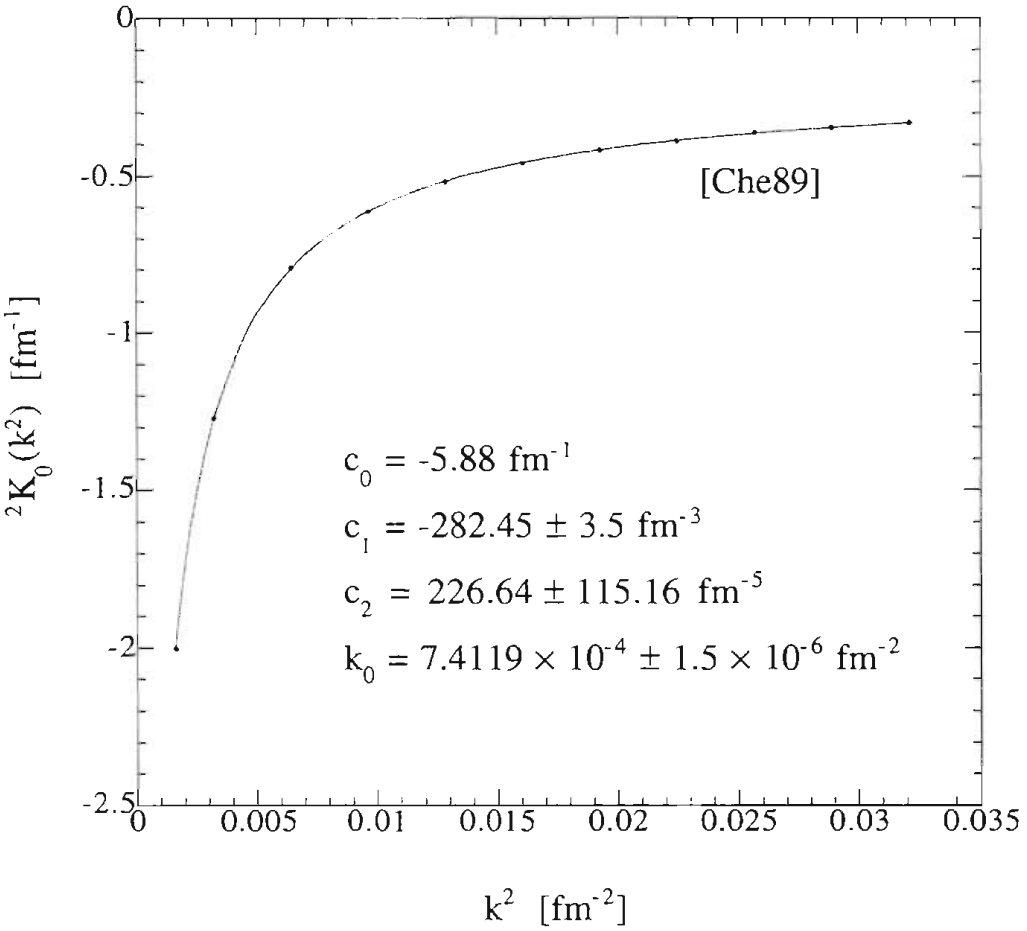

Figure 1.2 Proton-deuteron S-wave spin-doublet effective range function of [Che89] fit to the anomalous effective range expansion form

It should be noted, however, that the scattering length does not even appear in the expression for $C_{(0)}$. This term is in fact dominated by the effective range parameter. The leading contribution from the scattering length actually appears in the $C_{(-2)}$ term. At 400 keV, this term is larger than the $C_{(0)}$ term, but it may not have much influence in the overall fit because so much of the data was obtained at higher energies, where the $C_{(-2)}$ term is much smaller. This last fact constitutes the primary motivation for conducting this experiment—to obtain more data

at very low energies so that the contributions from the $C_{(-2)}$ and $C_{(-4)}$ terms manifest themselves more clearly.

In their attempt to fit the data to a singular form, the authors of [Hut83b] did not permit the pole position to vary freely; rather, the pole position was fixed at a number of points and the other parameters were optimized for each such value of the pole. It is very unlikely that this type of procedure would be successful in fitting the data. This is because the parameters in the expansion given by equation (1.9) are strongly correlated and are especially dependent upon the pole location. Only if one accidentally happened upon a very nearly correct value for the pole, would it be possible to obtain a reasonable set of phase shifts across the spectrum of energies employed in the analysis.

1.3.2 The S-wave spin quartet effective range function

The calculated and experimentally-extracted effective range functions for the spin-quartet channel, shown in Figure 1.3, manifest the same disagreement between theory and experiment as that seen in the doublet case. In this case, the mathematical form of the expansion is not at issue, only the values of the effective range parameters. Because the effective range parameters for the doublet and quartet channels inferred from any incomplete set of data are correlated, one expects that discrepancies in one channel will give rise to discrepancies in the other.

Even though transitions between the two states are forbidden, the doublet and quartet S-wave effective range parameters are correlated because both contribute substantially to the term in the differential cross section that has a constant angular distribution. Both also couple to D-waves. Furthermore, the S-wave amplitudes are strongly correlated with the P-wave amplitudes, since each contributes to the term in the cross section whose angular distribution is given by the $\ell=1$ Legendre polynomial. These contributions are negligible only if the P-wave amplitudes vanish strongly at low energies which, according to theoretical calculations, is not the case [Kie95b]. Errors in determining the P-wave and D-wave effective range parameters will therefore generate errors in determining the S-wave effective range parameters.

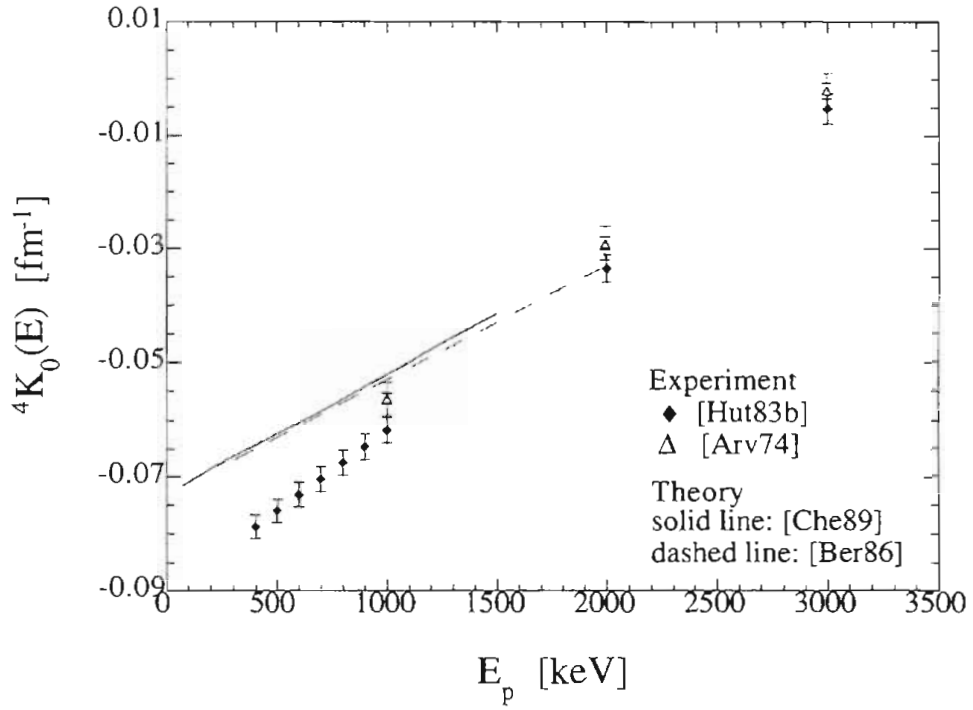

Figure 1.3 Calculated and experimentally derived effective range functions for the p–d S-wave spin quartet channel

Much of the information concerning the strength of the $\ell = 1, 2,$ and 3 partial waves comes from measurements of vector and tensor analyzing powers. These observables depend upon both the eigenphaseshifts for the relevant S-matrix element and the mixing parameters. The mixing parameters, like the effective range function, are even functions of the momentum k. It is assumed in [Hut83b] that these parameters vanish at the two-body threshold. The ε–parameters, which gauge mixing between different spin states having the same orbital angular momentum, cannot be required to vanish. The case of the threshold behavior of the other parameters is not so clear. At very low energies, the effective range expansion in the Coulomb system may be problematic for other reasons and so it is difficult to assess the relevance of results that strictly obtain only at zero energy. The approach to zero is more phenomenologically meaningful than the zero-energy result itself and rigid adherence to the latter may distort the former.

1.4.1 The plan of action

The scattering lengths reported by [Arv74], [Van67] and [Chr53] were determined by fitting the eigenphaseshifts extracted from phase shift analyses conducted at a number of different energies to the parametric form of the effective range expansion. The results obtained from phase shift analyses conducted at a single energy are ambiguous because in no case has a so-called "complete set of observables" been obtained at a single energy[12]. By contrast, the authors of [Hut83b] conducted the analysis directly in terms of the effective range parameters. Because the parametric effective range expansion strongly constrains the possible values of the phase shifts at any given energy, direct analysis of the entire data set in terms of the effective range parameters provides a more coherent means of inferring the effective range parameters than linking single-energy phase shift analyses.

- The analysis should be conducted by simultaneously fitting all of the available data, using the effective range expansion to parametrize the energy dependence of the eigenphaseshifts and mixing parameters.

The analysis of [Hut83b] was compromised by adopting incorrect assumptions regarding the energy dependence of the spin mixing parameters. Furthermore, in an attempt to reduce the scope of the analytic problem, the dependence of the eigenphases on the total momentum j was neglected for $\ell > 1$. Finally, the attempt to fit the data

---

12 A "complete set of observables" is one that, in principle, determines a unique solution. In the case of spin 1–spin 1/2 elastic scattering, no set is complete that does not include observation of second order polarization observables; e.g., spin transfer or spin correlation measurements. In real life, a minimally complete set of observables will yield a unique solution only if the data are infinitely accurate. A hyper-complete set of observables could, with data of finite accuracy, determine a bounded domain of parameter space that is unique in the sense that any other non-intersecting bounded domain of parameter space could be said **not** to be a solution. The most truthful thing to be said in this regard is that the more data of good accuracy you have, the more likely you are to infer the correct solution, all other things being equal. The whole notion of uniqueness is somewhat chimerical.

to the singular form of the effective range expansion did not permit the pole parameter to vary freely.

- The correct threshold behavior of the spin-mixing parameters should be used in the analysis. The energy dependence of the effective range and spin-mixing parameters are discussed more fully in the second chapter.

- The j-splitting of the phases should be accommodated, at least for the P and D-wave eigenphaseshifts and mixing parameters.

- When attempting to fit the data to the singular effective range expansion, the pole parameter should be allowed to vary freely over a reasonable range, using a high-resolution search grid. It is clear that such an analysis must rely heavily on theoretical guidance to constrain the regions of parameter space included in the search.

I have pointed out that under the hypothesis that the radius of convergence of the effective range expansion is very small relative to the typical energies at which the data was acquired, the highest order contribution of the scattering length to the effective range goes as k^{-2}. If the data set is dominated by measurements for which this term is negligible, then this term will exert only a very small influence.

- Measurements of the differential cross section at proton energies below 400 keV should be the principle aim of this experiment.

The following chapters detail the various means by which this plan of action has been implemented. In the next chapter, the elementary effective range theory presented at the beginning of this chapter is explored more deeply within the context of multichannel scattering theory. Chapter three details the experimental procedures developed and

utilized to acquire the data and chapter four describes the manner in which the data were analyzed and presents preliminary conclusions.

A great deal of effort has been expended in this attempt to resolve the discrepancy between the calculated and experimentally extracted values of the proton–deuteron S-wave effective range parameters. To the extent that we have been successful in this endeavor, I believe this effort to have been wisely invested. Understanding the interplay of long-range and short-range forces is of fundamental importance for developing a coherent, microscopic picture of systems in which nuclear and electrodynamic forces interact.

Chapter II: Effective Range Theory for Multichannel Scattering Systems

"Formal proofs of dispersion theories are like breasts on a man, they are neither useful nor ornamental."

Milton Goldberger

2.1.1 Constraints on the form of the $\mathcal{S}$-matrix

All of the dynamical information concerning a scattering system is encoded within the $\mathcal{S}$-matrix. To obtain a meaningful parameterization of the $\mathcal{S}$-matrix, it is necessary to invoke the symmetries which are known, or assumed, to be preserved by the nuclear interaction.

The nuclear interaction is assumed to be invariant with respect to time-translation, so that the $\mathcal{S}$-matrix is symmetric with respect to interchange of in and out states. The $\mathcal{S}$-matrix is unitary since, for arbitrary in and out states constructed from a complete asymptotic basis,

$$\left\langle \phi_{\beta,in} \left| \mathcal{S}^{\dagger} \mathcal{S} \phi_{\alpha,in} \right\rangle = \left\langle \phi_{\beta,out} \left| \phi_{\alpha,out} \right\rangle \right. = \delta_{\beta\alpha} \right.$$

Since the nuclear interaction is assumed to conserve parity and, absent external forces, the scattering system is invariant with respect to spatial rotations, the scattering sub-matrix for total angular momentum j and parity π can be written in the general form

$$\mathcal{S}^{j\pi}(k) = \mathcal{S}(\Lambda^{j\pi}(k)) = e^{2i\Lambda^{j\pi}(k)} \qquad (2.1)$$

where $\Lambda^{j\pi}(k)$ is a real, symmetric matrix [Bla52][13].

2.2.1 The eigenphaseshift transformation of the $\mathcal{S}$-matrix

Because they have different aims, theory and phenomenology impose different requirements upon the form of a solution to the scattering problem. Since present-day "exact" calculations of three-body scattering observables use nucleon-nucleon potentials as their dynamical input, the multichannel aspects of the scattering problem arising from the existence of particle degrees of freedom are salient features of the method of solution.

However many degrees of freedom are included in a theoretical calculation, of whatever type, they are not all necessarily phenomenologically relevant. Below the breakup-threshold, the wavefunction of the scattering system solves a set of coupled Schrödinger equations, with an effective two-body potential between the proton and deuteron. The phenomenological problem is always solved in this two-body Hilbert space[14]. The only relevant degrees of freedom are those appropriate to such a space; the coupled spin, the coupled orbital angular momentum, the coupled total momentum, and the relative momentum.

Because of the form of $\mathcal{S}^{j\pi}$, given in equation (2.1), it is possible to construct an "effective" single channel theory. One defines an orthogonal transformation of $\Lambda^{j\pi}$ so that the transformed matrix,

$$\Delta^{j\pi} = (\mathbf{T}\Lambda\mathbf{T}^{-1})^{j\pi},$$

is diagonal in the orbital angular momentum ℓ and spin s [Bla52]. Therefore,

---

13 It is assumed throughout that only two-body elastic channels are open.

14 It is assumed here that at sufficiently large separations, the intrinsic wavefunctions of both fragments are unaffected by the presence of one another.

$$\mathcal{S}^{j\pi}_{\beta\gamma}(k) = \left(\exp(2i\Lambda^{j\pi})\right)_{\beta\gamma} = \exp(2iT^{-1}_{\beta\alpha}\Delta^{j\pi}_{\alpha}\, T_{\alpha\gamma})$$

$$= T^{-1}_{\beta\alpha}\exp(2i\Delta^{j\pi}_{\alpha})T_{\alpha\gamma}, \qquad (2.2)$$

where the superscripts indicating that $T_{\mu\nu}$ depends upon the total angular momentum and the parity have been suppressed for clarity. The channel labels α, β and γ represent spins and orbital angular momenta, with $\beta = (\ell', s')$ and $\gamma = (\ell, s)$. The summation convention for repeated indices is assumed.

The parameters appearing in the diagonal matrix, $\Delta^{j\pi}_{\alpha}$, are real angles, termed eigenphaseshifts[15]. In the case of spin-$(1 \oplus \frac{1}{2})$ scattering, the transformation matrix $\mathbf{T}^{j\pi}$ can be taken as the product of three successive rotations [Sey69],

$$\mathbf{T}^{j\pi} = \mathbf{V}^{j\pi}\,\mathbf{W}^{j\pi}\,\mathbf{X}^{j\pi} \qquad (2.3)$$

where

$$\mathbf{V}^{j\pi} = \begin{pmatrix} 1 & 0 & 0 \\ 0 & \cos\varepsilon^{j\pi} & \sin\varepsilon^{j\pi} \\ 0 & -\sin\varepsilon^{j\pi} & \cos\varepsilon^{j\pi} \end{pmatrix},$$

$$\mathbf{W}^{j\pi} = \begin{pmatrix} \cos\zeta^{j\pi} & 0 & \sin\zeta^{j\pi} \\ 0 & 1 & 0 \\ -\sin\zeta^{j\pi} & 0 & \cos\zeta^{j\pi} \end{pmatrix},$$

and

---

15 Above the deuteron breakup threshold, the eigenphaseshifts are complex.

$$\mathbf{X}^{j\pi} = \begin{pmatrix} \cos\eta^{j\pi} & \sin\eta^{j\pi} & 0 \\ -\sin\eta^{j\pi} & \cos\eta^{j\pi} & 0 \\ 0 & 0 & 1 \end{pmatrix}.$$

The parameters ε, ζ and η are real angles, denoted spin mixing parameters. The ε-angle describes mixing between states of the same orbital angular momentum but different spin, the ζ-angle represents mixing between states having the same spins but different orbital angular momentum, and the η-angle mixes states whose orbital angular momentum and spin are both different.

2.2.2 Physical interpretation of the eigenphaseshift transformation

The scattering wavefunction in the asymptotic region, for a particular value of the total angular momentum j and angular momentum projection m, can be written in the form [Del58]

$$\Psi_{\infty}^{jm} = \sum_{\alpha} \psi_{\alpha}(r_{\alpha}) \frac{\varphi_{\alpha}}{r_{\alpha}} \mathcal{Y}_{\ell_{\alpha},s_{\alpha}}^{jm}(\theta,\phi) \qquad (2.4)$$

where r_{α} is the separation between the centers-of-mass of the scattering fragments, and

$$\mathcal{Y}_{\ell_{\alpha},s_{\alpha}}^{jm}(\theta,\phi) = \sum_{\mu,\nu} i^{\ell} C(s\ \ell\ j;\ \nu\ \mu\ m)\ Y_{\ell,\mu}(\theta,\phi)\ \chi_{s,\nu} \qquad (2.5)$$

is the coupled spin–orbital angular momentum wavefunction of [Del58] and [New82][16].

---

16 The coupling order of ℓ and s is different than that given in [Del58] and [New82]. This may give rise to different phases for some terms, depending upon the values of ℓ, s and j for a given scattering system.

Under the assumption that any long-range forces act only between the centers-of-mass of the scattering fragments in the asymptotic region, the wavefunction of relative motion $\psi_\alpha(r_\alpha)$ is given by

$$\psi_\alpha(r_\alpha) = C_\alpha[A_\alpha F_{\ell_\alpha}(r_\alpha) - B_\alpha G_{\ell_\alpha}(r_\alpha)] , \qquad (2.6)$$

where C_α depends on the reduced mass of channel α and the channel wavenumber k_α. Explicit reference to the quantum labels j and π has been suppressed. $F_{\ell_\alpha}(r_\alpha)$ and $G_{\ell_\alpha}(r_\alpha)$ are the regular and irregular solutions of the asymptotic region Schrödinger equation, respectively, defined as in [Lan58].

The channel labels α represent the triplet (ℓ, s, ρ), where ℓ and s are the channel orbital angular momentum and channel spin, respectively, and ρ signifies a particular quantum state of φ_α, which is the product of the intrinsic wavefunctions of the two fragments in the asymptotic channel labeled by α. One can define a single channel ρ that corresponds to a "real" deuteron—a mixture of S and D waves—and this is the standard interpretation of the mixing parameters extracted from phenomenology. However, this means that it cannot be assumed that the η and ζ mixing parameters vanish at threshold, which is the case for n–p or p–p scattering, for instance. The difference is that, for N-N scattering, the channel orbital angular momentum is completely characterized by the relative orbital angular momentum; there is no ℓ-mixing between the wavefunction of relative motion and the intrinsic wavefunction.

The sets of coefficients {A} and {B} for the various channels are related by the S-matrix:

$$B_\beta = \sum_\alpha S_{\beta\alpha} A_\alpha \qquad (2.7)$$

For single-channel scattering, discussed in chapter 1, the partial wave expansion yields a scattering matrix having the form

$$S_{\beta\alpha} = \begin{cases} \exp(2i\delta_{\ell_\alpha}) & \text{if } \beta = \alpha \\ 0 & \text{if } \beta \neq \alpha \end{cases} .$$

In this case, equation (2.6) becomes

$$\psi_\alpha(r_\alpha) = C_\alpha A_\alpha [F_{\ell_\alpha}(r_\alpha) - \exp(2i\delta_{\ell_\alpha}) G_{\ell_\alpha}(r_\alpha)] , \qquad (2.8)$$

In the general case of multichannel scattering, the scattering matrix has the form

$$S_{\beta\alpha} = \sum_{\mu,\nu} T^{-1}_{\beta\mu} \exp(2i\Delta_{\mu\nu}) T_{\nu\alpha} = \sum_{\mu,\nu} T_{\mu\beta} \exp(2i\Delta_\mu) \delta_{\mu\nu} T_{\nu\alpha} \qquad (2.9)$$

where $\delta_{\mu\nu}$ in equation (2.8) is the Kronecker delta function. Use has been made of the fact that **T** is an orthogonal transformation, so that $\mathbf{T}^{-1} = \mathbf{T}^\dagger = \mathbf{T}^T$. Substitution of (2.7) and (2.9) into equation (2.6) gives

$$\psi_\alpha(r_\alpha) = C_\alpha \left\{ A_\alpha F_{\ell_\alpha}(r_\alpha) - \left[\sum_{\beta,\mu,\nu} T_{\mu\alpha} \exp(2i\Delta_\mu) \delta_{\mu\nu} T_{\nu\beta} A_\beta \right] G_{\ell_\alpha}(r_\alpha) \right\} \qquad (2.10)$$

If the $T_{\beta\alpha} = \delta_{\beta\alpha}$, then the relative motion wavefunction reduces to the form of equation (2.8). This form is the same as that of the single-channel case, except that the eigenphaseshift is labeled by the complete channel label α, rather than solely by the orbital angular momentum for channel α: this reflects the fact that the potential may also depend upon the spin. An S-wave potential necessarily has this form, since different spin states couple to different values of the total angular momentum. Therefore, calculations performed using S-wave potentials always yield a mathematical form for the relative-motion wavefunction, and hence for the effective range expansion, that is identical to that of single-channel S-wave scattering. That being the case, the interpretation of the effective range parameters for multichannel S-wave scattering, or for any scattering system in which mixing between

channels is forbidden, is the same as the interpretation given in chapter 1 for the case of single-channel scattering.

If however, the channels are coupled, so that $T_{\beta\alpha} \neq \delta_{\beta\alpha}$, the interpretation is more complicated. The scattering matrix is diagonalized by the transformation

$$\tilde{\mathcal{S}} = \mathbf{T}\mathcal{S}\mathbf{T}^{-1} .$$

It therefore follows that the columns of $\mathbf{T}^{-1}$, (or the rows of $\mathbf{T}$), are eigenstates of the scattering operator. One can therefore construct a state $\Psi^{(\gamma)}$ for which all of the amplitudes A_β are proportional to $T_{\gamma\beta}$:

$$A_\beta^{(\gamma)} = q^{(\gamma)} T_{\gamma\beta}$$

Such a state is an eigenstate of the scattering, since

$$B_\beta^{(\gamma)} = \mathcal{S}_{\beta\alpha} A_\alpha^{(\gamma)} = T_{\mu\beta} \exp(2i\Delta_\mu) \delta_{\mu\nu} T_{\nu\alpha} T_{\gamma\alpha} q^{(\gamma)}$$

$$= \exp(2i\Delta_\gamma) q^{(\gamma)} T_{\gamma\beta} = \exp(2i\Delta_\gamma) A_\beta^{(\gamma)}.$$

The relative-motion wavefunction, labeled now by both α and γ, is then

$$[\psi_\alpha(r_\alpha)]^{(\gamma)} = C_\alpha A_\alpha^{(\gamma)} \{ F_{\ell_\alpha}(r_\alpha) - \exp(2i\Delta_\gamma) G_{\ell_\alpha}(r_\alpha) \}, \quad (2.11)$$

which has the same form as that of equation (2.8). Every channel α of the total wavefunction $\Psi^{(\gamma)}$ experiences a phase shift of Δ_γ. But Δ_γ is not the phase shift for the γ-channel. In general, a single phase shift for any such channel does not exist.

2.3.1 The effective range expansion and threshold behavior of the $T_{\beta\alpha}$

The reactance matrix $\mathcal{K}$ is a generalized collision matrix [Lan58] that is related to the scattering matrix by the Caley transformation [Tei52, New82]

$$\mathcal{S} = (\mathbf{I} + i\mathcal{K})(\mathbf{I} - i\mathcal{K})^{-1}, \tag{2.12}$$

so that

$$\mathcal{K} = i(\mathbf{I} - \mathcal{S})(\mathbf{I} + \mathcal{S})^{-1}. \tag{2.13}$$

It is easy to show that the same transformation that diagonalizes $\mathcal{S}$ also diagonalizes $\mathcal{K}$, and that the diagonal elements are given by

$$\tilde{\mathcal{K}}_{\beta\alpha} = \tan\Delta_\alpha \delta_{\beta\alpha},$$

where $\tilde{\mathcal{K}} = \mathbf{T}\mathcal{K}\mathbf{T}^{-1}$. One can also define a related matrix $\mathcal{M} = \mathcal{K}^{-1}$, whose diagonal elements are

$$\tilde{\mathcal{M}}_{\beta\alpha} = \cot\Delta_\alpha \delta_{\beta\alpha}.$$

Then using the relation between the reactance matrix and the scattering wavefunction [Lan58], one can show that, if the relative motion wavefunctions for each channel are taken to be eigenstates of the scattering operator with the eigenvalue $\exp(2i\Delta_\gamma)$, the asymptotic scattering wavefunction is given by [Del58]

$$\Psi_\infty^\gamma = Q_\gamma \sum_\alpha \sqrt{\frac{\mu_\alpha}{k_\alpha}}\, T_{\gamma\alpha}\left\{\cot\Delta_\gamma F_{\ell_\alpha}(r_\alpha) + G_{\ell_\alpha}(r_\alpha)\right\}\frac{\varphi_\alpha}{r_\alpha}\mathcal{Y}_\alpha(\theta,\phi), \tag{2.14}$$

where Q_γ is a constant (with respect to r_α) and μ_α is the reduced mass of channel α. By requiring the wavefunction in equation (2.14) to remain finite and non-vanishing over every extended domain $\mathcal{R}$ of the radial

configuration space in the external region, Delves[17] has obtained the following results for the energy dependence of the elements of the $\mathcal{M}$-matrix near the channel threshold: In the limit as $k \to 0$,

$$\cot\Delta_\gamma \to \text{const} \times k_\gamma^{-(2\ell_\gamma+1)},$$

$$T_{\alpha\gamma} \to \text{const} \times k^{|\ell_\alpha - \ell_\gamma|},$$

and

$$Q_\gamma \to \text{const} \times k_\gamma^{(\ell_\gamma+1/2)}$$

for neutral particle scattering. For charged particle scattering,

$$\cot\Delta_\gamma \to \text{const} \times k_\gamma^{-(2\ell_\gamma+1)} \frac{|e^{2\pi\eta} - 1|}{\eta^{2\ell_\gamma+1}},$$

$$T_{\alpha\gamma} \to \text{const.},$$

and

$$Q_\gamma \to \text{const} \times k_\gamma^{(\ell_\gamma+1/2)} \frac{\eta^{(\ell_\gamma+1/2)}}{|e^{2\pi\eta} - 1|^{1/2}}.$$

In each of these relations, η is the Coulomb parameter given in appendix B. There is apparently a difference between the threshold behavior of the off-diagonal elements of $\mathbf{T}$ for neutral and charged particle scattering. In the former case, the off-diagonal elements *must* vanish; in the latter case, they may vanish or they may not, depending on the dynamics.

---

17 Note that there is a typographical error in the second of equations A4b of [Del58], from which these results are taken.

The standard Coulomb-modified effective range expansion, given as in chapter 1, by

$$K_\gamma(k^2) = k^{(2\ell_\gamma+1)}C^2_{\ell_\gamma}(\eta)\left[\cot\Delta_\gamma + \frac{2\eta h(\eta)}{C_0^2(\eta)}\right] = -\frac{1}{a_\gamma} + \frac{r_\gamma k^2}{2} + P_\gamma k^4 + \ldots$$

has the proper threshold behavior. Note that $h(\eta)$ vanishes like k^2 as k goes to zero[18]. A rigorous derivation of the Coulomb-modified effective range expansion and mathematical expressions for the effective range parameters are given in [Bol85].

The requirement of [Hut83b] that the mixing parameters vanish at threshold, equivalent to requiring the off-diagonal elements to vanish there, is not supported by the investigation of [Del58]. Furthermore, the fact that these elements must vanish for neutron-deuteron scattering does not imply that they must vanish for proton-deuteron scattering. The argument that the symmetry of the $\mathcal{S}$-matrix demands this threshold behavior is valid only for those elements of $T_{\beta\alpha}$ that necessarily couple channels having different relative orbital angular momenta. In this regard, the behavior of n–p and p–p scattering is not relevant, because the intrinsic wavefunctions of those systems have well-defined orbital angular momenta that do not couple dynamically to the orbital angular momenta of the relative-motion wavefunction (at least not near the elastic threshold). Even without considering the effects of the electrostatic polarization potential, the threshold behavior of the p–d mixing parameters are not amenable to simple analysis.

2.4.1 The anomalous effective range expansion

A generalized collision matrix, such as the reactance matrix $\mathcal{K}$, can always be written in terms of the logarithmic derivative matrix $\mathcal{R}$. The general relationship is given by [Lan58]:

---

18 This is readily verified by considering the asymptotic behavior of the real part of the digamma function $\psi(1+i\eta)$ as $\eta\to\infty$ [Abr72].

$$\mathcal{U} = (\mathbf{O}\rho^{-1/2} - \mathcal{R}\mathbf{O}^{0\prime}\rho^{1/2})^{-1}(\mathbf{I}\rho^{-1/2} - \mathcal{R}\mathbf{I}^{0\prime}\rho^{1/2}),$$

where $\mathbf{O}$, $\mathbf{O}^{0\prime}$, $\mathbf{I}$ and $\mathbf{I}^{0\prime}$ are diagonal matrices whose elements correspond to "generalized" outgoing and incoming solutions to the Schrödinger equation in the external region, and their derivatives. The matrix ρ is a diagonal matrix whose elements are the product kr_α, where r_α is the channel radius for channel α. For the particular choices; $\mathbf{O} = -\mathbf{G}$, $\mathbf{O}^{0\prime} = \mathbf{O}' = -\mathbf{G}'$, $\mathbf{I} = \mathbf{F}$, and $\mathbf{I}^{0\prime} = \mathbf{I}' = \mathbf{F}'$; one obtains an expression for the reactance matrix. This expression can be simplified by taking the channel radius matrix to be proportional to the identity, so that one has

$$\mathcal{K} = -(\mathbf{G} - \rho\mathcal{R}\mathbf{G}')^{-1}(\mathbf{F} - \rho\mathcal{R}\mathbf{F}') .$$

Unfortunately, although it is known that the transformation $\mathcal{K} = \mathbf{T}\mathcal{K}\mathbf{T}^{-1}$ diagonalizes $\mathcal{K}$ one does not necessarily obtain an enlightening result thereby, since it is not clear that this same transformation also diagonalizes $\mathcal{R}$. However, it is useful to consider the case for which both the $\mathcal{R}$-matrix and $\mathbf{T}$ are diagonal. Then the reactance matrix has the form

$$\mathcal{K}_{\beta\alpha} = -\frac{F_{\ell_\beta} - \rho\mathcal{R}_\beta F'_{\ell_\beta}}{G_{\ell_\beta} - \rho\mathcal{R}_\beta G'_{\ell_\beta}}\,\delta_{\beta\alpha} . \qquad (2.15)$$

The F_ℓ, G_ℓ, F'_ℓ and G'_ℓ in this equation are the regular and irregular solutions to the wave equation characterizing scattering through the external region potential, and their derivatives with respect to $\rho = kr$, evaluated at some channel radius $r = r_c$. The $\mathcal{R}$-matrix in equation (2.15) is the same as that given in [Lan58].

Equation (2.15) can be used to derive the effective range expansion for any system in which the long-range interaction is square-integrable[19].

---

19 See equations 2.6, 2.7 and 2.8 of [Tei51] for conditions on the interactions in the external region.

Using this method, Teichmann derived an interpretation for the "anomalous" effective range expansion in terms of the coefficients of a Taylor series expansion of the single-channel $\mathcal{R}$-matrix [Tei51]. In the general case, and for the particular case of the Coulomb interaction, the expressions involved are very complicated.

Teichmann's argument is more transparent for neutral-particle scattering[20]. For the particularly simple case of S-wave scattering, the regular and irregular solutions are F = sinkr and G = coskr. Therefore,

$$\mathcal{M} = \cot\Delta = -\frac{G'}{F'} - \frac{\frac{1}{F'^2}}{\frac{F}{F'} - \rho\mathcal{R}} = \tan\rho_c - \frac{1 + \tan^2\rho_c}{\tan\rho_c - \rho_c\mathcal{R}}$$

so that

$$k\cot\Delta = k\tan kr_c - \frac{1 + \tan^2 kr_c}{k^{-1}\tan kr_c - r_c\mathcal{R}} \qquad (2.16)$$

The single-channel $\mathcal{R}$-matrix has the form

$$\mathcal{R}_\ell = \sum_\lambda \frac{\gamma_{\ell,\lambda}^2}{E_{\ell,\lambda} - E}$$

where the reduced width amplitudes $\gamma_{\ell,\lambda}$ are a measure of the strength of the λ-resonance. The $\mathcal{R}$-matrix can be expanded in even powers of k about the channel threshold, E = 0, so that

$$\mathcal{R} = \sum_{j=0}^{\infty} R_j k^{2j}$$

---

20 Teichmann's definition of $\mathcal{R}$ is somewhat different than that adopted here [Tei51]. Furthermore, the prime symbol in [Tei51] denotes differentiation with respect to r, whereas in this section, and in [Lan58], it denotes differentiation with respect to $\rho = kr$.

where

$$R_0 = \sum_\lambda \frac{\gamma_\lambda^2}{E_\lambda},$$

and

$$R_j = \left(\frac{\hbar^2}{2\mu}\right)^j \sum_\lambda \frac{\gamma_\lambda^2}{E_\lambda^{j+1}}$$

are the expansion coefficients, with μ being the reduced mass. Expanding equation(2.16) up to the second power in k gives

$$k\cot\delta = k^2 r_c - \frac{1 + k^2 r_c^{\,2}}{r_c\,(1 - R_0)} + \cdots$$

$$= -\frac{1}{r_c(1 - R_0)} - \frac{r_c^2 R_0\, k^2}{r_c(1 - R_0)} + \cdots$$

Defining the scattering length by

$$a_0 = r_c(1 - R_0), \qquad (2.17)$$

and the effective range parameter by

$$r_0 = -\frac{2r_c^2 R_0}{a_0} = -\frac{2r_c R_0}{1 - R_0},$$

the usual form of the effective range expansion is obtained. Note that if $R_0 \ll 1$, then $a_0 \approx r_c$, and $r_0 \approx -2r_c R_0$. This is the "normal" case for potential scattering. If, on the other hand, $R_0 \gg 1$, then $a_0 \approx -r_c R_0$, and $r_0 \approx 2r_c$.

Suppose now that $R_0 \approx 1$. Then the scattering length will vanish near zero and the effective range parameter will become very large. In this case it is necessary to expand the denominator in equation (2.16) to the fourth power in k. One then has

$$k\cot\delta = k^2 r_c - \frac{1 + k^2 r_c^{\,2}}{r_c(1 - R_0 + k^2[r_c^2/3 - R_1])} + \cdots \qquad (2.18)$$

which is the so-called anomalous effective range expansion. The pole wavenumber is given by

$$k_0^2 = \frac{a_0}{r_c(r_c^2/3 - R_1)} \qquad (2.19)$$

according to which it is clear that the pole location and the scattering length are correlated.

2.4.2 The Phillips lines

Equation (2.19) provides some insight into the so-called "Phillips lines", a roughly linear correlation between the theoretical values for the trinucleon bound state and doublet S-wave scattering length, first noted in [Phi77] for the n–d system. These lines consist of a set of ordered pairs (E_B, O), where O is some three-nucleon observable calculated on the basis of a particular realistic N-N potential and E_B is the trinucleon binding energy calculated with that same nuclear interaction. It was subsequently discovered that similar theoretical correlations exist for the p–d doublet S-wave scattering length and ^{3}He binding energy, and for the trinucleon bound state energies and a host of other three-nucleon observables including the rms charge radius and the ratio of asymptotic D-to-S state amplitudes [Gib88].

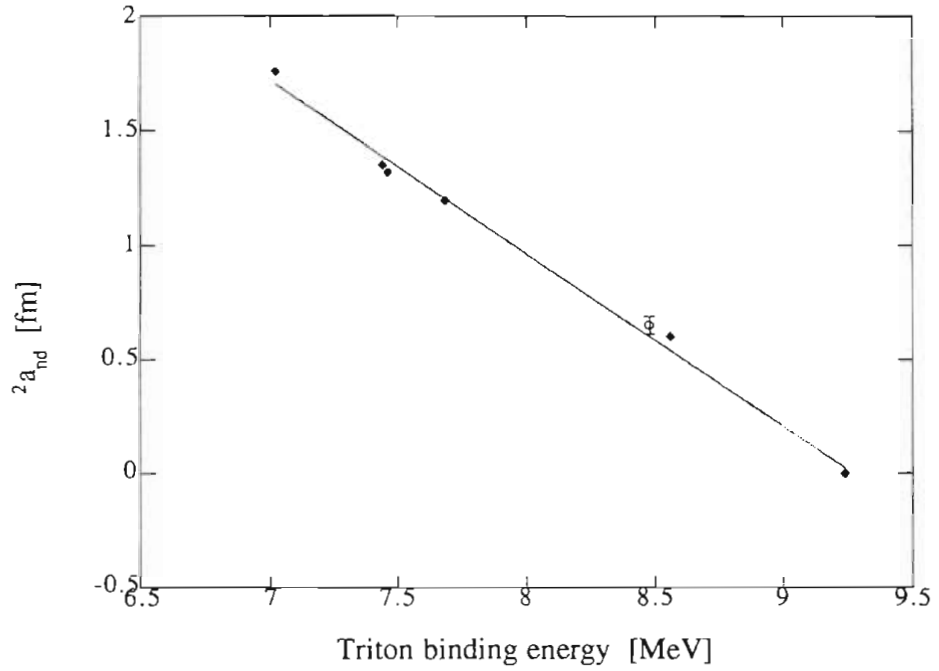

Figure 2.1 Phillips line for the correlation between neutron-deuteron scattering length and triton binding energy

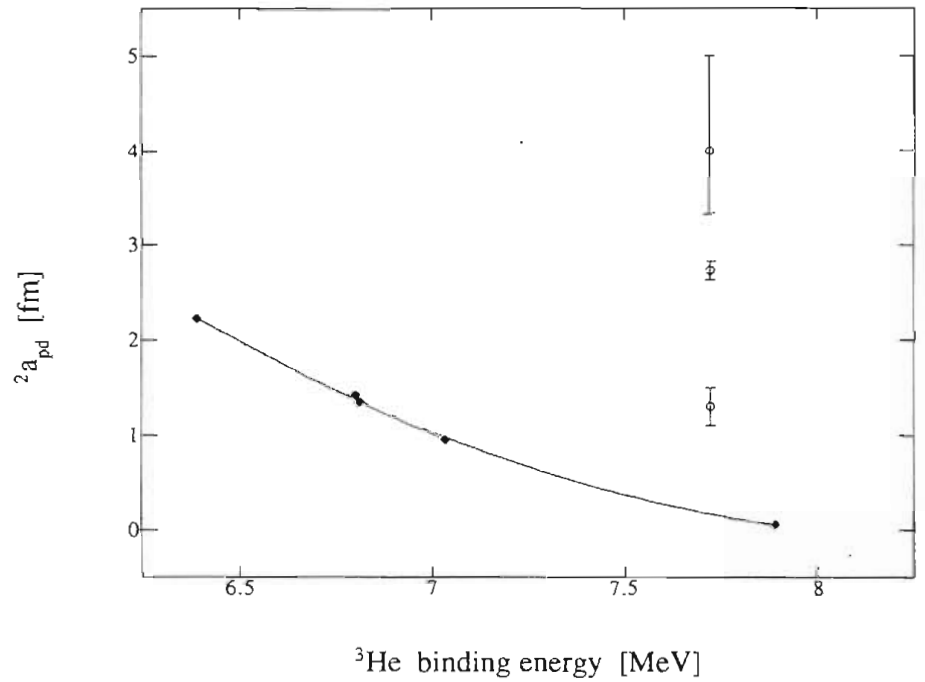

Figure 2.2 Phillips line for the correlation between $^2a_{pd}$ and the ^{3}He binding energy

The pair corresponding to the experimental n–d doublet S-wave scattering length and the triton binding energy lies directly on its scattering length Phillips line, shown in Figure 2.1. None of the pairs representing the correlation between the experimental p-d doublet scattering lengths lie on the calculated p–d doublet S-wave Phillips line, according to which $^2a_0$ ought to be approximately zero [Lev90]. The Phillips line for the p-d scattering length is shown in Figure 2.2.

The trinucleon bound state is dominated by the doublet S-state amplitude, which constitutes nearly 90% of the total bound state amplitude. From a dispersion-theoretical perspective, the low-energy scattering in the doublet S-state is dominated by the bound-state pole and the branch cut corresponding to single nucleon exchange. The nucleon exchange cut can be approximated by a simple pole whose location and strength can be determined either on the basis of theory, or phenomenologically.

Because of the predominance of the doublet S-state in the bound state amplitude, if the N-d interaction does vanish near threshold along the complex k-plane axis, the value of k for which it vanishes should vary approximately linearly with the binding energy. If this value is very close to the elastic threshold, the anomalous effective range expansion will be valid and equation (2.18) then predicts that the scattering length will vary linearly with the vanishing point k_0.

An alternate explanation for the Phillips lines was provided by Efimov [Efi88], who was able to qualitatively reproduce the n-d Phillips lines. One can readily analyze his argument in the context of the model presented in this section. According to equation (2.17), the scattering length is given by $a_0 = r_c(1 - R_0)$. Suppose that for an S-wave channel α, over some energy region, the $\mathcal{R}$-matrix is dominated by a single resonance level. Then

$$\mathcal{R}_\alpha(E) \approx \frac{\gamma_\alpha^2}{(E_\alpha - E)}.$$

Suppose also that the $\mathcal{R}$-matrix parameters are such that $|E_\alpha| \gg |E_B|$, where E_B is the binding energy of the system under consideration. Then it follows that

$$\mathcal{R}_\alpha(E_B) \approx \mathcal{R}_\alpha(0) \approx R_0$$

At a bound state, the $\mathcal{R}$-matrix goes as the reciprocal square root of the bound state energy, so that one anticipates that, up to a constant,

$$a_0 \propto \frac{1}{\sqrt{E_B}}.$$

This is precisely the case for triplet scattering in the n-p system, where E_B is the deuteron binding energy. The relationship $|E_\alpha| \gg |E_B|$ is a consequence of the fact that the deuteron binding energy can be considered small on the scale of the nucleon-nucleon potential or, equivalently, that the deuteron is a loosely bound system. Under these assumptions, the logarithmic derivative for the bound state wavefunction is nearly the same as that for the zero-energy scattering system. Therefore, the $\mathcal{R}$-function evaluated at the bound-state is also equal to the $\mathcal{R}$-function at zero energy. In the case of the three-nucleon system, the argument is essentially the same, although somewhat more complicated. The essential ingredient is to assume that the $\mathcal{R}$-matrix is roughly constant, or only very slowly varying, over the range of energies from the trinucleon binding energy to threshold.

2.5.1 The scattering length in the presence of the long-range electrostatic polarization interaction

The proper definition of the p-d scattering length requires consideration of the influence of the long-range electrostatic polarization potential. It was proved in [Ben85] that the conventionally defined

Coulomb-modified scattering length diverged in the presence of the polarization interaction. Therefore, it was not considered sufficient to regard this interaction as a perturbation to the short-range interaction.

Bencze, et. al. subsequently demonstrated that the scattering length could be appropriately defined by considering the polarization interaction as an additional long-range force, in a manner analogous to the treatment of the nuclear scattering in the presence of Coulomb forces [Ben87]. The so-called long-range modified scattering length, defined so that the zero-energy phase shift is determined with respect to the combined Coulomb plus polarization phase shifts, was shown to be finite and therefore well-defined.

Nonetheless, owing to the complex nature of the solutions to the Coulomb plus polarization potential Schrödinger equation, the use of the rigorously defined scattering length involves serious computational difficulties that would be especially difficult to incorporate into phenomenological calculations in which the effective range parameters must be inferred from the data. Therefore, it is quite fortunate that the authors of [Ben87] were able to show that, as a consequence of the small electric polarizability of the deuteron, above roughly 10 keV scattering energy, the effective range function for the rigorously defined doublet S-wave phase shift is essentially identical to that for the phase shift calculated by incorporating the polarization potential into the short-range interaction. As a practical matter, then, it is sufficient to perform the phenomenological calculations by assuming the form of the standard Coulomb-modified effective range expansion.

Chapter III: Experimental Procedure

"Workin' in the fields till you get your back burned,
Workin' 'neath the wheel till you get your facts learned..."

Bruce Springsteen

3.1.1 Estimates of the systematic uncertainties

In order to estimate the magnitude of the systematic errors likely to be encountered in this experiment, a computer code capable of calculating differential cross sections at arbitrary energies below the deuteron breakup threshold was developed. The input for these calculations were the effective range parameters reported in the literature.

Expected p–d cross sections at 320 keV were first calculated using the phenomenological effective range parameters and energy dependent mixing parameter functions published in [Hut83b]. A second calculation at this same energy was made in which the S-wave spin-doublet and spin-quartet effective range parameters taken from the theoretical calculations of [Che89], were exchanged for those of [Hut83b]. The values of the other parameters were the same as those of [Hut83b].

Figure 3.1 shows the fractional difference between the cross sections calculated with the effective range parameters of [Che89] and [Hut83b]. The fractional difference in Figure 3.1 is defined as

$$\frac{(\sigma_{[Che89]} - \sigma_{[Hut83b]})}{\sigma_{[Hut83b]}}.$$

It is reasonable to conclude on the basis of this plot that a measurement of the differential cross section at 320 keV incident proton energy is fairly

sensitive to the difference between the calculated and experimentally extracted values of the doublet S-wave phase shift parameters.

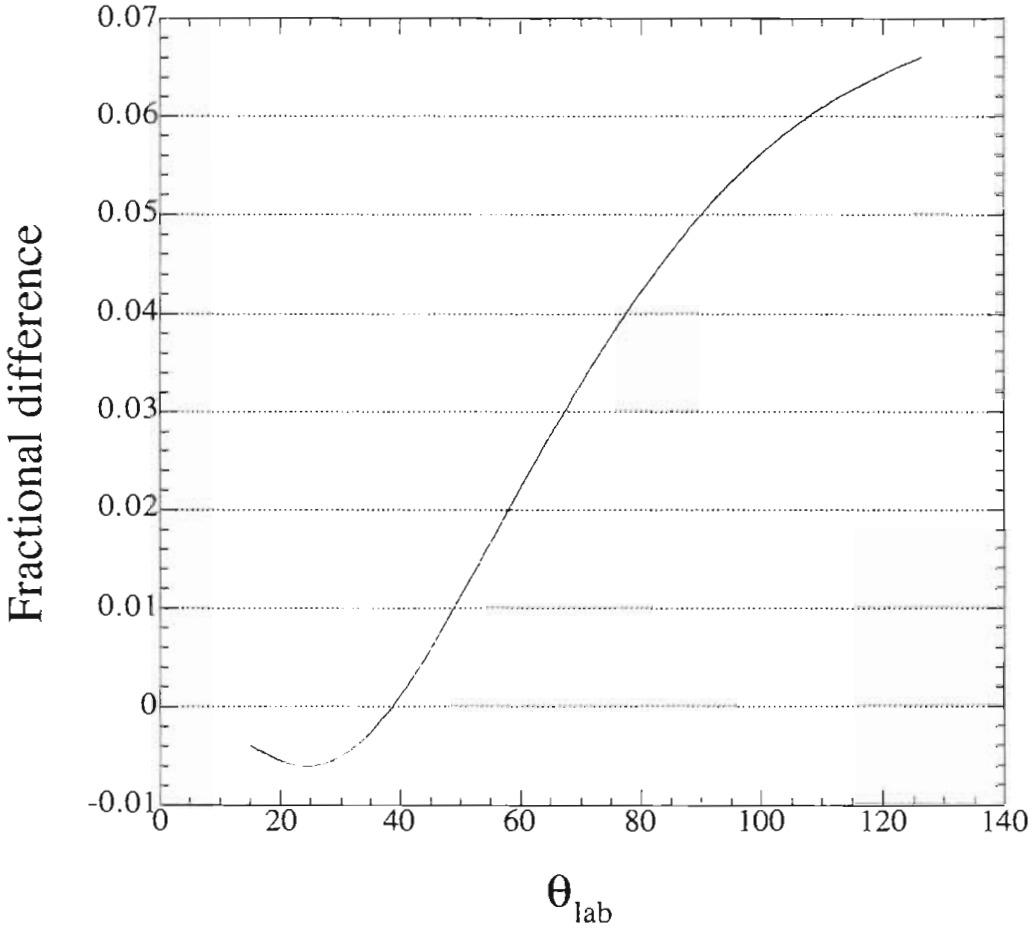

Figure 3.1 Fractional difference of p–d differential cross section calculated with S-wave effective range parameters of [Che89] and [Hut83b]

The typical magnitudes of the cross section for this reaction are of the order of several tens to several hundreds of mb/sr. Therefore, it was anticipated that systematic uncertainties would be more significant than statistical errors. The differential expression for the cross section, corresponding to the zeroth order approximation, relates the observed yield $Y(\theta)$ to the differential cross section $\sigma(\theta,E)$. According to this expression,

$$dY(\theta,E) = I(t)\, n(t)\, \sigma(\theta,E)\, d\Omega\, dE\, dt\,, \qquad (3.1)$$

where n(t) is the target thickness in number-areal density, I(t) is the incident beam intensity and $d\Omega = \sin\theta d\theta d\phi$ is the differential solid angle. The target thickness and beam intensity are typically time-dependent quantities.

The experimentally determined yield at a nominal energy and angle is

$$Y(\theta_0,E_0) = \int_\theta \int_E \int_t I(t)\, n(t)\, \sigma(\theta,E)\, d\Omega\, dE\, dt \qquad (3.2)$$

To obtain a differential expression comparable to equation (3.1) from an experimental determination of the angular distribution of reaction yield, it must be shown that the yield averaged over the finite incident energy spread and detector angular acceptance of the experimental configuration is equivalent to the differential expression in equation (3.1), evaluated at the nominal experimental values of θ_0 and E_0. In addition, the time-variation of the product I(t)n(t) must be taken into account.

A sufficient condition for eliminating the correlation between energy and angle in equation (3.2) is that

$$\int_\theta \frac{\partial\sigma}{\partial\theta}\, d\theta \approx 0$$

If the detector is far from the target, then $\sin\theta d\phi$ is essentially constant. By requiring the partial derivative of the cross section to be linear across the polar angular acceptance, this integral will vanish by the anti-symmetry of the integrand about its value at the nominal angle.

Figure 3.2 shows an estimate of the specific sensitivity of the cross section with respect to variations of the scattering angle. The calculations at 100.5° correspond to the recoil particle observed at a scattering angle of 25°. That is why the variation has a different sign and is large relative

to the 50° variation. This reflects the fact that the angular spread in the recoil reaction corresponds to a relatively larger angular spread in the equivalent direct reaction.

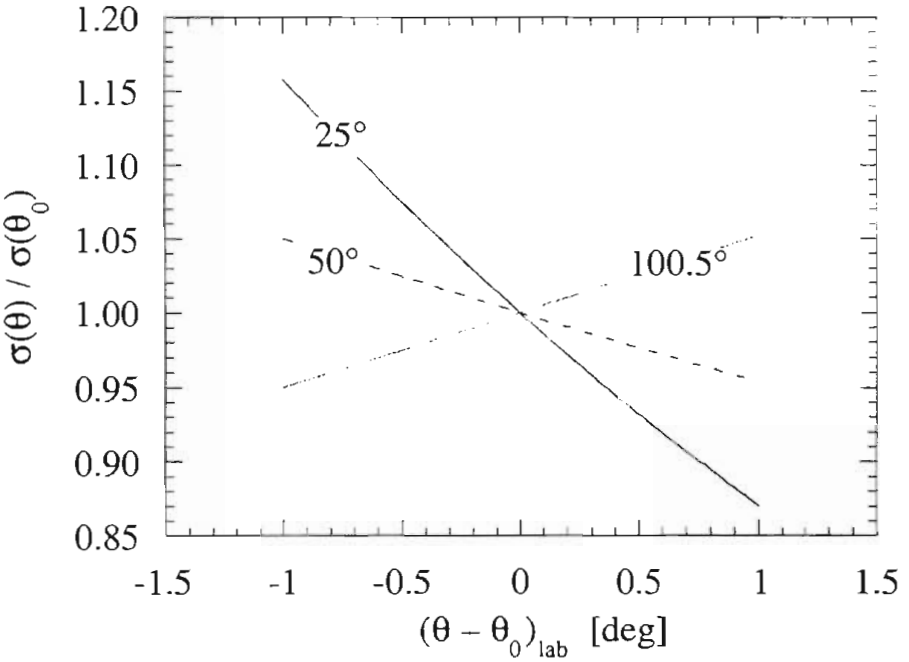

Figure 3.2 Specific angular sensitivity of p–d cross section at E_p = 320 keV, calculated with the effective range parameters of [Hut83b]

Our spectrum detectors were typically mounted 24 cm (collimation radius) from the target. They were equipped with 250 μm thick collimators. The horizontal opening of the collimators was 1.6 mm, while the vertical opening was 4.0 mm. Thus, the polar angle acceptance was $\delta\theta = \pm 0.19°$ and the detector solid angle was $\delta\Omega = 1.1 \times 10^{-4}$. Over the angular range given by $\delta\theta$, the cross sections can be considered linear.

Because the cross section is so sensitive to the scattering angle, it is obviously very important to determine the detector angle setting accurately. The angle-setting apparatus was equipped with a Vernier scale, permitting, in principle, a resolution of ±0.05°. At each angle at

least three, and often four or five, runs were taken and the angle was re-set for every run. In this manner, the systematic error arising from an incorrect angle setting was partially randomized.

The total angular offset of the detector relative to the nominal set-point was determined by measuring the $^{12}C(p,p)^{12}C$ cross section at a number of angles symmetrically about $\theta_{nom} = 0°$ and adjusting the nominal angle until the angular distribution also appeared symmetric. A Monte-Carlo code, described in the following chapter, was used to perform the offset calculation.

Uncertainties in the reaction energy arise from two sources: energy straggling in the target and uncertainties in determining the true nominal energy. The specific energy sensitivity of the differential cross-section at three different angles is shown in Figure 3.3.

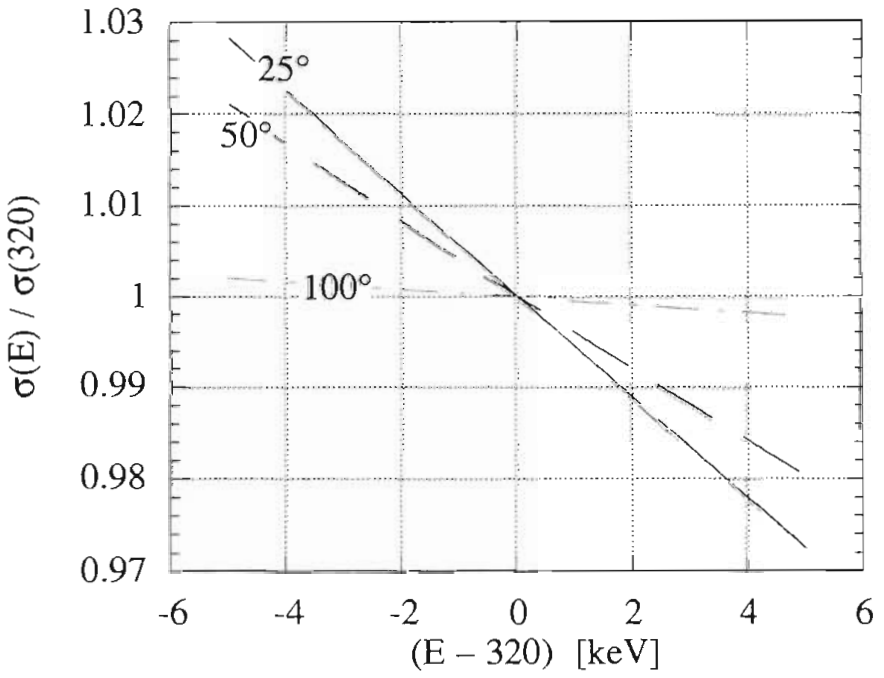

Figure 3.3 Specific sensitivity of p–d cross section at $\theta_{lab} = 25°$, 50° and 100°, with respect to variations of the incident proton energy about a nominal value of 320 keV.

The variation of the cross section with respect to energy is fairly linear over the range of ±5 keV, which is a conservative estimate of the spread in reaction energies. Therefore, one can reasonably take the cross section at the nominal value of the energy to represent the energy-integrated value of the cross section. Because the energy loss in the targets was relatively large (several keV) and the targets were made from an exotic material whose stopping power is not yet determined, it was not possible to determine the mean reaction energy solely on the basis of a knowledge of the incident beam energy. The mean reaction energy was instead determined by fitting the angular distribution of the difference in the kinematic shifts experienced by protons scattering from deuterium and carbon in the target. This procedure is described more fully in chapter 4.

Because it was important to keep the range over which the energy was integrated as small as possible, this experiment was performed using solid deuterated targets. Unfortunately, deuterium tends to evaporate from such targets under ion beam bombardment. Furthermore, carbon was observed to build up on the targets. Therefore, neither the carbon nor the deuterium thickness of the targets was constant in time.

The product I(t)n(t) is common to all angles, however, and if there are no other factors under the time integral, it is possible to integrate this product and then divide the cross section at the detection angle by the cross section at some fixed monitoring angle. Assuming that the energies and angles are all independent of the time, then the time-integral cancels in the ratio and one is left with an expression for the relative cross section at an angle θ:

$$\sigma(\theta_{det},E) \propto \frac{Y(\theta_{det},E)}{Y(\theta_{mon},E)}$$

where the normalization constant is given by the ratio of the solid angles subtended by the detector and the monitor, multiplied by the cross-section at the monitoring angle.

Unless the cross section at the monitoring angle is well-known, this method provides a relative rather than an absolute determination of the cross section. It is always possible to go back at any point and measure the absolute cross section very carefully at one angle and then fix the normalization by this measurement. Also, the theoretical and experimentally derived calculations agree at a couple of angles within the range of angles that were measured. It therefore seems reasonable to normalize the data at one or two of these points.

It is also possible to allow the normalization to be a free parameter in the phase shift analysis. This was done for some of the data in the analysis of [Hut83b]. This procedure is justifiable if the differences between various parameterizations are not merely one of overall scale. Under this assumption, not much additional uncertainty is introduced by allowing the normalization to "float", especially if the range of values is tightly restricted, which is the case if a first-order approximation is made by fixing the normalization value at one of the angles where distinct parametric sets can be expected to overlap.

3.2.1 The Minitandem accelerator

The Minitandem accelerator was built in order to accelerate light ion beams from 80 keV, which is the current maximum beam energy attainable from the TUNL Atomic Beam Polarized Ion Source [Cle95], to the several hundred keV energies required for this experiment and for other experiments in the TUNL research program [Bla93]. The idea for the Minitandem accelerator was first ventured by G. Clausnitzer, nearly a decade ago[21].

A tandem accelerator accelerates a charged particle beam in two stages. Negatively charged ions, produced in an ion source, are attracted to the positive terminal of the device—the additional energy they acquire in this first stage is just the product of their charge multiplicity and the potential at which the terminal is held. A thin stripper foil, usually made

---

[21] This suggestion was made by Dr. Clausnitzer in a private communication with Prof. E.J. Ludwig of the University of North Carolina at Chapel Hill.

of carbon, is mounted within the terminal in the path of the beam. The purpose of the stripper foil is to remove electrons from the negatively charged ions. Depending on the charge-exchange cross section of the ionic type in the stripper material at the velocity of the beam, various fractions of the beam will experience some degree of electron stripping. Those components having a net positive charge will be accelerated down to ground potential again, having acquired an additional energy given by the final charge multiplicity times the terminal potential. The total energy acquired by a given particle in the beam is

$$\Delta E = V_{term}(Z_{fin} - Z_{in})$$

where Z is the charge multiplicity of the particle.

The Minitandem accelerator resembles a large aluminum egg. It consists of a 51 cm diameter cylindrical vacuum chamber, 20 cm high, surmounted top and bottom by polished aluminum hemispheres intended to lower the electric field gradients. A carousel is mounted in the center of the chamber in which 13 pairs of apertures were drilled. Twelve of these aperture pairs are for mounting stripper foils and the 13^{th} permits the beam to pass unimpeded when no acceleration is desired. A handle extends from the top of the carousel through the roof of the accelerator, so that stripper foils can be changed without breaking vacuum merely by rotating the carousel handle. A Plexiglas port is located on the roof of the Minitandem, along the beam axis just forward of the carousel and in line with an internally mounted periscope-style mirror, so that one may view the stripper foil . The accelerator is depicted in Figure 3.4.

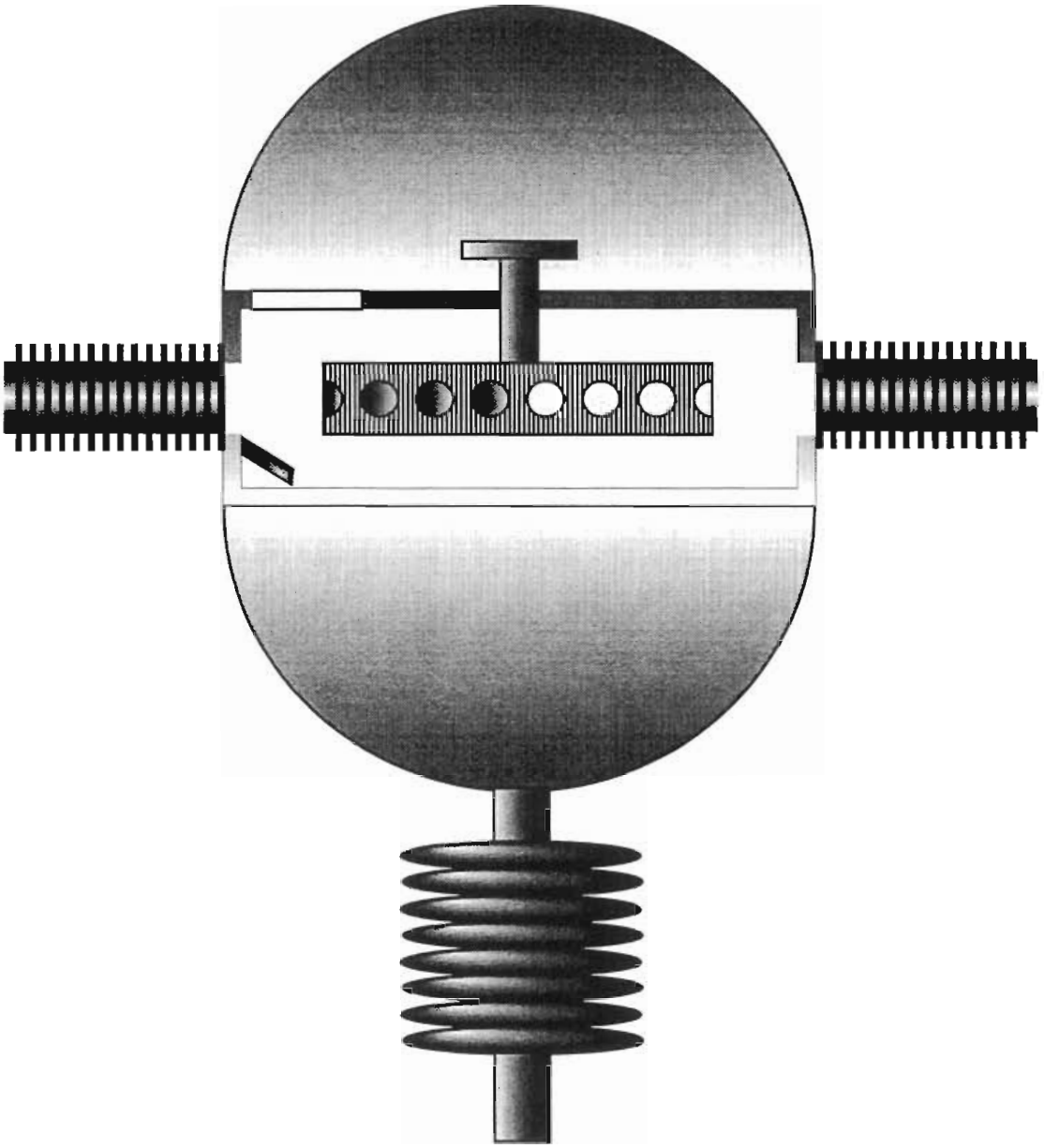

Figure 3.4 The Minitandem accelerator

The acceleration tubes incidentally provide radial focusing to the incident beam; the "strength" of this focusing depends on the ratio of the energy gain to the initial energy. As the beam follows the field lines imposed by the electrodes, it experiences an inward radial force during the first (geometric) half of its trajectory and an outward radial force during the second half. Since the beam is being accelerated, in every inter-electrode interval its velocity in the second half of the trajectory is

greater than its velocity in the first half, and hence it takes a longer time to complete the first half of its path than the second half. Hence it spends more time in the inwardly focusing field than in the outwardly focusing field, in every interval.

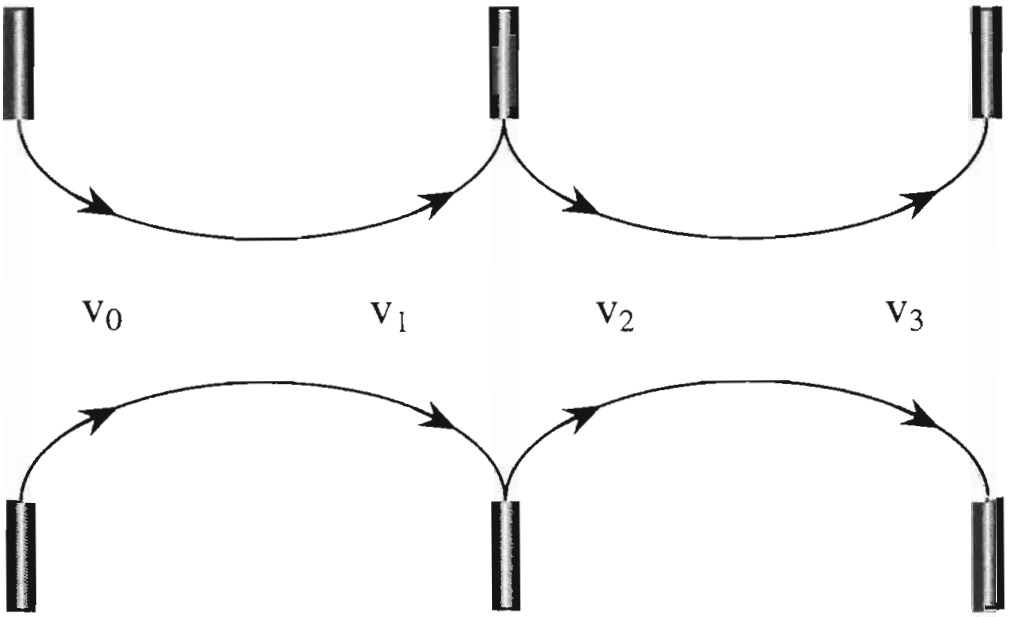

$$v_3 > v_2 > v_1 > v_0 \Rightarrow t_3 < t_2 < t_1 < t_0$$

The focusing effect can be amplified by choosing the electrode apertures such that their diameter diminishes monotonically in the direction of acceleration. This deforms the field so that the magnitude of the radial component of the field is greater in the focusing phase of the trajectory than in the de-focusing phase.

The entrance aperture to the accelerator was made as large as possible, so as to permit entry to as much beam as could be focused onto the stripper foil without hitting the electrodes. The maximum permissible aperture depends upon the optical profile of the incident beam, the operating potential of the accelerator, and the fixed "focusing gradient" of the tube—essentially the diameters of the electrode apertures in the entrance tube. Because we did not know the optical profile of the beam,

nor were we able to freely select the diameters of electrodes used in the construction of the acceleration tubes, the current system cannot be considered optimal.

Multiple scattering calculations performed using the formulation of Marion [Mar67] showed that, for 2 $\mu g/cm^2$ carbon stripper foils, 90% of the beam lies within a cone of 2° half-angle. This is less than the angular acceptance of the entrance port to the downstream acceleration tube, and one expects that most of the beam clearing this port should be transmitted to the exit, owing to the radial focusing provided by the downstream tube, especially at the highest energies. However, we have noticed substantial carbon deposits surrounding the downstream port. These cannot be from the primary beam, since this is blocked by the stripper holder. It may be that these are carbon atoms ejected in the forward direction by nearly head-on collisions with incident protons.

A great deal of data concerning the dependence of the analyzed beam current upon various operating parameters were collected soon after the Minitandem was installed. Of these data, perhaps the most useful as a figure of merit are the data on the transmission fraction: the fraction of beam incident at the Minitandem entrance that was measured on a Faraday cup downstream of the analyzing magnet. This magnet selected only that component of the beam whose energy was consistent with a single positive charge as it left the Minitandem stripper foil. The experimental set-up for these measurements is indicated schematically in Figure 3.5.

The fractional transmission is defined here as the ratio of beam current observed on the LEBAF2 beamstop to that observed on the LEBAF1 beamstop. The data were taken using polarized negative ions from the TUNL Atomic Beam Polarized Ion Source. Selected results of these measurements are shown in Figure 3.6, along with curves indicating the positive charge fractions predicted on the basis of the data taken in [Kre81], using the fitting parameters of Table D.1.

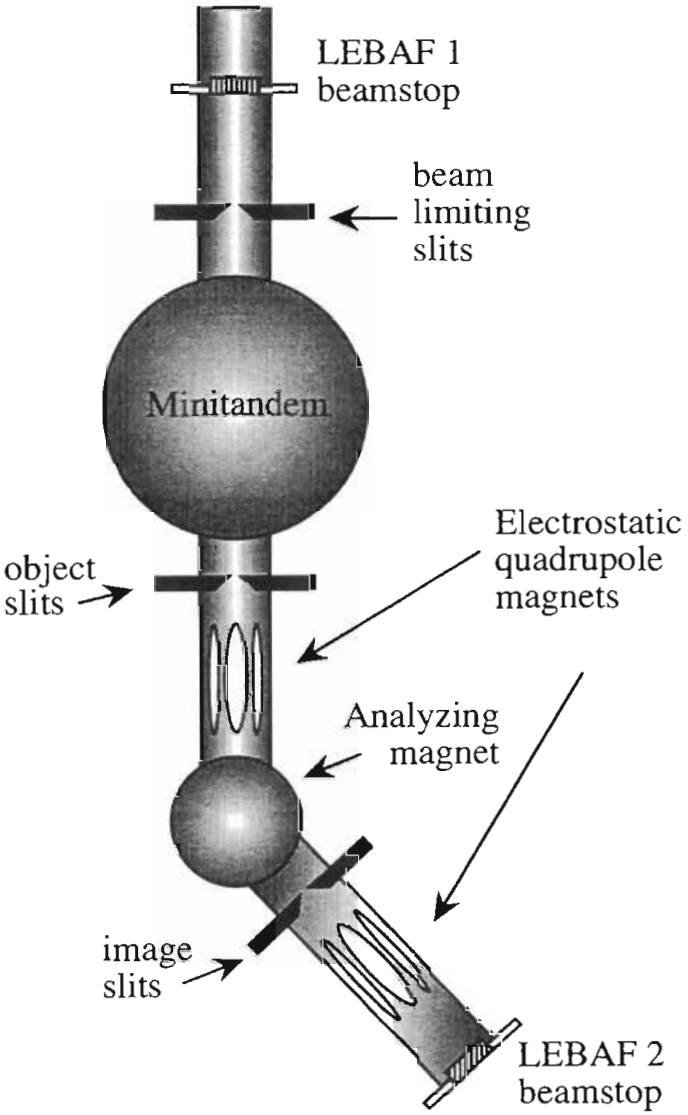

Figure 3.5 Experimental set-up for Minitandem transmission tests

It is apparent from this plot, that in this case, at least, the thickness of the stripper foil was irrelevant to the observed fractional transmission. Furthermore, the fact that the transmission is roughly the same for protons and deuterons implies that charge exchange was not, in this case, the limiting factor. It is likely that the discrepancy between the theoretical and experimental yields arise from the relatively poor focusing provided by the upstream acceleration tube at low incident ion energies. Because the cross section for the p–d elastic reaction is so large

at low energy, however, we were never limited by having insufficient beam unless some piece of equipment was obviously malfunctioning.

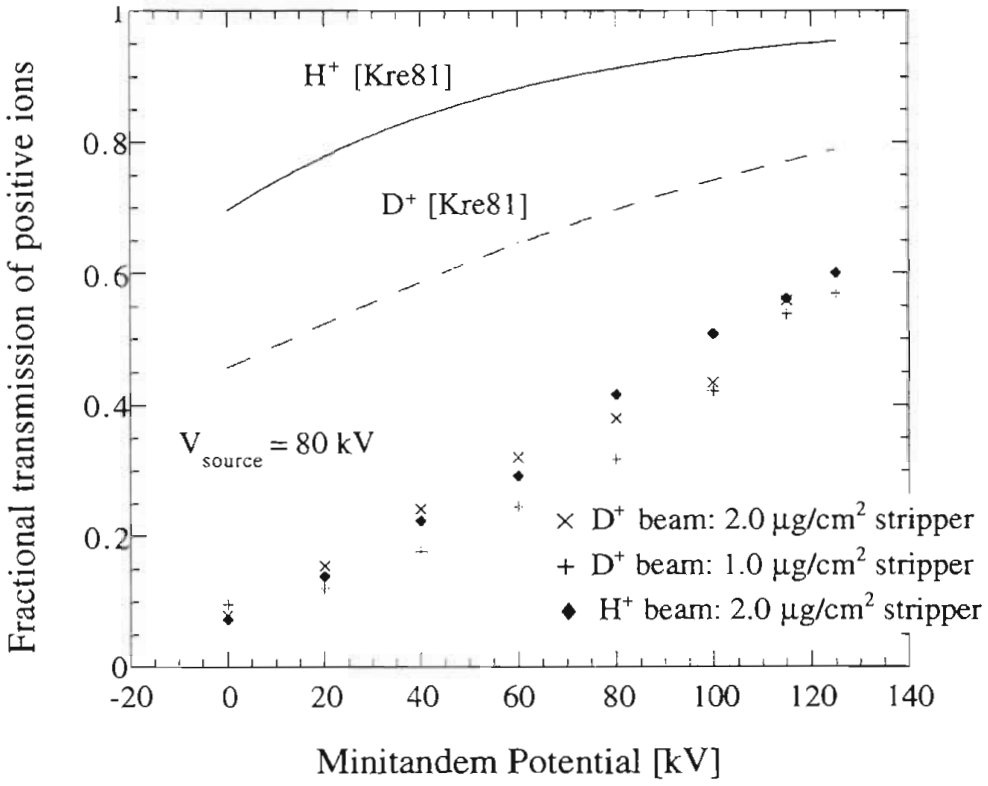

Figure 3.6 Data from Minitandem transmission tests

3.2.2 Energy calibration of the Minitandem accelerator

Most of the data in this subsection are culled from an internal report prepared by Dr. C. R. Brune of the UNC Nuclear group [Bru95], who was largely responsible for supervising and performing the calibration. Because the power supply that was used to raise the Minitandem to high voltage during the experimental runs had a (theoretically) maximum output potential of 125 kV, protons could not be accelerated to an energy greater than 330 keV. The $^{19}F(p,\alpha\gamma)^{16}O$ reaction is an excellent reaction to use in calibrating the accelerator, since it is a very strong, yet relatively narrow ($\Gamma = 2.34 \pm 0.04$ keV [Uhr85]) resonance. However, since the resonance energy is $E_p = 340.46$ keV

[Ajz83], it was not possible to traverse the peak of this resonance using the 125 kV power supply[22].

Therefore, a 200 kV power supply[23] was used to accelerate a proton beam to sufficient energy to excite the 340 keV ^{19}F resonance. In order to determine the gain of PS#2, the peaks of the $^{19}F(p,\alpha\gamma)^{16}O$ resonance at $E_p = 223.00$ keV and the $^{27}Al(p,\gamma)^{28}Si$ resonance at $E_p = 326.97$ keV were also correlated with the gain of PS#2. Power supply #1 and power supply #2 were then cross-calibrated by matching the centroids observed in $^{12}C(p,p)^{12}C$ scattering at energies within the range of power supply #1. The gains of both power supplies were measured in arbitrary units given by the Digital Voltage Meter (DVM) reading across a current shunt running from high voltage to ground. The scale of the shunt was such that it nominally provided a voltage reading given by $DVM = \frac{V}{12.5}$, with V being the potential across the shunt.

The targets for the resonance reactions were prepared by standard vacuum evaporation techniques. The ^{19}F target consisted of a 50 $\mu g/cm^2$ deposit of CaF_2, whereas the ^{27}Al target, also 50 $\mu g/cm^2$, was prepared from natural aluminum. Given the narrow width of these resonances and the large energy losses experienced by protons in CaF_2 and aluminum at low energies, these targets can be considered infinitely thick. The resonance peaks were traversed a number of times in each case, with reasonable reproducibility in all but one instance.

The fluorine resonances were fit with a single-level form, the yield being given by

$$Y \propto \left\{ \frac{\pi}{2} + \tan^{-1}\left[\frac{2(E - E_R)}{\Gamma} \right] \right\}$$

---

22 In what follows, the 125 kV power supply is denoted power supply #1 or simply PS1.

23 Hereafter denoted power supply #2 or PS2.

where Γ is the experimental resonance width. The $^{27}Al(p,\gamma)^{28}Si$ excitation curve was fit to an error function. The resonance parameters and DVM readings from PS2 are summarized in Table 3.1. The resonance peaks and widths are taken from [Uhr85] and references cited therein.

Table 3.1: Resonance parameters and correlation to PS2 DVM

Reaction	E_{Res} (keV)	Γ (eV)	Power supply 2 DVM
$^{19}F(p,\alpha\gamma)^{16}O$	340.46 ± 0.04	2340 ± 40	6.590
$^{19}F(p,\alpha\gamma)^{16}O$	223.99 ± 0.07	985 ± 20	3.653
$^{27}Al(p,\gamma)^{28}Si$	326.97 ± 0.05	< 38	6.254

From these values, an absolute calibration of the Minitandem accelerator/power supply #2 composite system was made by performing a linear fit of the sum of the resonance energies and the energy lost in the 3 $\mu g/cm^2$ carbon stripping foil[24], vs. the DVM, shown in Figure 3.7.

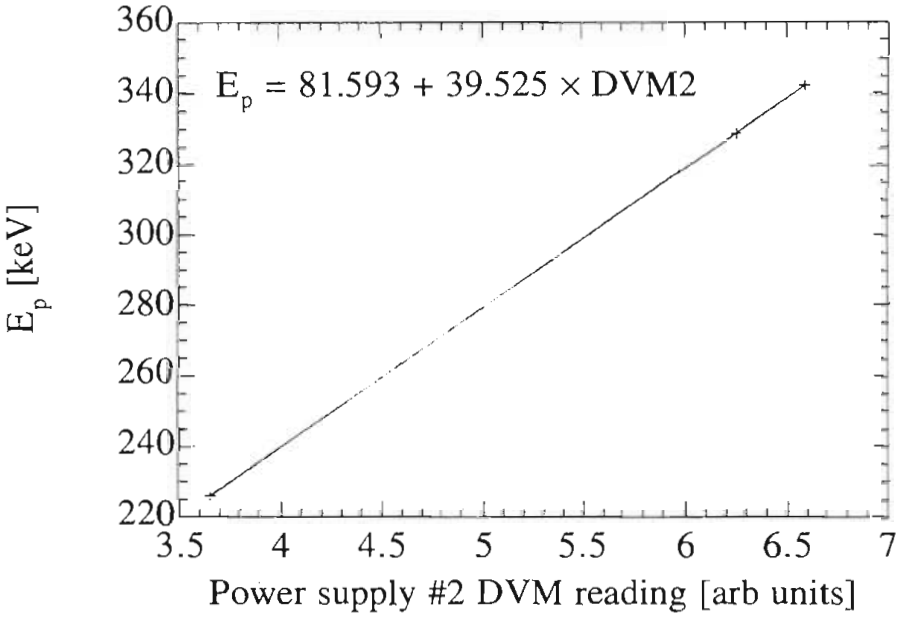

Figure 3.7 Absolute energy calibration of power supply #2

[24] Dr. Brune calculated this energy loss to be 1.7 keV for each of the flourine resonances and 2.0 keV for the aluminum resonance.

The offset fit of 81.593 keV is reasonable. Since the source was set to operate at 80 kV and the potential on the source's cesium oven was 0.9 kV, the predicted offset potential is 81.8 keV. The 210 eV discrepancy is both inconsequential and within the error arising from uncertainty as to the thickness of the stripping foil. The observed gain of 39.525 keV/DVM is in fair agreement with the gain of 40.0 specified by the manufacturer.

For each power supply, a relative energy calibration was established by scattering the accelerated protons through a carbon foil at energies given by various gain settings, and observing the peak locations at fixed detector angles of ±30°. Equating the linear fits of $^{12}C(p,p)^{12}C$ centroid vs. DVM setting of the two supplies established the cross-calibration. The linear fits for power supplies #1 and #2 are shown in Figures 3.8 and 3.9 respectively. The data are shown in Table 3.2.

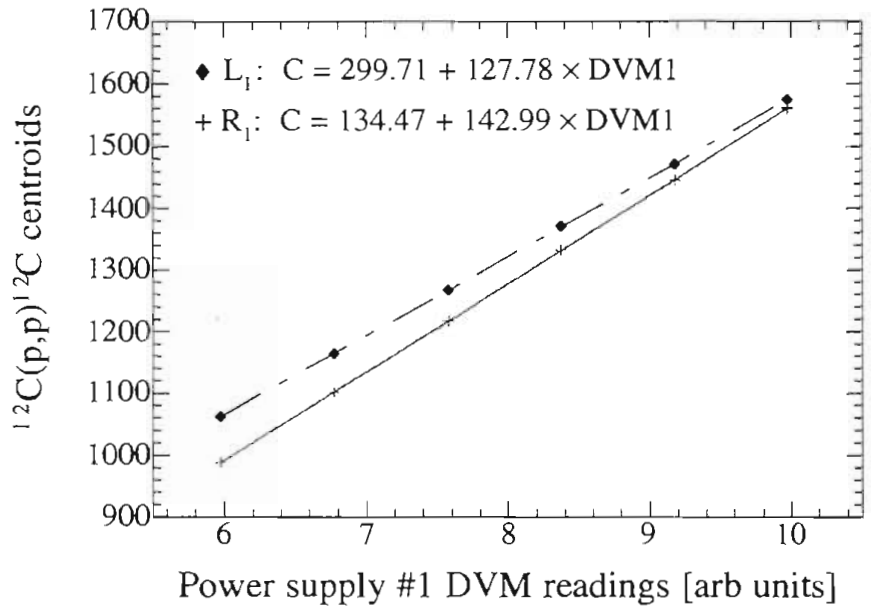

Figure 3.8 Power supply #1 cross-calibration curves

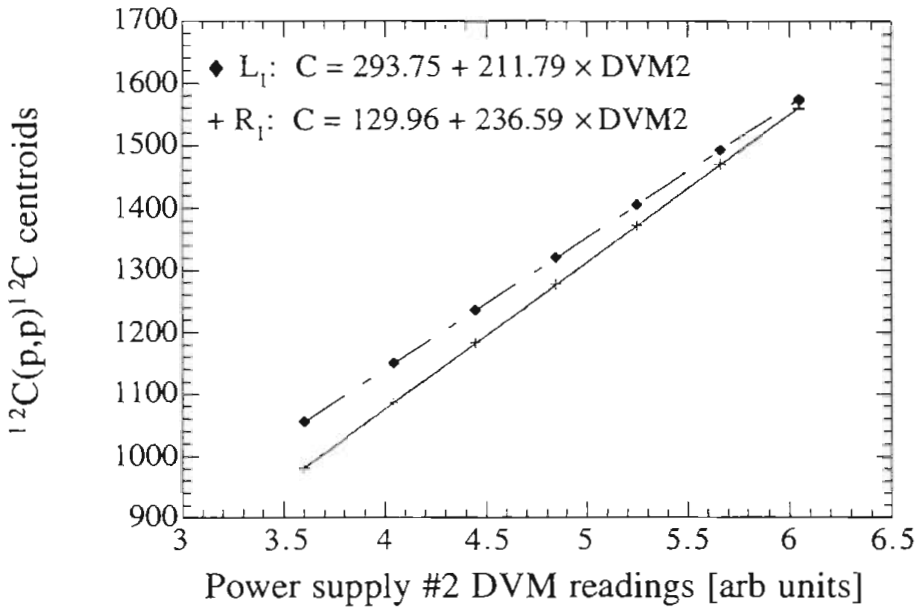

Figure 3.9 Power supply #2 cross-calibration curves

Table 3.2: Cross-calibration data for power supplies #1 and #2.

DVM1	R_1 centroid	L_1 centroid	DVM2	R_2 centroid	L_2 centroid
9.972	1560.78	1573.73	6.046	1560.32	1574.09
9.172	1446.70	1472.45	5.659	1469.61	1492.78
8.372	1333.01	1370.92	5.245	1371.50	1405.38
7.573	1217.97	1267.36	4.845	1277.43	1320.69
6.772	1102.09	1164.45	4.444	1182.21	1235.44
5.972	988.09	1062.84	4.045	1086.92	1150.33
9.972	1559.23	1573.67	3.600	980.33	1055.30

Equating the centroid variables of the PS1 and PS2 plots for both the left and right detectors, one finds that

$$DVM2 = 0.02814 + 0.60333 \times DVM1 \qquad \text{Left detectors}$$
$$DVM2 = 0.01906 + 0.60438 \times DVM1 \qquad \text{Right detectors}$$

Then using the absolute calibration for power supply #2, one obtains:

$$E_p = 82.71 + 23.85 \times DVM1 \qquad \text{Left detectors}$$
$$E_p = 82.35 + 23.89 \times DVM1 \qquad \text{Right detectors}$$

Taking the average value of these two fits yields the absolute calibration for the Minitandem accelerator–power supply #1 composite system. This is

$$E_p = 82.53 + 23.87 \times DVM1.$$

According to the manufacturer of power supply #1, with an ideal shunt the gain ought to be 25.0. The gain is therefore 4.5% lower than expected. At the maximum potential of 125 kV, a 4.5% discrepancy constitutes an 11 keV systematic error in the nominal energy.

3.3.1 Targets

The electronic energy loss of a projectile in an elemental material is peaked at projectile energies where the velocity of the projectile is roughly equal to the orbital velocity of the valence electrons in the target material. Figure 3.10 shows the stopping powers for hydrogen ions in elemental carbon [And77]. The main features of this curve are typical of elemental energy loss curves.

The stopping power is fairly large at the incident proton energies at which this experiment was conducted. Furthermore, at most scattering angles the specific energy loss of the scattered particle exiting the target is greater than the loss prior to scattering, since the kinematic shift forces the exiting particle's energy closer to the peak in the energy loss curve. Therefore, the peak shape arising from energy loss processes is not symmetric about the nominal reaction energy. Only at very small scattering angles, where the kinematic shift is small, is the observed distribution symmetric about the reaction energy. Determining the nominal reaction energy unambiguously therefore becomes increasingly difficult as the energy loss gets larger.

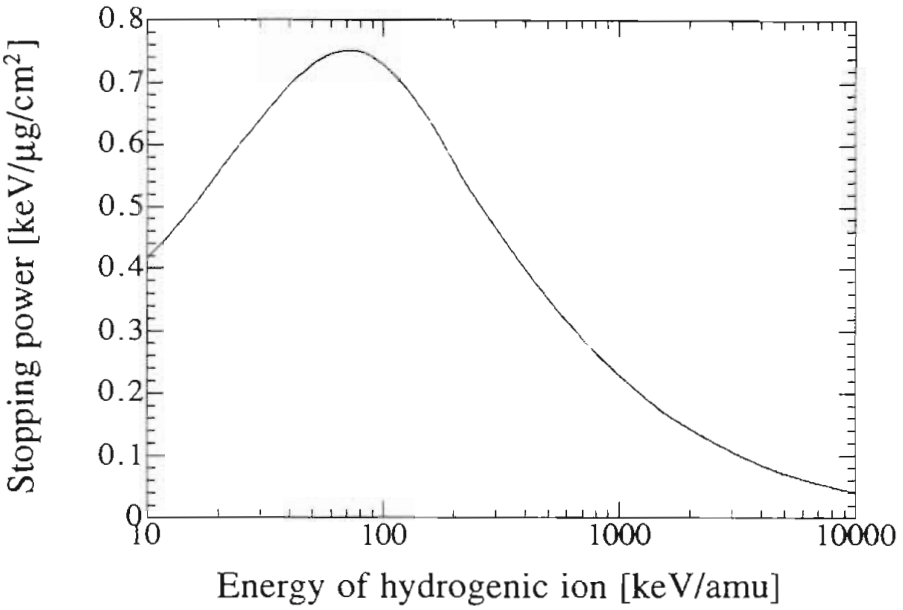

Figure 3.10 Stopping power of hydrogenic ions in carbon

The target material is typically not distributed uniformly within the contaminant matrix. For solid deuterated and hydrogenated targets, it is impossible to monitor the actual distribution of target nuclei under experimental conditions, since this distribution changes under ion beam bombardment. The best defense against systematic uncertainties in the nominal reaction energy is to ensure that the energy loss in the target material is very small.

In addition, isolating the reaction products of interest from the yield of contaminant reactions requires that the energy straggling also be very small. The absolute straggling width typically increases monotonically with the target energy loss. Under the conditions in which this experiment was performed, the electronic width of the yield peaks was quite small, typically around 2 keV (5 to 5.5 keV FWHM). The limiting factor in isolating the peaks of interest, especially at far-forward angles, was the energy resolution of the targets.

A number of attempts were made to fabricate thin, self-supporting polymer targets by a variety of means. These included thermal vacuum evaporation, as well as water casting and spin casting of both

polyethylene and polystyrene from a boiling solution of carbon tetrachloride. The attempts at spin-casting and water casting, in addition to being difficult and dangerous, were uniformly unsuccessful.

Thin polymer films vacuum evaporated onto carbon backings have been successfully made for decades [Mak69]. Films of this nature were used at this lab to serve as targets for the $^2H(\vec{d},p)^3H/^2H(\vec{d},n)^3He$ experiment [Fle93]. Two types of polymers were evaporated onto thin carbon backings, deuterated polyethylene and deuterated parapolyphenol (DPP). The spectrum of E_{nom} = 330 keV protons scattered from 1 $\mu g/cm^2$ of DPP evaporated onto a carbon backing is shown in Figure 3.11. Figures 3.12, 3.13 and 3.14 show the spectra of protons scattered at 300 keV from a composite deuterated polyethylene target consisting of 4 $\mu g/cm^2$ C_2D_4 evaporated onto a 3 $\mu g/cm^2$ carbon backing at three different scattering angles. Finally, Figure 3.15 depicts the spectrum of E_{nom} = 330 keV protons scattered from a target consisting of 4 $\mu g/cm^2$ of C_2D_4 evaporated onto a 4.7 $\mu g/cm^2$ carbon backing at a nominal lab angle of 50°.

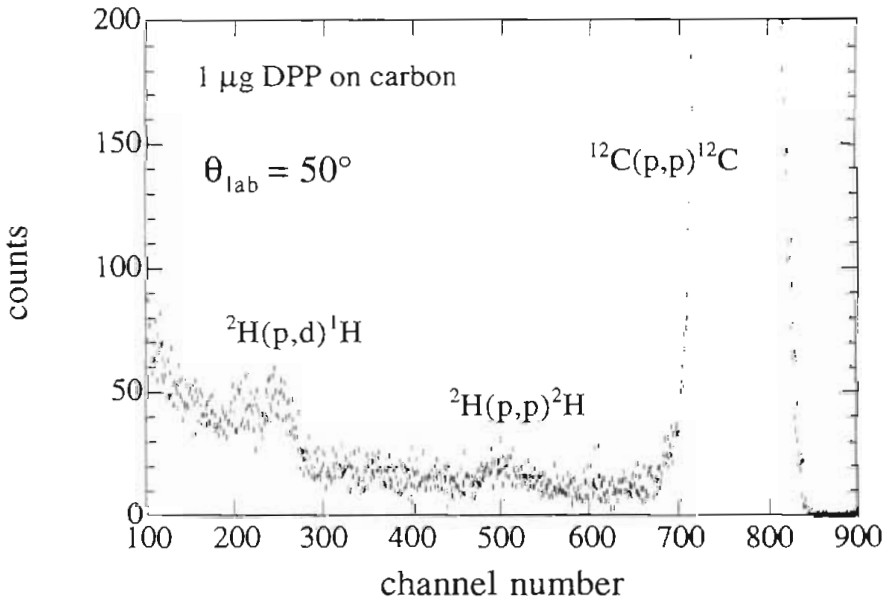

Figure 3.11 Spectrum of carbon-backed DPP target at θ_{lab} = 50°

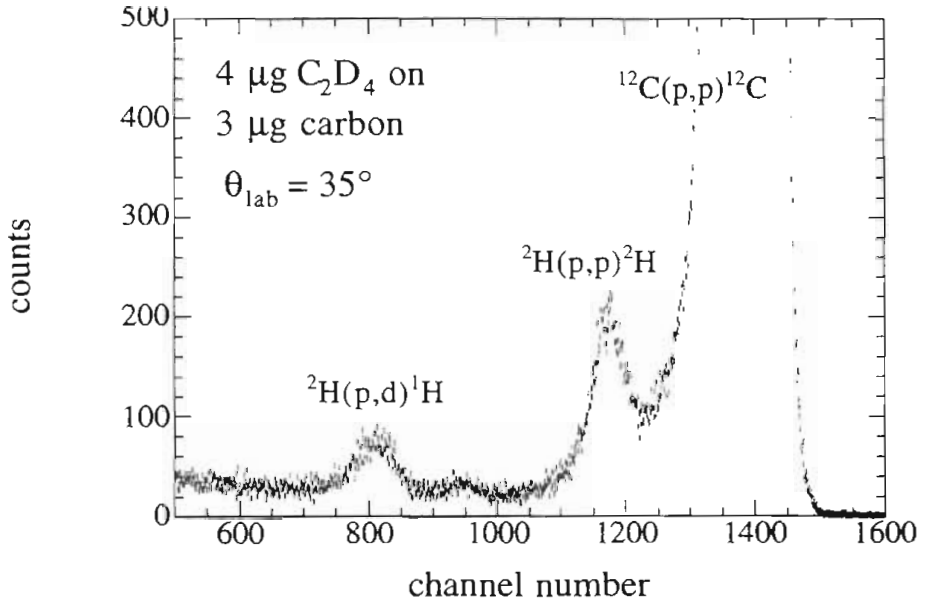

Figure 3.12 Spectrum of carbon-backed deuterated polyethylene target at $\theta_{lab} = 35°$

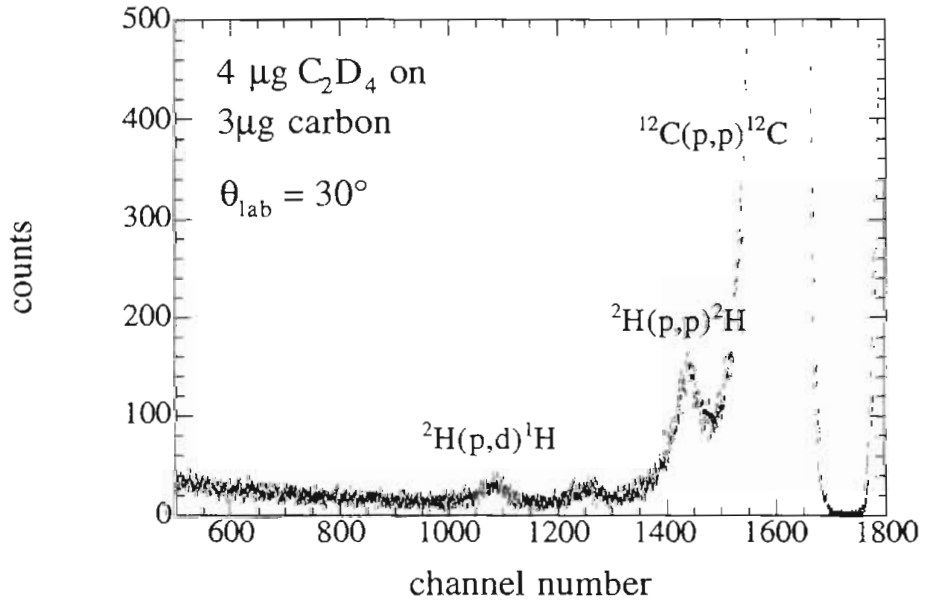

Figure 3.13 Spectrum of carbon-backed deuterated polyethylene target at $\theta_{lab} = 30°$

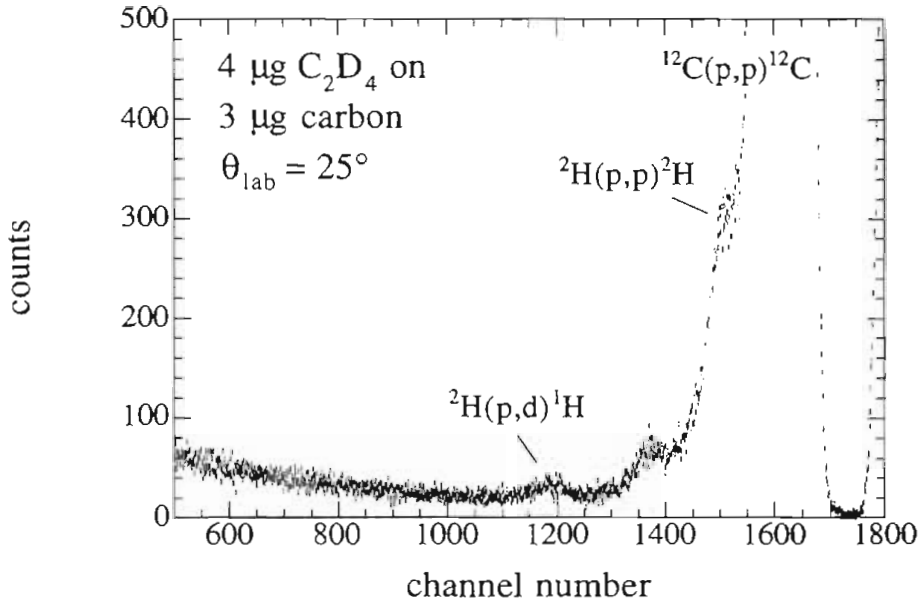

Figure 3.14 Spectrum of carbon-backed deuterated polyethylene target at $\theta_{lab} = 25°$

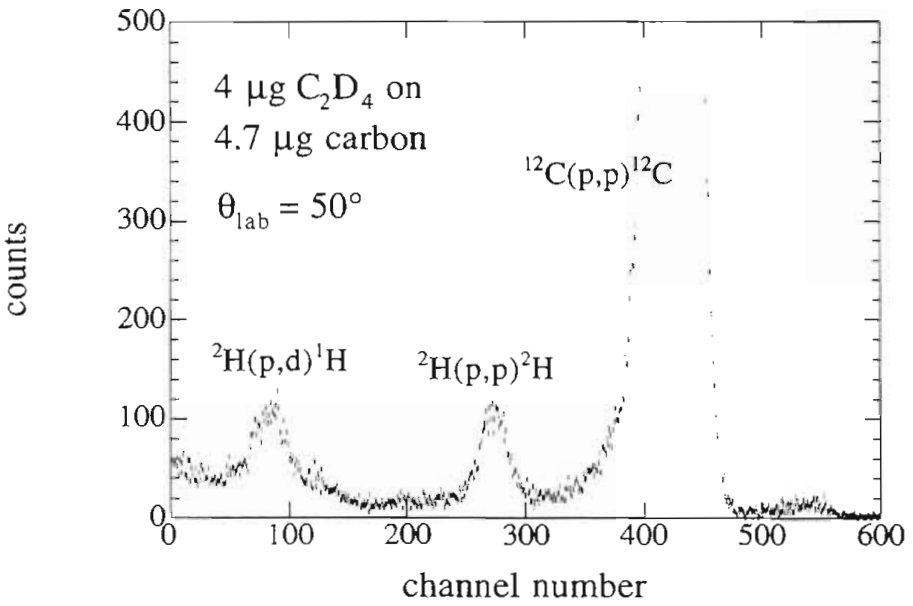

Figure 3.15 Spectrum of carbon-backed deuterated polyethylene target at $\theta_{lab} = 50°$

A series of runs were taken at 10 minute intervals with the target of Figure 3.15 to determine the rate of deuterium depletion and carbon accretion. These results are shown in Figures 3.16 and 3.17 respectively.

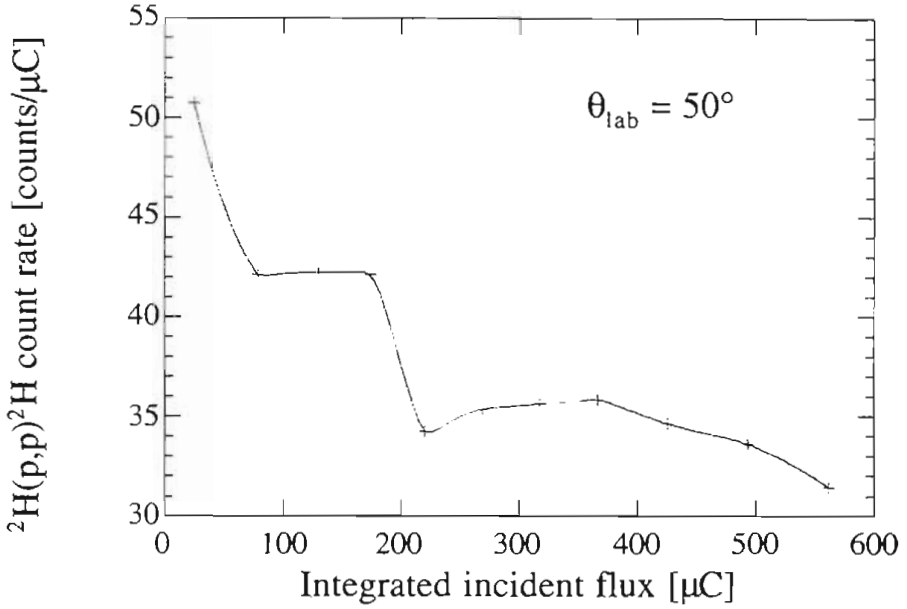

Figure 3.16 Dependence of p–d count rate on integrated incident charge for a carbon-backed 4 μg/cm^2 C_2D_4 target: The curve is intended to guide the eye.

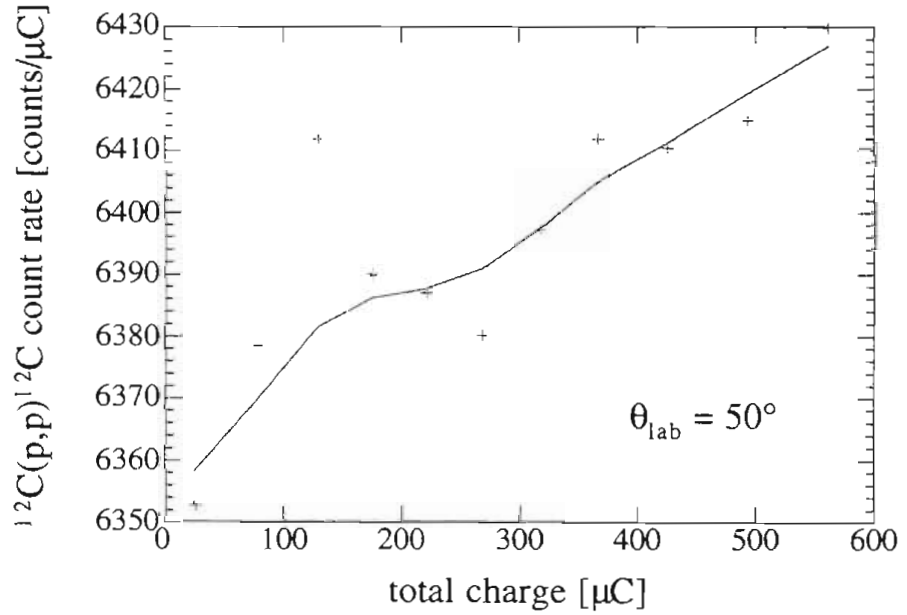

Figure 3.17 Dependence of p–^{12}C count rate on integrated charge for a carbon-backed 4 μg/cm^2 C_2D_4 target: The curve is to guide the eye.

The thickness and straggling width of a target consisting of 6 $\mu g/cm^2$ of deuterated polyethylene evaporated onto a 2.9 $\mu g/cm^2$ carbon backing was measured by proton scattering at E_{nom} = 330 keV and $\theta_{lab} = 50°$. After deconvoluting the electronic noise, the FWHM energy width of the deuterium peak was found to be 13.0 keV. The deuterium thickness was 6.1×10^{16} nuclei/cm^2 and the carbon thickness was 6.8×10^{17} nuclei/cm^2. The peak widths for this type of target are unacceptably large. Contemplation of the spectra in Figures 3.13 through 3.15 make it clear that it would be very difficult to measure the yield of the $^2H(p,p)^2$ peak with the requisite accuracy by using carbon-backed polymer targets.

3.3.2 Amorphous deuterated carbon targets

Elemental carbon occurs naturally in two stable forms: graphite, which is a disordered, soft, opaque semi-metal; and diamond, which is crystalline, extremely hard, transparent and highly insulating. A nearly continuous range of metastable phases exist between these two extremes [Mey86], all subsumed under the names "diamond-like carbon" (DLC), isotropic carbon (i–C), amorphous carbon (a-C), "hard carbon", "cracked" carbon, etc. The designation a-C will be used in what follows.

Material of this type has been made inadvertently for centuries. It is formed when sufficient energy is supplied to a sample of graphite to transform a substantial fraction of the *sp*-2 chemical bonds to *sp*-3 bonds. This process can be catalyzed by the presence of hydrogen . When formed at very low energies, this material may take the form of common soot. Higher energies, such as might be present when an oil diffusion pump is left running without cooling water, lead to the formation of an extremely hard deposit that adheres very strongly to a large number of base materials. Yet higher energies will promote the creation of extremely hard insulating films which have many of the characteristics of diamond. For this reason they have elicited much commercial interest [Mey80, El-H88, Des94, Hol79, Pou86, Tan91].

It was noted that films of this type, created by "cracking" or dissociating a hydrocarbon gas in a plasma and accelerating the radical

fragments towards a substrate, made ideal stripping foils for tandem accelerators, especially for use with heavy ion beams [Sof82, Tol82, Gal82, Whi79, Tai80, Tai81, Hüc81]. Such films, commonly referred to as "cracked ethylene" films—although they can be made using nearly any hydrocarbon as a precursor gas[25]—were found to be uncommonly hardy under ion bombardment [Lea82]. For this reason, they are often used as tandem stripper foils for accelerating heavy ions.

A problem encountered by a number of workers, whether engaged in the production of heavy-ion stripper foils or components of semiconductor devices, was that such films contained an extraordinary amount of hydrogen [Hol78, Hol79, And79]. This was especially a problem for those seeking to make dielectric coatings, since the hydrogen interfered with the useful electrical and optical properties that were sought. Commercial researchers have obviated this problem either by annealing the hydrogen out of the device at high temperatures, or by adopting new methods which do not rely on hydrogen to catalyze the reaction. Before these solutions were adopted, however, a great deal of research was conducted into the deposition conditions that would result in the smallest possible hydrogen concentration.

Since it was apparent from the work on heavy-ion stripper foils that relatively thin self-supporting a–C films could be manufactured by the relatively simple glow-discharge technique, it seemed worthwhile to utilize the tremendous amount of commercial research undertaken to eliminate hydrogen contamination in order to create thin films which had very high hydrogen concentrations, i.e., precisely those which would make poor commercial coatings. The results can be summarized as follows [Tan91, Ker87, Des94] : The hydrogen concentration goes up as the deposition temperature goes down. It goes up as the deposition power, or bias voltage, goes down. It goes down as the gas pressure in the plasma reactor goes up. The hydrogen concentration in the film decreases as the free hydrogen content of the plasma increases [Rev93].

---

25 In addition to ethylene; propane, butane, acetylene and methane have been used to grow such films.

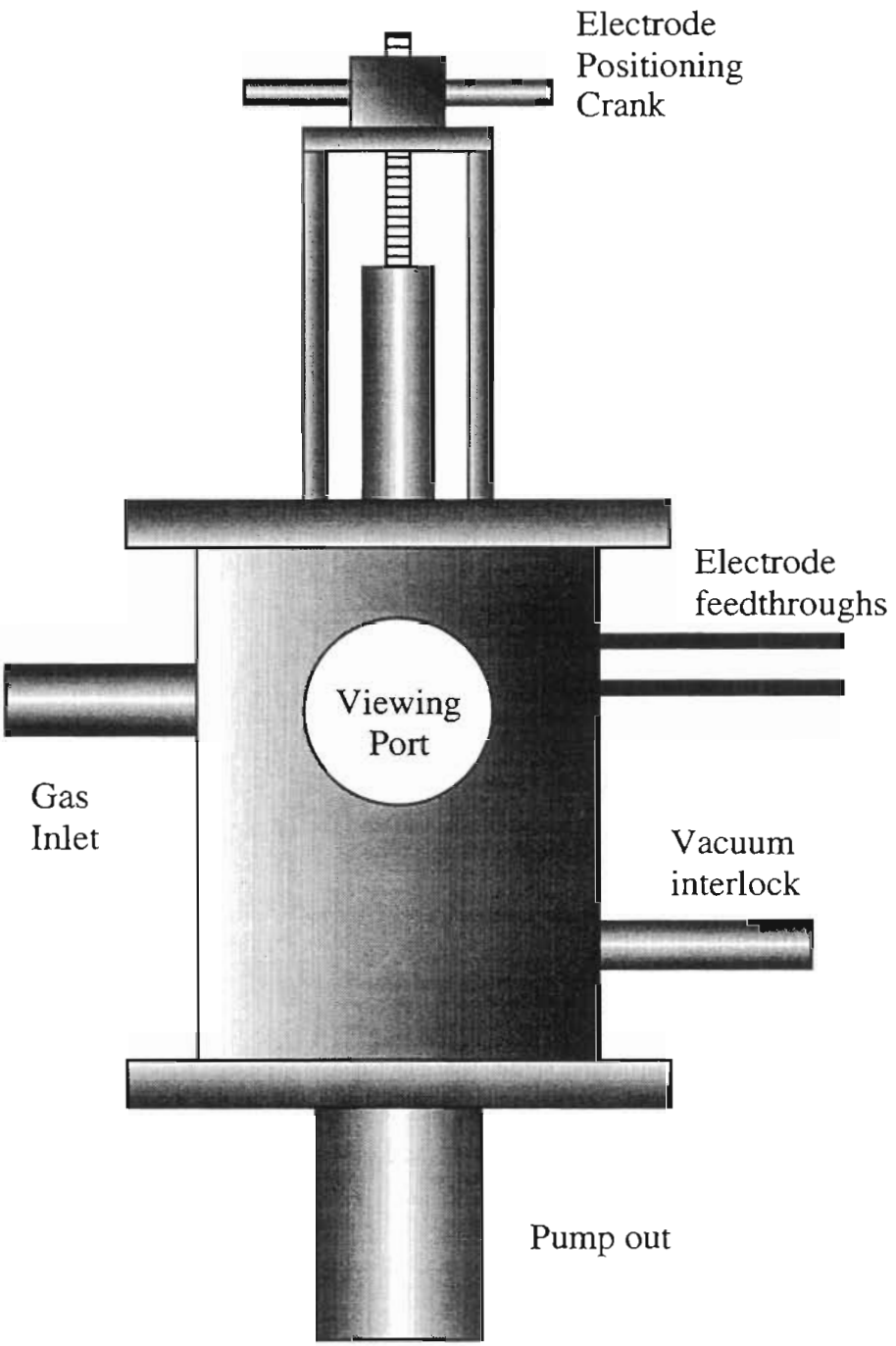

Figure 3.18 TUNL/UNC Plasma Assisted Chemical Vapor Deposition chamber exterior

A small DC glow-discharge plasma reactor was designed and built. A simplified view of the exterior of the device is shown in Figure 3.18. A schematic cutaway of the interior is shown in Figure 3.19. The plasma

chamber is 36 cm in diameter by 29 cm in height. The electrodes were polished to a high finish so as to inhibit sparking within the chamber. The device was initially equipped with a water cooled plate which served as a heat sink for a Peltier cooling block that could be attached to the base of the negative electrode, but it was found that the electrodes did not heat up in use and the cooling lines, being very bulky, made the device difficult to service.

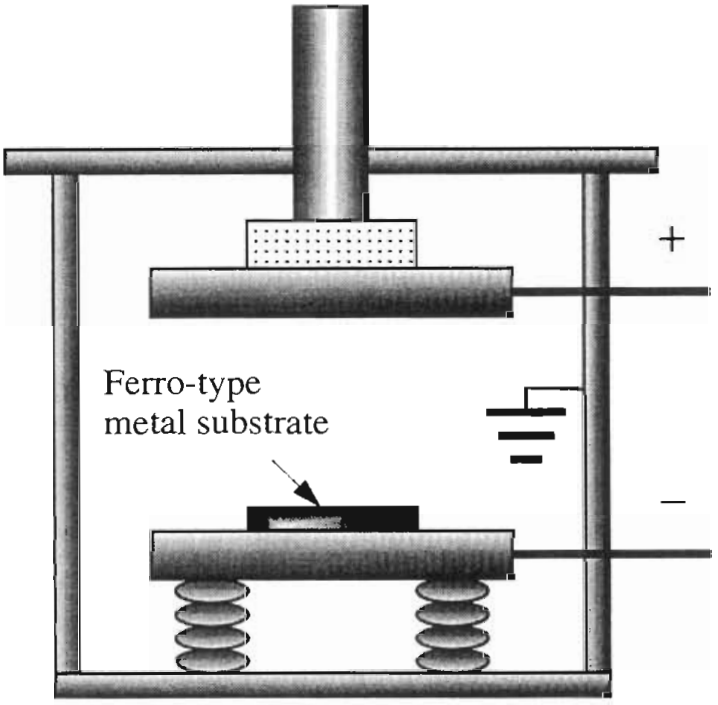

Figure 3.19 Interior view of TUNL/UNC Plasma Assisted Chemical Vapor Deposition chamber

A 1.3 mm × 7.6 mm slide of ferro-type metal (chromium plated iron) serves as the substrate. The slide is first coated with a 400 Å thick layer of NaCl, which serves as a release agent, and is then placed on the lower electrode. The plasma chamber is evacuated to roughly 10^{-6} torr with an oil diffusion pump. After purging the gas lines, the diffusion pump gate valve is closed and a roughing valve is opened, allowing the chamber to be continuously pumped at a high rate of flow. A thin stream of deuterated methane gas is continuously bled into the chamber through a leak valve attached to the gas manifold. When the steady-state pressure

is optimal, high voltage of ±100 VDC is applied to the electrodes by a Regatron tube power supply of Sputnik-era vintage. The potential is increased until a plasma ignites between the electrodes. This usually occurs when the inter-electrode potential is about 400 V. The plasma current is read from a small current meter connected in series with the electrodes. The high voltage may then be raised until the optimum operating conditions are achieved.

The maximum output of the Regatron is 600 VDC at 600 mA. The electrodes are connected symmetrically with respect to ground: This minimizes sparking to the interior of the chamber, which is held at ground potential. Sparking was also inhibited by placing a pair of high-power, low-impedance resistors in series with the electrode power supply. This prevents cascades from developing out of transient current peaks generated by plasma instabilities, such as random sparking events. The thickness is monitored by summing the average charge collected over short time intervals. The deposition time is measured with an electric lab timer. For the targets used in the p–d experiment, the deposition time was between 20 and 40 minutes.

After completing the deposition, the chamber may be brought up to atmospheric pressure using either argon or nitrogen, supplies of which are connected to the PACVD gas manifold. A manual for the TUNL PACVD, "An Illustrated Guide to the Care and Feeding of the TUNL Plasma Assisted Chemical Vapor Deposition System", has been prepared by the author. This manual describes how to prepare the substrates, and gives detailed instructions for operating and maintaining the device. Standard operating parameters are also listed in the manual.

Since these films are extremely thin, it is very difficult to float them from the substrate successfully. Through trial and error, it was found that the best results were obtained by floating the film in a bath of roughly 2–3 liters of water that had been heated to ≈ 55°C: Heating the water both improves dissolution of the release agent and lowers the surface tension of the water. After all of the films have been released into the water, roughly 200-300 ml of ethyl alcohol should be added. The

alcohol further lowers the water's surface tension and for this reason it is important to add the alcohol *after* the film has released from the slide. Otherwise, the films will sink to the bottom of the pan. The films are then floated onto a target ring in the usual manner.

After the film is floated onto a target ring, the ring is placed in a target transport case which is kept in a cooler filled with ice. A shallow pan of dessicant is also placed in the cooler. This procedure allows the residual water and alcohol to evaporate slowly from the film and significantly enhances post-flotation survival. For the targets used in the p-d experiment, the success rate, defined as 1 day survival, was between 1 in 6 and 1 in 10 attempts.

Although the films were very fragile, once in the beam they were remarkably hardy, some lasting over 2 days continuously in the beam. Since the films are highly insulating, excessive charge should not be permitted to build up on the surface: The films may shatter if the accumulated charge sparks to some conducting surface. Figures 3.20, 3.21 and 3.22 show the proton scattering spectra of the target used to obtain nearly all of the data taken at E_{nom} = 330 keV.

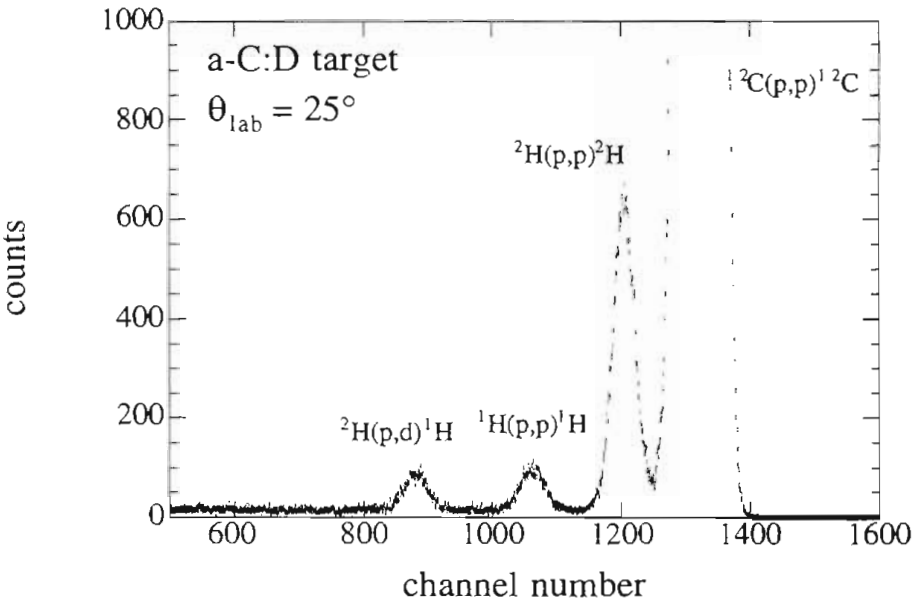

Figure 3.20 Spectrum of a-C:D target at θ_{lab} = 25°

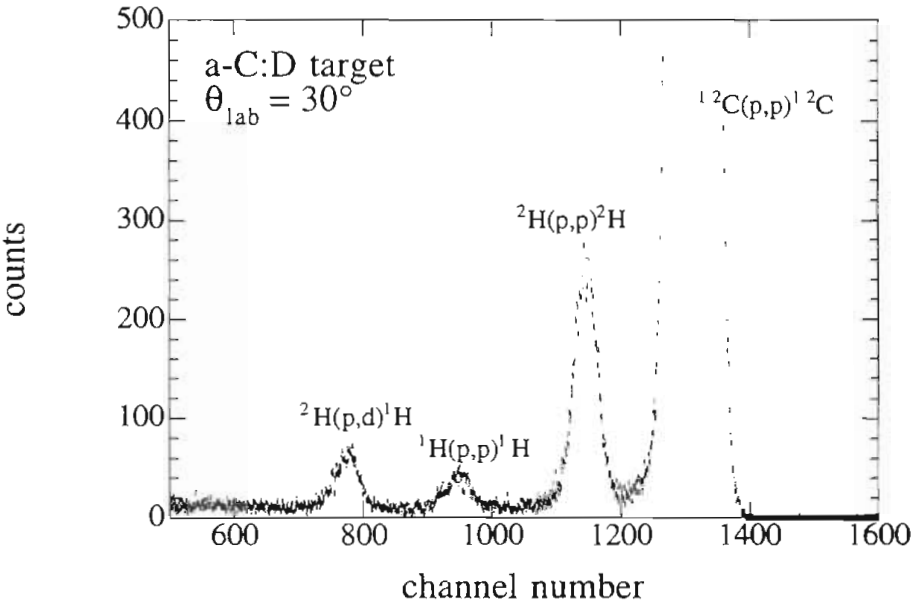

Figure 3.21 Spectrum of a-C:D target at $\theta_{lab} = 30°$

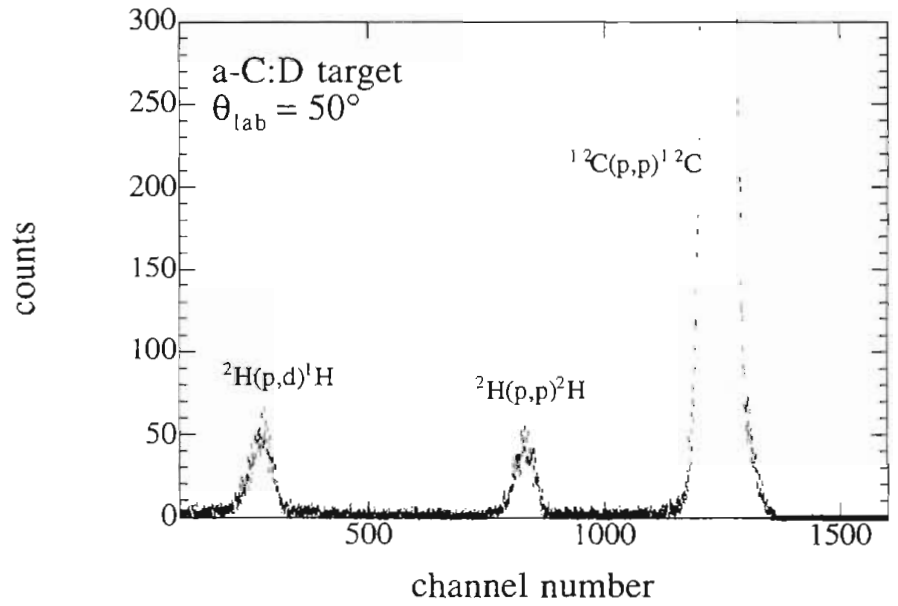

Figure 3.22 Spectrum of a-C:D target at $\theta_{lab} = 50°$

The deuterium thickness for this target is $\tau_d \approx 1.1 \times 10^{17}/cm^2$ while the carbon thickness is $\tau_C \approx 3.3 \times 10^{17}/cm^2$. After deconvoluting the electronic width, the FWHM of the p-d peak was determined to be 6.4 keV.

3.4.1 The scattering chamber

The scattering chamber, designed by Prof. E. J. Ludwig, can be operated at a potential of 200 kV with respect to ground, although this feature was not used in the p–d experiment. Partly in order to minimize potential gradients, it is very large, measuring 107 cm in diameter. Three small turbo-pumps are mounted on the bottom of the chamber in such a way that a hemispherical dome can be drawn up to enclose them, thereby providing a smooth contour to further minimize electric fields. It stands upon a trio of ceramic insulators.

Because of its size, the angle-setting marks are difficult to see. For this reason, large magnifying lenses were fixed in the line of sight between the angle-setter and the setting marks. The detectors are mounted upon 66 cm diameter rotating plates set in the floor and lid of the chamber, permitting independent rotation of the left and right detectors. Freon lines run into the detector holding racks, which under ideal conditions provide cooling for the detectors. A target rod with 5 slots for holding target rings runs through the center of the chamber. During the experiment, the target rod was held at +100 V and connected in parallel with the main beam integration, provided by a Faraday cup.

A pair of monitor detectors are emplaced symmetrically with respect to the beam axis, one on the roof, the other on the floor of the chamber. The monitor detector holders are set at an angle such that they "look" over the detectors mounted on the rotating plates, directly at the target. In this way, the rotating detectors can be placed directly in front of the monitors without impeding their view. The purpose of the monitor detectors is to measure the changing composition of the target from a fixed location. A drawing of the chamber interior emphasizing the monitor lines of sight is shown in Figure 3.23.

A pair of horizontal and vertical collimator slits are mounted inside the entrance snout in the path of the beam. The edges of these collimators were beveled to an edge thickness of roughly 200 μm. Typical pressures inside the chamber during experimental runs was a few

times 10^{-6} torr. During the course of the experiment, the only major problem associated with the use of this chamber was the great difficulty we experienced in attempting to align it properly. This difficulty was due partly to the mass of the chamber, supported as it was upon a triad of relatively brittle insulators. It was also partly due to the fact that a 200 kV acceleration tube forms the input beamline to the chamber. Simultaneously achieving a good visual alignment and an adequate vacuum seal oftentimes seemed as arduous as docking a pair of spacecraft.

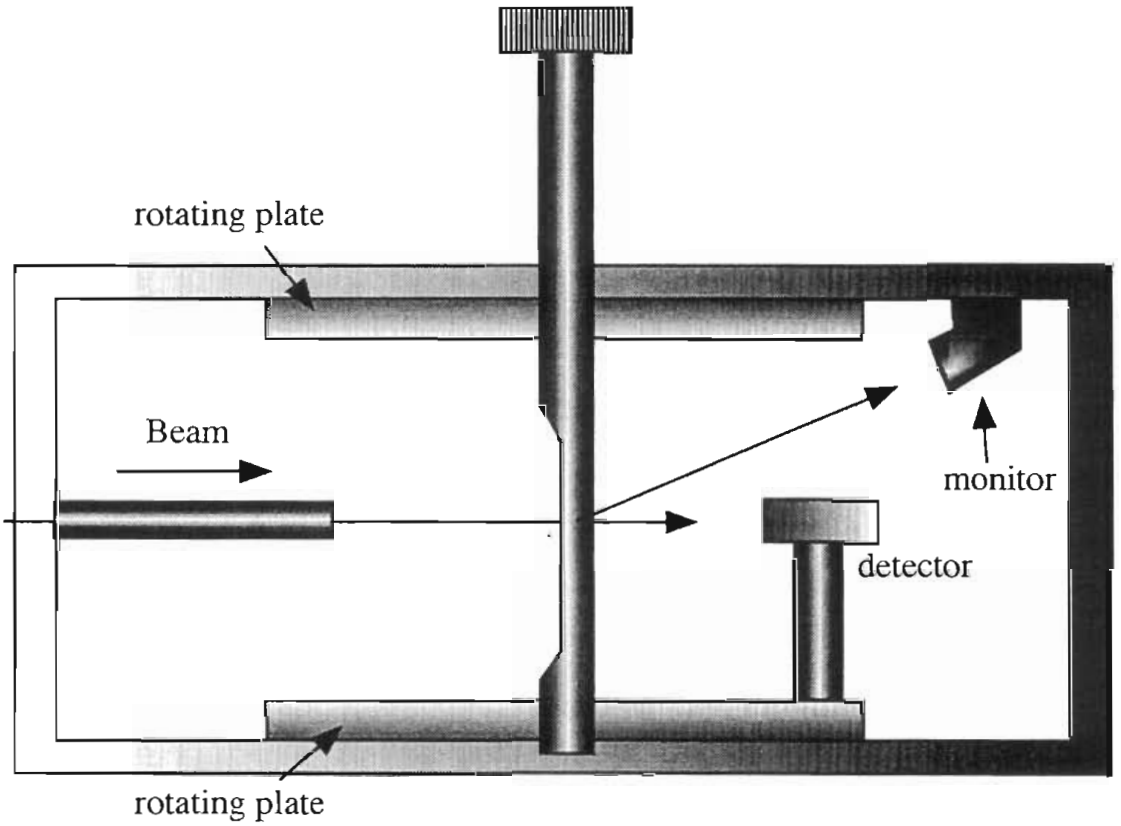

Figure 3.23 High-voltage scattering chamber

3.5.1 Methodology

In the run of May, 1994, data were taken with a single spectrum detector at nominal laboratory scattering angles of 20°, 25°, 30°, 40°, 45°, 50° and 60°. The cross sections for center-of-mass angles in the backward hemisphere were determined from the yield of recoil deuterons at these same angles. As previously noted, a number of runs were taken

at each angle, with the angle being re-set between each run. The left monitor detector was placed at 37.5° while the the right monitor detector was located at 30°. Sufficient counts were taken to ensure less than 1.5% statistical uncertainty in the detector with the lowest number of counts in the peak of interest.

The standard procedure for correcting for the dead-time of the data acquisition system calls for pulsed signals to be routed through the same electronic circuit traversed by the true data signal. These signals appear in the spectrum as a well-resolved "pulser" peak. By taking the ratio of the number of counts routed through the pathway to the number that appear in the pulser, the fraction of time that the data acquisition system is unresponsive can be determined—it is just the reciprocal of this dead-time correction ratio. The experimental yield is then rectified by multiplying by this dead-time ratio.

It was found in the course of a preliminary run that when the count rate was very high, a large number of spurious counts appeared in the pulser peak. In some cases, so many additional counts were registered that the dead-time factor became less than one. By plotting the dead-time correction factor against the counting rate, it was found that as the apparent dead-time correction approached 10%, increasing the counting rate actually decreased the apparent dead-time factor. It was initially suspected that this effect was due to pile-up—the displacement of counts in the spectrum due to the signal from two or more small-amplitude signals arriving simultaneously and being counted as a single, large amplitude signal.

In an attempt to overcome this phenomenon, a dead-time correction procedure was designed that was identical to the standard dead-time correction method, except that instead of counting the input signals generated by the pulser electronics, the gates generated by the pulser electronics were counted. However, this procedure failed to correct the problem. In fact, it is unlikely that these spurious counts were caused by pile-up, since the background generated in the high count rate spectra did not manifest the regularities characteristic of signal pile-up.

A more likely cause is that random noise signals in the detection circuit were registered as counts when the counting rate was high, because the proliferation of signal gates permitted them to "piggyback" in through the gating circuit. This would account for the essentially featureless character of the background. If this is the case, then the modified dead-time correction circuit would fail to correct the problem, since the spurious signals did not generate any gates. Since it was uncertain at the time whether the modified circuit would resolve this difficulty, the beam current was kept low enough that the dead time corrections were modest, less than 5.5%. Comparison of the dead-times calculated using the standard procedure with that calculated using the modified procedure showed that they differed by less than 10% from one another under these conditions.

Chapter IV: Analysis and Conclusions

"Tout le monde y croit cependant ... car les expérimentateurs s'imaginent que c'est un théoréme de mathématique et les mathématiciens que c'est un fait expérimental ... "

Henrí Poincaré, *on the normal distribution*

4.1.1 Spectral Analysis

Neither the reaction peaks nor the low-intensity background appearing in the p–d elastic spectra can be adequately represented by simple parametric forms like the normal distribution. Furthermore, the statistical processes giving rise to energy losses of particles transiting thin films are so complicated and as yet incompletely understood that it is not at present possible to advance a credible model that predicts any particular analytic or parametric form for the energy distribution describing peak shapes. It was believed at first that the reaction peaks could be resolved by using a deconvolution algorithm to extract the electronic noise from the peaks. A computer code was written for this purpose, but failed to resolve the problem because the electronic noise contributed relatively little to the peak widths.

4.1.2 MuMuRaMa: Multinomial Multinomial Random Markov Chain Analysis

A Fortran code was developed that applied the Gibbs sampler algorithm, described in Appendix E, to infer the expected partition of the spectra into their constituent peaks. Because of the complicated nature of the problem, and because Bayesian image analysis is an unsettled area of research, especially regarding the practical implementation of recent theoretical developments, the algorithm, and especially its Fortran implementation, is not a "finished" product. Nonetheless, despite certain

difficulties and quirks, it represents a high-quality solution to the problem of spectral analysis.

Suppose that the observed data **Y** has the form of a histogram—an integer-valued vector of counts as a function of energy. If the number of counts N in the spectrum is large, then there are an enormous number of ways in which **Y** can be partitioned into the sum of a fixed number K of constituent spectra **Z**. The j^{th} partition has the form

$$\mathbf{Y}^{(j)} = \sum_{n=1}^{K} \mathbf{Z}_n^{(j)} \qquad (4.1)$$

where the index "n" refers to the label of the constituent.

The hypothetical spectra $\mathbf{Z}_n$ represent the spectra that would have been observed had it been possible to somehow discriminate between the counts coming from the different reactions assumed to occur in the interaction of the beam with the target. For most of the p-d spectra, there were five such constituent reactions; $^{12}C(p,p)^{12}C$, $^{2}H(p,p)^{2}H$, $^{1}H(p,p)^{1}H$, $^{2}H(p,d)^{1}H$, and a relatively featureless background spectrum.

The event space from which the data **Y** were drawn, and from which the data **Z** could in principle have been drawn were it possible to observe the distinctions between particles scattered by the various constituent reactions, is the space of all possible partitions of a very large number $M \gg N$ of counts. These counts are divided into $K \times J$ categories, where K is the number of constituents and J is the dimension of the vector **Y**; i.e., the number of channels in the spectrum. Each category contains $g_{(i,n)}$ counts representing events in which the product of reaction type "n" would have been observed in energy bin "i", were it possible to discriminate between products of different reactions. The parameter $\varphi_{(i,n)} = \frac{g_{(i,n)}}{M}$ denotes the primitive probability, or estimate, of observing $z_{(i,n)} = N\varphi_{(i,n)}$ counts of reaction type "n" hypothetically observed in energy bin "i", in a sample of size N.

The following primitive probabilities can also be defined in terms of the population of various categories in the event space.

$$\theta_{(i)} \equiv \frac{g_{(i)}}{M} \equiv \frac{1}{M}\sum_{n} g_{(i,n)}\,, \tag{4.2}$$

$$\omega_{(n)} \equiv \frac{g_{(n)}}{M} \equiv \frac{1}{M}\sum_{i} g_{(i,n)}\,, \tag{4.3}$$

and

$$\pi_{(i\,|n)} \equiv \frac{\varphi_{(i,n)}}{\omega_{(n)}} = \frac{g_{(i,n)}}{g_{(n)}} \tag{4.4}$$

For a sample of size N, in the limit that $N \to \infty$, $N\theta_{(i)}$ is the estimate of the number of counts in channel "i" summed over all reaction types, $N\omega_{(n)}$ is the estimate of the number of counts of reaction type "n", irrespective of channel, and $N\pi_{(i\,|n)}$ is the estimate of the number of counts in channel "i", given that the reaction was of type "n".

Straightforward implementation of the Gibbs sampler implies that the hyperparameter ζ should be taken as the concatenation of the primitive probability vector φ and the latent data vector **Z**. However, this does not lead to useful results, since there is no good way of providing direct constraints upon φ. Constraints can be imposed indirectly, however, since each of the primitive probabilities defined in equations (4.2) – (4.4) can themselves be constrained in some manner. The most useful constraints are those that can be imposed on $\omega_{(n)}$ and $\pi_{(i|n)}$. The constraint information contained in $\theta_{(i)}$ is more directly expressed through the conditional dependence on the data **Y**, since y_i is the experimental estimate of $N\theta_{(i)}$. The hyperparameter ζ is therefore taken

as the concatenation of the latent data **Z**, the primitive parameter vector ω and the primitive parameter vector π.

The distribution of the latent data elements $z_{(\bullet,\bullet)}$ obtained by sampling without replacement from this space has the form of a hypergeometric function. However, since it is assumed that $M \gg N$, then for sufficiently large N, sampling with and without replacement are equivalent. Therefore the distribution of $z_{(\bullet,\bullet)}$, conditional on φ and N, has the form of a multinomial distribution. The conditional dependence on the data **Y** is imposed by requiring that equation (4.1) holds.

The distribution of $z_{(i,\bullet)}$ in each channel "i" is also multinomial, so that,

$$z_{(i,\bullet)} \sim Mu(z_{(\bullet,\bullet)}, \varphi_{(i,\bullet)}, y_i) = y_i! \prod_k \frac{\left\{ \varphi_{(i,k)} \right\}^{z_{(i,k)}}}{z_{(i,k)}!},$$

with

$$y_i = \sum_m z_{(i,m)}.$$

The sample of the latent data $z_{(i,\bullet)}$ can readily be performed using successive draws from a binomial distribution. If the expected value of $z_{(i,m)}$ is large, the binomial variate can be approximated by a sample from the Poisson distribution.

Given an initial set of parameters, $(\omega^{(0)}_{(\bullet)}, \pi^{(0)}_{(\bullet|\bullet)})$, the joint parameter set $\varphi^{(0)}_{(\bullet,\bullet)} = \omega^{(0)}_{(\bullet)} \pi^{(0)}_{(\bullet|\bullet)}$ can be formed. Using this parameter set, sample

$$z^{(1)}_{(i,n)} \sim Mu(z_{(\bullet,\bullet)}, \varphi^{(0)}_{(i,n)}, y_i) \qquad (4.5)$$

for each channel "i" and reaction type "n". By using this sequential sampling method, the latent data sample for each reaction type index in a

given energy channel is automatically conditional on the values of the previously sampled latent data and on the observed data in that channel.

For each of the K reaction types "n", the primitive parameter $\omega_{(n)}$, describing the relative contribution of the n^{th} reaction type, is sampled, conditional on all other parameters:

$$\omega_{(n)}^{(1)} \sim P(\omega_{(\bullet)} | z_{(\bullet,\bullet)}^{(1)}, \pi_{(\bullet|\bullet)}^{(0)}, \omega_{(1)}^{(1)}, \ldots, \omega_{(n-1)}^{(1)}, \omega_{(n+1)}^{(0)}, \ldots, \omega_{(K)}^{(0)})$$

Finally, for each of the L channels "j" and K reaction types "n", the conditional parameter $\pi_{(\bullet|\bullet)}$, representing the "peak shapes", are sampled, conditional on all other parameters.

$$\pi_{(1|1)}^{(1)} \sim P(\pi_{(\bullet|\bullet)} | z_{(\bullet,\bullet)}^{(1)}, \omega_{(\bullet)}^{(1)}, \pi_{(2|1)}^{(0)}, \ldots, \pi_{(L|1)}^{(0)}, \pi_{(\bullet|-1)}^{(0)})$$

$$\vdots$$

$$\pi_{(L|1)}^{(1)} \sim P(\pi_{(\bullet|\bullet)} | z_{(\bullet,\bullet)}^{(1)}, \omega_{(\bullet)}^{(1)}, \pi_{(1|1)}^{(1)}, \ldots, \pi_{(L-1|1)}^{(1)}, \pi_{(\bullet|-1)}^{(0)}))$$

$$\pi_{(1|2)}^{(1)} \sim P(\pi_{(\bullet|\bullet)} | z_{(\bullet,\bullet)}^{(1)}, \omega_{(\bullet)}^{(1)}, \pi_{(\bullet|1)}^{(1)}, \pi_{(2|2)}^{(0)}, \ldots, \pi_{(L|2)}^{(0)}, \pi_{(\bullet|(-1,-2))}^{(0)})$$

$$\vdots$$

$$\pi_{(L|2)}^{(1)} \sim P(\pi_{(\bullet|\bullet)} | z_{(\bullet,\bullet)}^{(1)}, \omega_{(\bullet)}^{(1)}, \pi_{(\bullet|1)}^{(1)}, \pi_{(1|2)}^{(1)}, \ldots, \pi_{(L-1|2)}^{(1)}, \pi_{(\bullet|(-1,-2))}^{(0)})$$

$$\vdots$$

$$\vdots$$

$$\pi_{(1|K)}^{(1)} \sim P(\pi_{(\bullet|\bullet)} | z_{(\bullet,\bullet)}^{(1)}, \omega_{(\bullet)}^{(1)}, \pi_{(2|K)}^{(0)}, \ldots, \pi_{(L|K)}^{(0)}, \pi_{(\bullet|-K)}^{(1)})$$

$$\vdots$$

$$\pi_{(L|K)}^{(1)} \sim P(\pi_{(\bullet|\bullet)} | z_{(\bullet,\bullet)}^{(1)}, \omega_{(\bullet)}^{(1)}, \pi_{(1|K)}^{(1)}, \ldots, \pi_{(L-1|K)}^{(1)}, \pi_{(\bullet|-K)}^{(1)})$$

This completes one cycle of the Gibbs Sampler. A new hyperparameter set $\varphi^{(1)}$ is then constructed, and the procedure reiterated, starting with a re-sampling of the latent data according to (4.5).

The χ^2 and log-likelihood functions are calculated every 20 iterations, using the data y_j and the expectation values $\langle N\theta_{(j)} \rangle$. At some point the analyst will note that the log-likelihood score is stationary with respect to continued iterations. At this point the analyst may choose to begin evaluating the partitions, following which samples from the latent data vector **Z** are stored every H iterations, where H is set by the user. This provides a means of calculating both the expectation of the predictive density of the latent data spectra, conditional on the observed data, as well the expectation and variance of the total yield for each isolated spectra: These comprise the principle results of the analysis.

The samples from the conditional distributions for the parameters π and ω are performed by using an acceptance/rejection method: A new value of the parameter is selected and the ratio of the new and old conditional distributions is formed. The new value is accepted or rejected according to the criteria imposed by the Metropolis-Hastings algorithm [Has70]. All factors that depend only on the common, "conditioning", parameters cancel in the ratio. This makes the method computationally tractable.

Like the transition operator for the Gibbs sampler, The Metropolis-Hastings transition operator is a Markov operator [Gem84]. But while the correlation between samples for the Metropolis-Hastings algorithm persists over only a single transition, it is not clear how the correlation range of the Gibbs sampling operator is influenced by the correlation range of the transition operator used to generate the single-site updates. Thus, there is at present no formal means of determining how small the data sampling frequency parameter H can be made. For want of better understanding of this matter, in most sample runs, H was arbitrarily set to 5. This permits the analysis to be completed in a reasonable period of time. However, it cannot be guaranteed that successive samples are then uncorrelated.

Two separate sampling routines were developed, permitting different types of constraints to be placed on the conditional probabilities

that determine the shape of each reaction peak. In one routine, the shape distributions of all but the p–C peak and the background peak were taken as normal distributions. Then $\pi_{(j\,|\,\bullet)} = \mathrm{No}(x_{(j\,|\,\bullet)},\sigma_{(j\,|\,\bullet)})$ for these peaks, where x and σ are the mean and variance of the normal distribution, respectively. The p–Carbon peak and the background peak were allowed to vary freely, with the sole constraint that they be unimodal, with fixed modal channel. In the second routine, the "unimodal but otherwise free" conditions were applied to all peaks.

At first, both routines were used sequentially for each analysis. The first routine was used to determine an approximate estimate of the distribution. This approximate solution was used to generate a prior, which had the form of a Dirichlet distribution, $\mathrm{Di}(\mathbf{Z},\alpha)$, where the Dirichlet parameter vector α was proportional to the solution $\mathbf{Z}'$ of the first stage, e.g., $\alpha = \alpha\mathbf{Z}'$. This prior was then used in the second stage, in which the unconstrained parameterization was applied. The global parameter α, which took on values between 0 and 1, fixed the "rigidity" of the prior in constraining the second stage solutions. It was determined by the χ^2 score of the first-stage fit. Figure 4.1 shows a typical reaction spectrum at a nominal lab scattering angle of 25°.

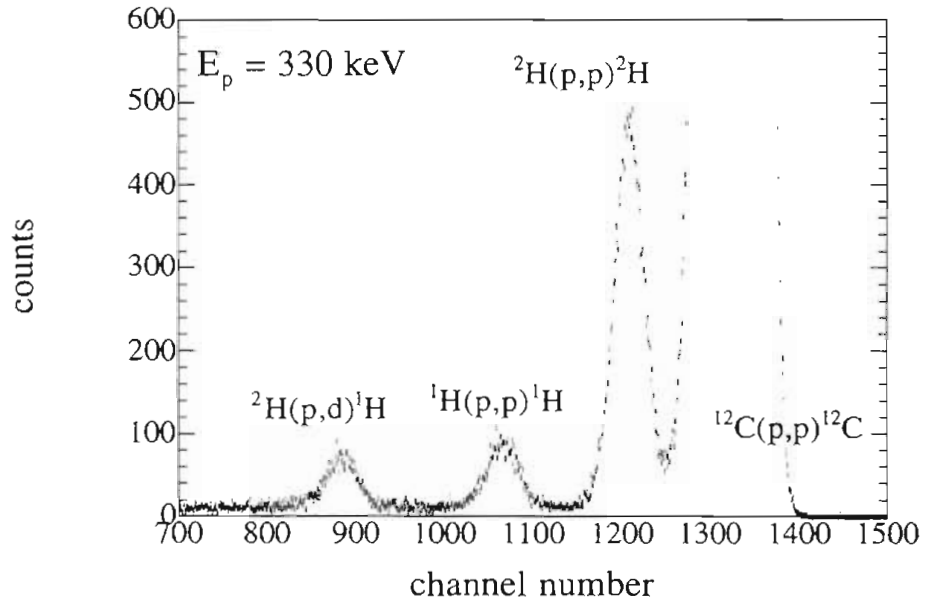

Figure 4.1 p–d spectrum at $\theta_{lab} = 25°$.

Figures 4.2 and 4.3 depict the analyzed $^{12}C(p,p)^{12}C$ spectrum at two different scales. The peak shape's departure from normality is evident in the close-up perspective of Figure 4.3.

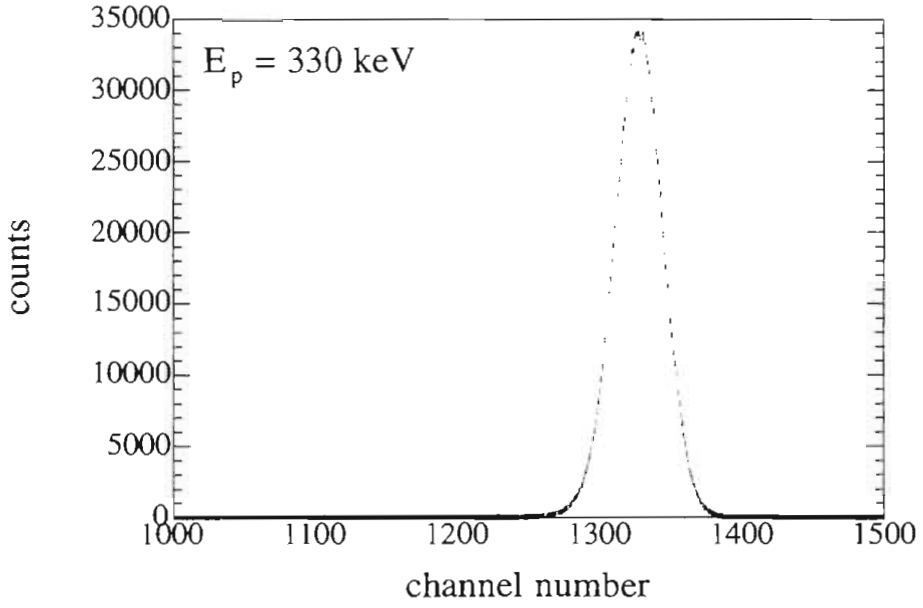

Figure 4.2 Analyzed $^{12}C(p,p)^{12}C$ peak at $\theta_{lab} = 25°$

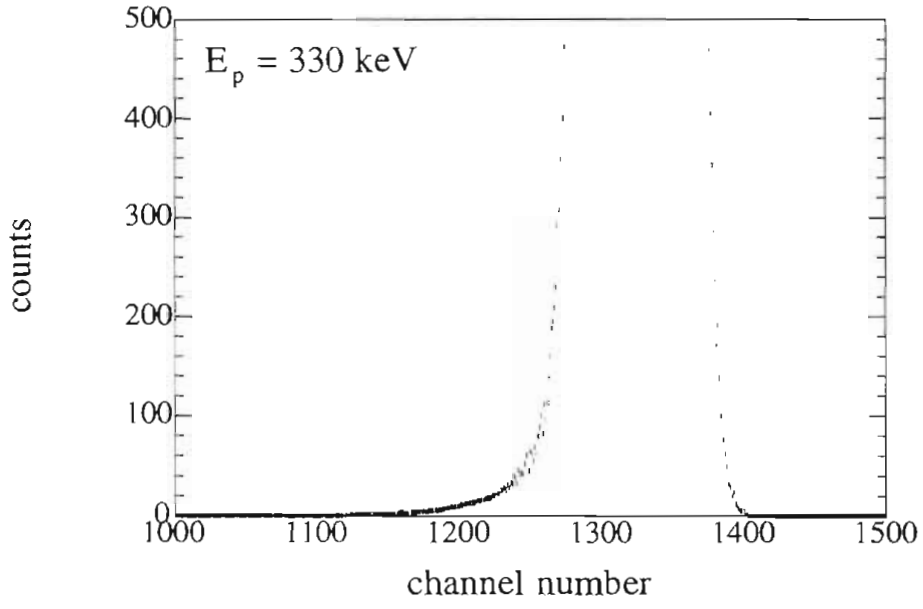

Figure 4.3 Detail of analyzed $^{12}C(p,p)^{12}C$ peak at $\theta_{lab} = 25°$

Figures 4.4 and 4.5 show, respectively, the inferred direct and recoil p–d reaction peaks at 25°.

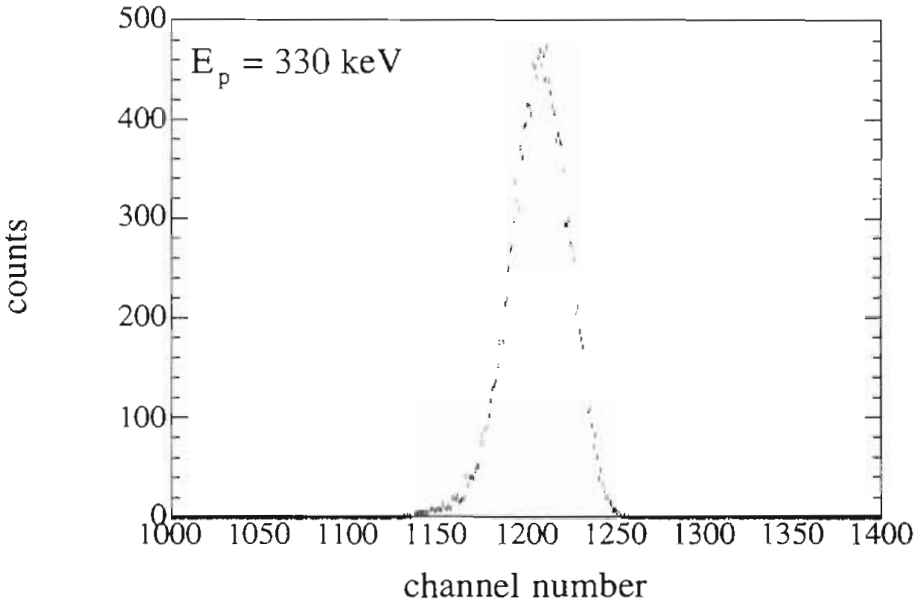

Figure 4.4 Analyzed $^2H(p,p)^2H$ spectrum at $\theta_{lab} = 25°$

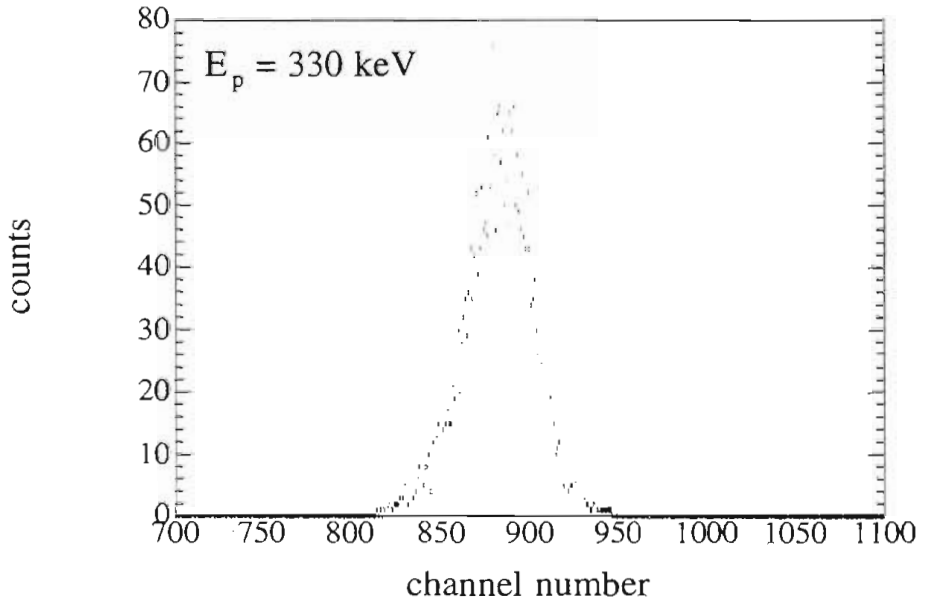

Figure 4.5 Analyzed $^2H(p,d)^1H$ spectrum at $\theta_{lab} = 25°$

4.2.1 Determination of the scattering angle

Because of the strong angular dependence of the p–d reaction, especially at forward angles, it is critical to know the scattering angle accurately. If only relative cross sections are available, the scattering angles for any of the spectra can be determined in two steps.

In the first step, the experimentally determined relative cross sections for the $^{12}C(p,p)^{12}C$ reaction are calibrated with respect to R-matrix calculations of this cross section based upon the formalism of [Lan58] and the R-matrix parameters of [Mey76][26]. The R-matrix code was written by the author and incorporated a program for calculating Coulomb penetrabilities developed by W.J. Thompson of the UNC–CH faculty. The code was tested by comparing the output values with $^{12}C(p,p)^{12}C$ cross sections measured near the 424 keV S-wave resonance [Mey94], upon which the parameterization of [Mey76] was based.

Discrepancies of the order of 5% between the calculation and the data were found near the resonance energy at angles backward of 90°. It is believed that these discrepancies arise from differing values of the fundamental constants and physical parameters used in the present code and the code used in the excitation function fit [Tho95]. In any case, errors of this magnitude are not likely to present difficulties at the lower energies and more forward angles at which the calibration takes place. In fact, comparison between the R-matrix calculation and calculations of the $^{12}C(p,p)^{12}C$ Rutherford cross section show that the latter is a valid approximation to better than 0.5% over the angular region at which this experiment was conducted.

Angular distributions for the $^{12}C(p,p)^{12}C$ elastic scattering reaction were measured at a number of small angles on either side of zero degrees at the nominal beam energy of 330 keV, using a thin carbon target (2.7 ± 0.3 μg/cm^2). By measuring data symmetrically with respect to the

---

26 Revised values of some of these parameters are given in [Mey77]. The code was designed to incorporate all of the energy levels given in [Mey76], but in the actual calculations, the negative energy state was not used.

zero-crossing, the global angular offset could be inferred. The yields in the various detectors were normalized with respect to dead-time corrections, which were never more than 5.5%. The relative yields were formed by dividing the dead-time corrected yield in the rotating detector by the sum of the dead-time corrected yields in the fixed monitor detectors.

At least three runs were taken at each angle setting[27], and the angle was re-set between each run. A composite yield for each angle was formed by combining the data from each run according to a normal model where the weight functions were purely statistical. It should be noted that this is not generally a valid procedure for data that cannot be presumed to be drawn from identical sample spaces. However, since the statistical weights for each run at a given angle were roughly equal, little bias was introduced by this approximation. The composite relative yields found in the zero-crossing measurement are shown in Table 4.1. The positive angular direction was taken to be clockwise from zero.

Table 4.1: Relative yields from zero-crossing measurement

θ [deg]	DTC monitor normalized yield [arb units]
+14.00	21.31 ± 0.100
+17.00	9.560 ± 0.0357
+20.00	4.777 ± 0.0169
+23.00	2.767 ± 0.0114
+25.00	1.964 ± 0.00894
–14.00	14.85 ± 0.0572
–17.00	7.081 ± 0.0297
–20.00	3.780 ± 0.0163
–23.00	2.211 ± 0.00991

In order to obtain starting values for the fit to the $^{12}C(p,p)^{12}C$ cross section, this angular distribution was first fit to a generic symmetric

27 At +14°, only 2 runs were taken.

distribution[28] using the built-in fitting routine of the Kaleidagraph spread-sheet software. The fit was run twice, yielding angle offsets of

$$\delta_1 = -0.634^\circ \pm 0.006^\circ$$

and

$$\delta_1 = -0.638^\circ \pm 0.007^\circ .$$

Although these values were very consistent with one another, we desired to use a sampling-based fitting routine for the final value of the offset . This would allow us to fit the function to a realistic fitting function, rather than simply an ersatz variation and hence, simultaneously fit the angle offset, the energy and the normalization constant. It was noted in [Tho92] that the normalization constant for the data is not, in general, equal to the reciprocal of the normalization constant for the fitting function. Directly fitting the data normalization constant, however, was problematic because it was not clear how to treat the renormalized uncertainties. This dilemma was obviated by renormalizing the fitting function instead, but this poses no essential difficulty since the main aim of this exercise is to correlate experimental and theoretical determinations of the angle, and for this purpose it does not matter which one is renormalized.

It was also noted that comparison of the data with the fitting function, using the approximate offset determinations, revealed that the data point at the nominal scattering angle of +20.00° was inconsistent with the rest of the data set. Since the aim of this exercise was not to verify the well-known differential cross section for the $^{12}C(p,p)^{12}C$ reaction for small scattering angles, but rather to calibrate the relative yield determination, this datum was discarded. It was also noted that the data were equally well fit by the Rutherford and R-matrix fitting

---

28 Two such distributions were used; a power law function for the variable $q = |\theta+\delta\theta|$, and a power law function for the variable $q' = \sin|\theta+\delta\theta|$. The results were substantially the same in each case.

functions, which is not surprising since at these angles, numerical comparisons show them to differ by less than a few parts in 10^4. Therefore it was decided to use the Rutherford cross section as the fitting function, since it was computationally less demanding.

A Monte Carlo fitting routine based upon the Gibbs Sampler was written and used to fit the data. A number of trials of this routine were conducted using different starting values. The fitted values for the angle offset were identical. As expected, use of the Rutherford cross section almost completely eliminated what little independence existed between the fitted values of the energy and normalization constants. Indeed, were it not for the kinematic shifts, they would exhibit complete functional dependence on one another. The following sets of parameters were found.

Table 4.2: Fitted angle offsets and energy/normalization correlates

δ [degrees]	E_p [keV]	C_{norm} $[(mb/sr)^{-1} \times 10^{-6}]$	χ^2
-0.641 ± 0.007	311.96 ± 1.06	$8.1463 \pm .0549$	0.382
-0.641 ± 0.007	312.45 ± 1.44	$8.1724 \pm .0754$	0.381
-0.641 ± 0.007	324.30 ± 3.95	$8.8044 \pm .2150$	0.383

One can use, for the purposes of correlating theoretical and experimental cross sections by angle, any energy/normalization constant pair one chooses. The resulting cross sections are identical to within a few parts in 10^3.

4.3.1 Determination of the mean reaction energy

A number of methods were used to try to determine the nominal reaction energy. In the first method, a 2.7 $\mu g/cm^2$ carbon target was put in the beam path. With the detector kept in a fixed location, the gain of the Minitandem power supply was varied between DVM = 9.971 and DVM = 7.972 in five steps in the first calibration sequence, and between DVM = 9.972 and DVM = 7.200 in six steps in the second calibration sequence. Two energy calibration sequences were performed because

nearly immediately following the first calibration procedure, the Minitandem stripper foil broke. Upon replacement, it was noted that all of the centroids had shifted by roughly 35 channels, corresponding to a shift of roughly 7 keV. This gives some indication, incidentally, of the particles' energy loss in the collodion coating.

It was hoped that each calibration run would provide two sets of indendent information; the variation of the proton-carbon centroids with Minitandem potential, and the variation in proton-carbon yield with Minitandem potential. The combination of these two sets of data would have allowed us to uniquely infer the offset energy—the energy prior to acceleration—as well as the gain and offset of the amplifier, given no more information than the scattering angle and the Minitandem gain. However, it was found that the determination of the absolute reaction yields was not credible because carbon built up on the target continuously throughout the run. The centroid information alone does not uniquely determine the energy offset, and the amplifier gain and offset.

Upon analysis, it was also found that the second energy calibration was flawed. One would expect, for instance, to obtain reasonable consistency with the results of the first energy calibration after making a first-order correction for the Minitandem foil thickness, but this was not the case. Furthermore, the kinematic shifts between the p-^{12}C and p–d centroids were inconsistent with any reasonable estimate of the reaction energy. It was at last determined that the angle was set incorrectly during this calibration run: Rather than being at 24.36°—the angle that one would expect on the basis of the setting recorded in the lab book after correcting for the global angle offset—the angle was actually at $21.97 \pm 0.04°$.

Determining this angle was not difficult. Since the energy and normalization constant inferred from the ^{12}C(p,p)^{12}C relative cross section data are strongly correlated, it is sufficient to use any pair of these parameters from Table 4.2: they are all consistent with the data. The angle at which the energy calibration was performed was then inferred by means of a Monte Carlo sampling code that fit the observed yield from

the initial calibration run to the renormalized Rutherford cross section, (calibrated to the zero-crossing data), as a function of scattering angle. The result obtained did not depend upon the starting value for the angle. The uncertainty in the angle determination is entirely due to statistical uncertainty in the relative yield.

Knowledge of the scattering angle at which the energy calibration data were measured is sufficient to infer the amplifier gain, given a very reasonable model. The model accounts for energy losses in the Minitandem stripping foil, which is taken to be 2.4 $\mu g/cm^2$ thick. The carbon target is assumed to be 2.7 $\mu g/cm^2$ thick. The inferred amplifier gain is not sensitively dependent on these values. The incident particles are assumed to scatter midway through the target. The result is not critically dependent on this assumption either, especially at small angles. After suffering an energy shift due to kinematic factors, the particles then transit a thickness of the foil given by

$$t = \frac{\tau}{2\cos\theta},$$

where τ is the target thickness.

The pulse height defect for protons in a silicon detector with a 500Å window was numerically calculated using physical parameters determined with the TRIM program, which simulates the atomic collisions of ions in matter, according to a method proposed in [Len90]. The resulting function, giving the apparent energy of a pulse as a function of its true energy, was fit over a range from 100 keV to 360 keV to a simple linear form.

$$E_{apparent} = -8.3302 + 1.0109 \times E_{true}$$

where both energies are in keV. One can then show that the centroid C depends upon the Minitandem DVM setting, V_{DVM}, according to

$$C = G_{amp}G_{acc}K_1 V_{DVM} + G_{amp}(K_1E_0 + K_0) + O_{amp}$$

where G_{amp} is the amplifier gain, O_{amp} is the amplifier offset, G_{acc} is the accelerator gain, E_0 is the energy offset, and K_1 and K_0 are angle dependent constants. At 21.965°, they are equal to

$$K_1 = 1.006 \pm 8.1 \times 10^{-5},$$

and

$$K_0 = -10.48 \pm 0.024.$$

One can perform a linear fit of the centroid to the Minitandem DVM setting, given the data from the energy calibration. This yields

$$C = m_1 V_{DVM} + m_0$$

where $m_1 = 124.86 \pm 0.61$ and $m_0 = 91.53 \pm 5.32$. Equating the coefficients of V_{DVM} and using $G_{acc} = 23.87$, determined in the accelerator calibration procedure, one obtains

$$G_{amp} = 5.202 \pm 0.025$$

as the amplifier gain.

Given the amplifier gain, the energy difference between any two peaks can be determined, although the absolute energy of either peak cannot. In any case, the angular distribution of kinematic peaks for any one constituent is not a sensitive measure of the reaction energy. However, the angular distribution of the difference between the p-^{12}C and p–d peaks is not only sensitive to the absolute energy, but is also independent of the amplifier offset. A number of runs from the p–d data set were selected for this determination. The selection criteria were that the proton-carbon and proton–deuteron centroids be well-determined and that the proton–carbon peaks in the monitor detectors did not exhibit any

unusual shifts. This latter criterion was the more restrictive. The data used in the absolute calibration are shown in Table 4.3.

Table 4.3: Data used in absolute energy calibration

Run #	$\theta_{nominal}$ [deg]	$^{12}C(p,p)^{12}C$ centroid [channel number]	$^{2}H(p,p)^{2}H$ centroid [channel number]
1127	24.359	1328.79 ± 0.75	1209.87 ± 1.0
1126	24.359	1326.79 ± 0.75	1206.67 ± 1.0
1086	29.359	1316.87 ± 0.75	1147.49 ± 1.0
1088	29.359	1316.98 ± 0.75	1146.70 ± 1.0
1095	39.359	1289.95 ± 0.75	1002.74 ± 1.0
1096	44.359	1271.69 ± 0.75	922.012 ± 1.0
1097	44.359	1271.03 ± 0.75	921.097 ± 1.0

A Monte Carlo sampling routine was used to infer the energy on the basis of the centroid differences. The energy was allowed to vary uniformly over the range of incident energies 310 keV $\leq E_{inc} \leq$ 330 keV. The amplifier gain was permitted to vary uniformly over half the range of its total uncertainty. The target was assigned an equivalent carbon thickness of 14.2 $\mu g/cm^2$ on the basis of the FWHM of a representative peak, using the predicted value of the amplifier gain to determine the energy width. The stopping power of [And77] was used to determine the equivalent carbon thickness.

The sampling code was run three times, using different starting values and search ranges. The search ranges were also varied with respect to symmetry about any particular value, so as to exclude the possibility of merely sampling the width of the search range. The inferred values of the incident energy and amplifier gain for the three sampling runs are shown in Table 4.4.

Table 4.4: Results of the absolute energy calibration

E_{inc} [keV]	G_{amp} [channel/keV]	χ^2/d.o.f.	fractional uncertainty
318.06 ± 1.90	5.203 ± 0.016	0.363	0.351%
318.11 ± 1.67	5.202 ± 0.007	0.364	0.352%
318.11 ± 1.67	5.202 ± 0.007	0.364	0.352%

The uniformity of the results belies the fairly large uncertainties associated with the incident energy. In fact, this uncertainty is related to the width of the sampling range assigned to the amplifier gain. Since the inferred value of the amplifier gain is also very uniform, this implies that the uncertainty in the amplifier gain is overstated. This is undoubtedly in part a consequence of using a uniform distribution for the amplifier gain, when in fact, the distribution of uncertainties in this parameter is unknown.

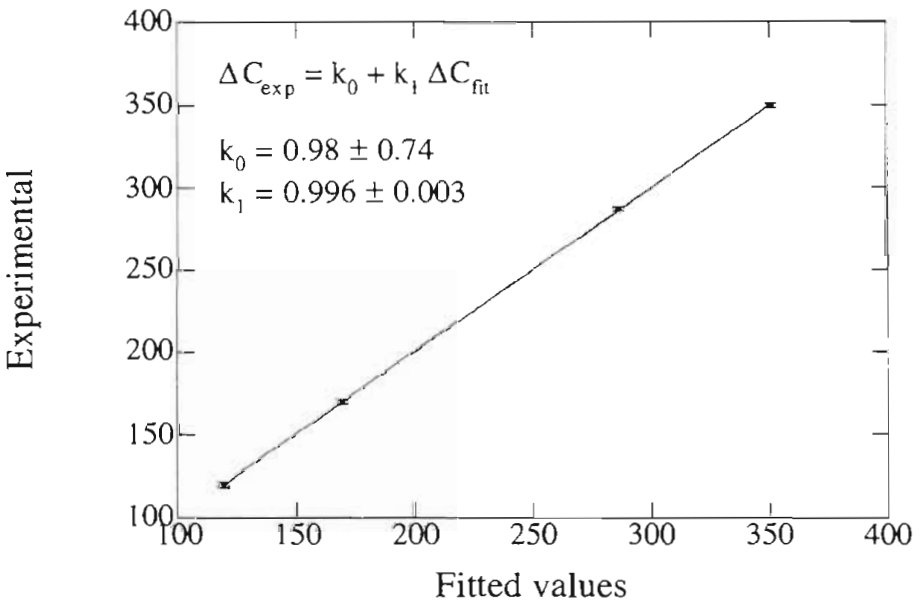

Figure 4.6 Comparison of experimental and fitted values for the centroid difference of the $^{12}C(p,p)^{12}C$ and $^{2}H(p,p)^{2}H$ peaks

Figure 4.6 shows the fit between the experimental centroid differences and the differences given the model parameters from sample number 3 of Table 4.4. The fit lies, in each case, within the experimental

uncertainties, which are of the order of 0.5% to 1.0% of the difference. The values

$$E_{inc} = 318.1 \pm 1.7 \text{ keV}$$

and

$$G_{amp} = 5.202 \pm 0.007$$

are taken to be the canonical incident energy and amplifier gain in what follows. Upon subtracting the assumed energy loss in the target, the mean proton interaction energy is

$$E_p = 314.9 \pm 1.7 \text{ keV}$$

4.4.1 Relative cross sections

Relative cross sections for the $^{12}C(p,p)^{12}C$, $^{2}H(p,p)^{2}H$ and $^{2}H(p,d)^{1}H$ reactions are given in the following series of tables. The peaks were extracted from the spectra using the MuMuRaMa spectral analysis code from each of the three detectors used in the experiment. Denoting the movable detector yield by R_1 and the monitor detector yields by R_{mon} and L_{mon} respectively, the relative cross sections were formed from the ratios

$$\sigma_{relative} = \frac{R_1}{R_{mon} + L_{mon}} .$$

The data from run 1130 has been excluded for the present, owing to a severe shift in the proton-carbon centroids in two of the detectors that has not yet been rectified. It was not possible to extract the $^{2}H(p,p)^{2}H$ yield from the 20° spectra, so only recoil data are given for this angle.

Table 4.5: Measured relative cross sections at $\theta_{nom} = 20°$

Run number	$^{12}C(p,p)^{12}C$	$^{2}H(p,p)^{2}H$	$^{2}H(p,d)^{1}H$
1081			0.213 ± 0.003
1083			0.239 ± 0.016
1084			0.211 ± 0.015
1085			0.214 ± 0.017
combined			$\mathbf{0.214 \pm 0.003}$

Table 4.6: Measured relative cross sections at $\theta_{nom} = 25°$

Run number	$^{12}C(p,p)^{12}C$	$^{2}H(p,p)^{2}H$	$^{2}H(p,d)^{1}H$
1127	1.870 ± 0.004	1.602 ± 0.048	0.234 ± 0.012
1126	1.842 ± 0.004	1.610 ± 0.041	0.229 ± 0.009
1123	1.869 ± 0.004	1.592 ± 0.041	0.243 ± 0.010
combined	$\mathbf{1.860 \pm 0.002}$	$\mathbf{1.601 \pm 0.025}$	$\mathbf{0.235 \pm 0.006}$

Table 4.7: Measured relative cross sections at $\theta_{nom} = 30°$

Run number	$^{12}C(p,p)^{12}C$	$^{2}H(p,p)^{2}H$	$^{2}H(p,d)^{1}H$
1086	0.9042 ± 0.0026	0.8228 ± 0.0254	0.237 ± 0.010
1088	0.9081 ± 0.0027	0.8183 ± 0.0236	0.203 ± 0.007
1089	0.9037 ± 0.0025	0.8626 ± 0.0265	0.222 ± 0.010
1090	0.8999 ± 0.0025	0.8888 ± 0.0264	0.218 ± 0.009
combined	$\mathbf{0.9038 \pm 0.0013}$	$\mathbf{0.8459 \pm 0.0127}$	$\mathbf{0.217 \pm 0.004}$

Table 4.8: Measured relative cross sections at $\theta_{nom} = 40°$

Run number	$^{12}C(p,p)^{12}C$	$^{2}H(p,p)^{2}H$	$^{2}H(p,d)^{1}H$
1092	0.2937 ± 0.0011	0.3306 ± 0.0118	0.227 ± 0.016

1094	0.2942 ± 0.0008	0.3550 ± 0.0108	0.220 ± 0.006
1095	0.2926 ± 0.0008	0.3589 ± 0.0127	0.216 ± 0.009
1093	0.2935 ± 0.0009	0.3550 ± 0.0127	0.218 ± 0.009
combined	**0.2935 ± 0.0004**	**0.3496 ± 0.0060**	**0.219 ± 0.004**

Table 4.9: Measured relative cross sections at $\theta_{nom} = 45°$

Run number	$^{12}C(p,p)^{12}C$	$^{2}H(p,p)^{2}H$	$^{2}H(p,d)^{1}H$
1096	0.1870 ± 0.0008	0.2312 ± 0.0087	0.211 ± 0.008
1097	0.1854 ± 0.0066	0.2595 ± 0.0100	0.228 ± 0.001
1098	0.1872 ± 0.0001	0.2404 ± 0.0010	0.239 ± 0.010
1101	0.1878 ± 0.0007	0.2458 ± 0.0108	0.226 ± 0.010
combined	**0.1872 ± 0.0001**	**0.2405 ± 0.0010**	**0.228 ± 0.001**

Table 4.10: Measured relative cross sections at $\theta_{nom} = 50°$

Run number	$^{12}C(p,p)^{12}C$	$^{2}H(p,p)^{2}H$	$^{2}H(p,d)^{1}H$
1103	0.1260 ± 0.0007	0.1836 ± 0.0090	0.235 ± 0.012
1105	0.1260 ± 0.0006	0.1882 ± 0.0092	0.234 ± 0.011
1107	0.1256 ± 0.0004	0.1886 ± 0.0063	0.243 ± 0.007
1110	0.1258 ± 0.0005	0.1994 ± 0.0065	0.257 ± 0.009
1114	0.1245 ± 0.0005	0.1957 ± 0.0069	0.244 ± 0.009
combined	**0.1255 ± 0.0002**	**0.1922 ± 0.0033**	**0.244 ± 0.004**

It was found that the global angular offset of –0.641° determined by the zero–crossing procedure outlined in section 4.2.1 was inconsistent with the offset determined by comparing the measured $^{12}C(p,p)^{12}C$ angular distributions with calculation. This may have been because the zero-crossing data were measured at very forward angles, where it is known that there are difficulties with the proper determination of the dead-time correction factor. In order to rectify this problem, the offset

was re-calculated by fixing the energy tightly about E_p = 314.9 keV, and simultaneously fitting the angle offset and the normalization constant with a Monte Carlo sampling code. The parameters were found to be:

$$E_p = 314.89 \pm 0.28 \text{ keV}$$

$$C_{norm} = (8.37167 \pm 0.01563) \times 10^{-6}$$

$$\delta\theta = -0.225° \pm 0.010°.$$

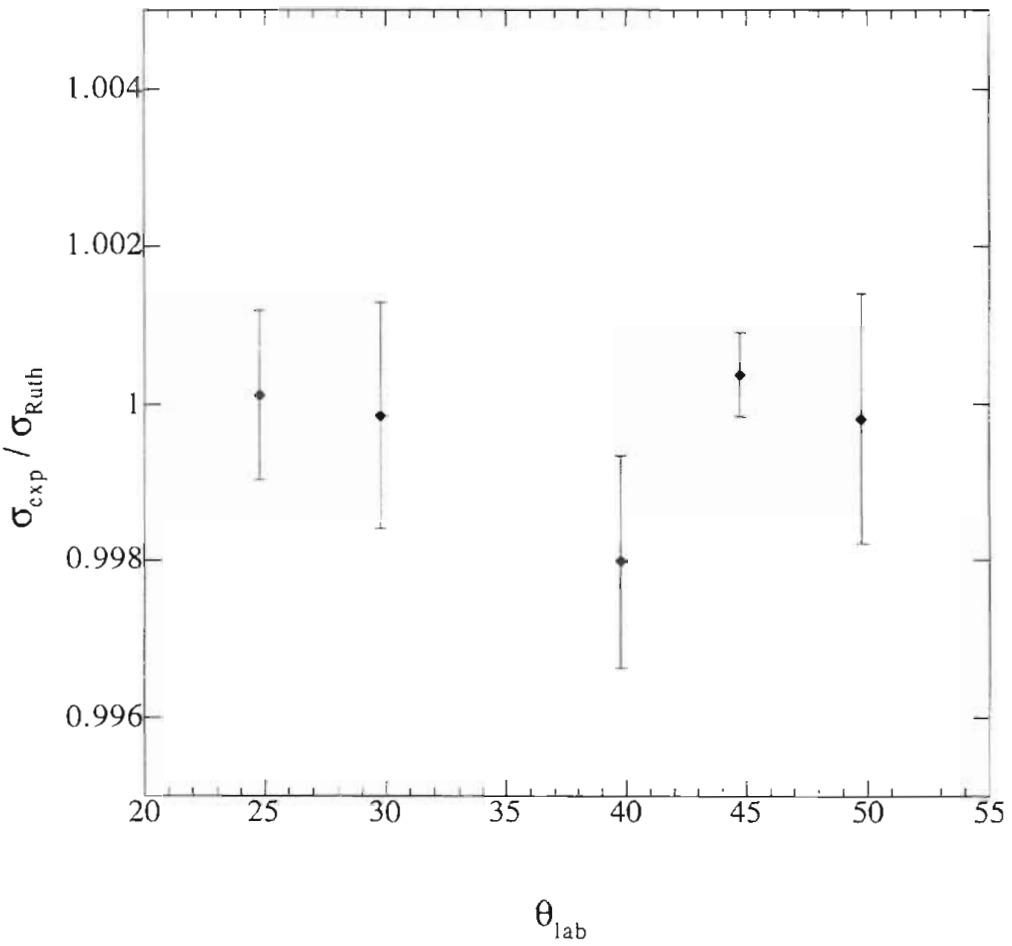

Figure 4.7 Ratio of experimental to calculated $^{12}C(p,p)^{12}C$ cross section using parameters determined from Monte Carlo angle-offset fitting procedure

The χ^2 uncertainty of the fit was 0.543 and the rms deviation was 0.057%. Figure 4.7 shows the ratio of experimental to Rutherford cross section obtained with these parameters. It should be noted that the angle offset is fairly well determined by this procedure. Since the derivative of the cross section with respect to angle is strongly dependent on the angle, it is not possible to directly compensate changes in the angle offset by changes in the global normalization.

Adopting $\delta\theta = -0.225°$ as the offset value for the angular distributions, center-of-mass angular distributions were obtained for proton-deuteron scattering. These are listed in Table 4.11.

Table 4.11: Center-of-mass p–d relative cross sections

θ_{Lab} [deg]	$\theta_{C.M.}$ [deg]	$\sigma(\theta)$ [arb units]
24.78	36.88	0.7634 ± 0.0120
29.78	44.16	0.4164 ± 0.0063
39.78	58.44	0.1867 ± 0.0032
44.78	65.41	0.1350 ± 0.0006
49.78	72.23	0.1142 ± 0.0020
55.96	80.45	0.0945 ± 0.0015
63.78	90.45	0.0803 ± 0.0004
72.03	100.45	0.0712 ± 0.0013
90.43	120.45	0.0625 ± 0.0012
101.04	130.45	0.0647 ± 0.0017
113.04	140.45	0.0569 ± 0.0008

Figure 4.8 shows the ratios of these angular distributions to the 314.9 keV p–d cross sections calculated using the S-wave parameters of [Hut83b] and [Che89]. All other parameters are those of [Hut83b]. It is fairly clear that the datum at $\theta_{lab} = 44.78°$ is anomalous. The points $\theta_{lab} = 101.04°$ and 113.04° might also be flawed. No explanation has yet been found for these apparent excursions. It cannot be simply a case of the angle being set incorrectly, as the p–^{12}C data agree well with the

rectified angles. Nor would the problem seem to lie with the dead-time corrections, since, at least for the data at 44.78° and 101.04°, their "partner points" appearing in the same spectra, the data at 63.78° and 24.78°, respectively, do not appear to be incorrect.

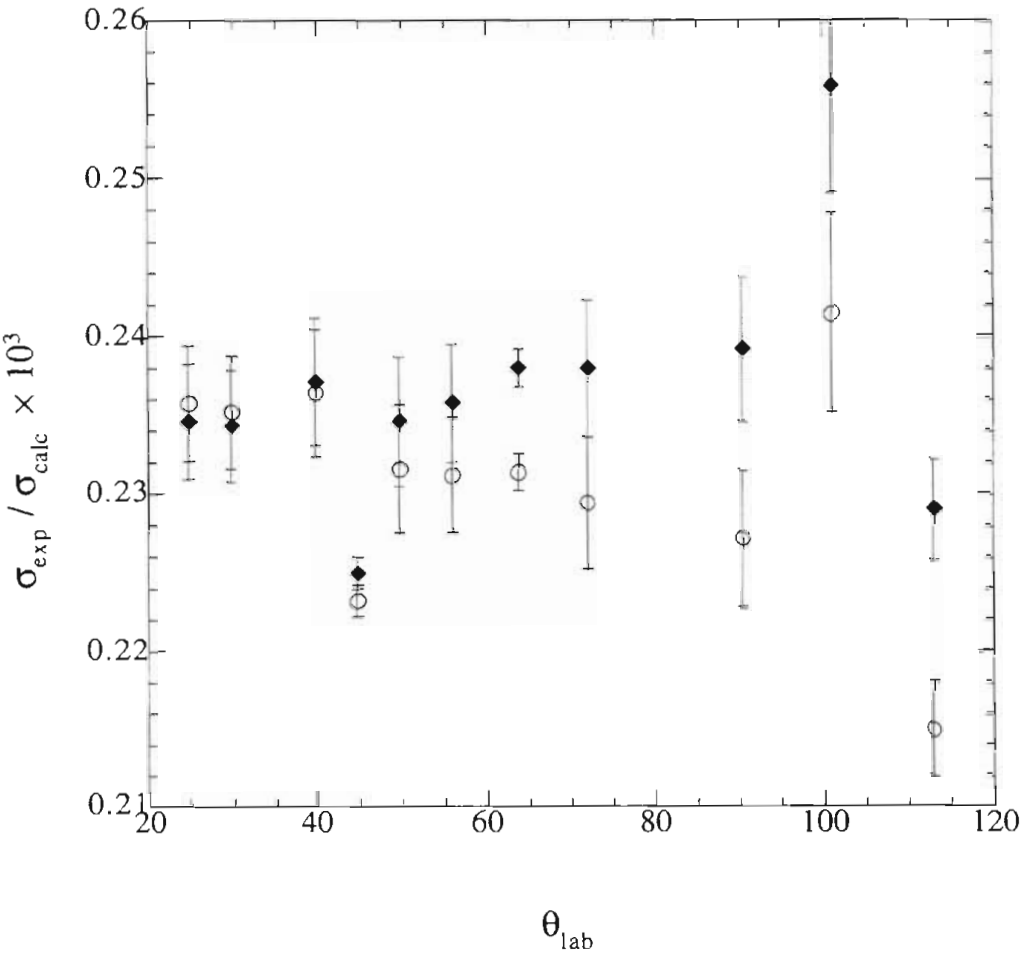

Figure 4.8 Ratio of experimental to calculated p–d cross section. The scale is arbitrary. The ratios calculated with the S-wave parameters of [Hut83b] are represented by diamonds. The circles represent the calculations using the S-wave parameters of [Che89]. The data are unnormalized.

Table 4.12: Normalized center-of-mass p–d cross sections

θ_{Lab} [deg]	$\theta_{C.M.}$ [deg]	$\sigma(\theta)$ [mb/sr]
24.78	36.88	3238 ± 50

29.78	44.16	1766 ± 27
39.78	58.44	792.0 ± 14
44.78	65.41	572.7 ± 3
49.78	72.23	484.4 ± 8.5
55.96	80.45	401 ± 6.4
63.78	90.45	341 ± 2
72.03	100.45	302 ± 5.5
90.43	120.45	265 ± 5.1
101.04	130.45	274 ± 7.2
113.04	140.45	241 ± 3

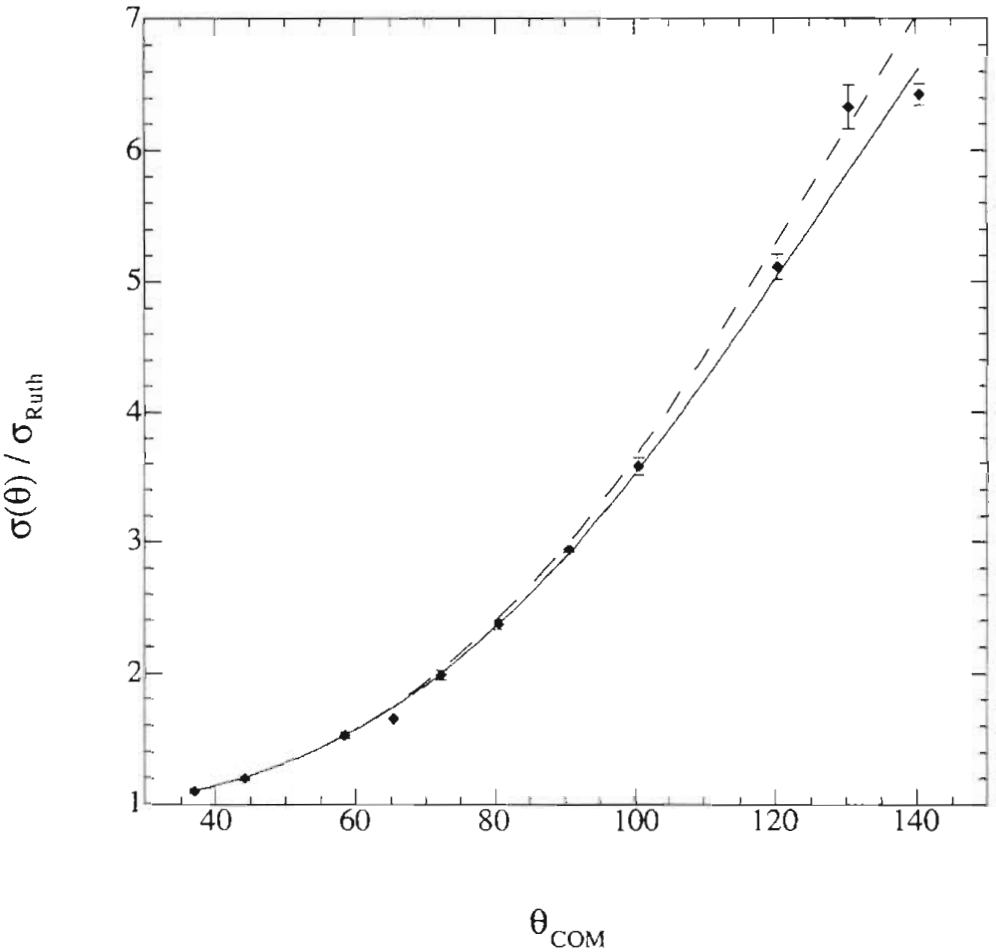

Figure 4.9 Center-of-mass proton-deuteron differential cross sections, divided by the p–d Rutherford cross-section. The diamonds are the TUNL data of this work.

The data were normalized at 29.78° and 39.78°, using the average normalization constants obtained from the two sets of S-wave parameters, so that the normalization constant $N_0 = 4242$. The normalized data are given in Table 4.12.

Figure 4.9 shows the measured experimental cross section plotted with two sets of calculated p–d cross sections. The solid line was calculated using the effective parameters of [Hut83b], whereas the dashed line was calculated with the S-wave effective range parameters of [Hut83b] replaced with those of [Che89]. The latter calculation predicts a pole in the doublet S-wave effective range function.

4.5.1 Discussion

Recent sophisticated calculations of the p–d cross section and spin observables have been performed by the theory group at Pisa at a number of energies [Kie94, Kie95a, Kie95b]. The calculations are performed by solving the Schrödinger equation using a variational method in which the wavefunction is expanded in a basis of correlated hyperspherical harmonics.

Figure 4.10 shows the ratio of the angular distribution data to the cross sections calculated using effective range parameters extracted from the phases calculated by the Pisa group. Also shown are the ratios of Figure 4.8. The possibly anomalous data at $\theta_{lab} = 44.78°$, 101.05° and 113.04° have been suppressed to clarify the comparison.

The Pisa calculations, like those of [Che89]. predict a very small value of the doublet S-wave scattering length, ($^2a_0 \approx -0.02$ fm) and a pole in the effective range function. At 314.9 keV, the S-wave phases are very close to those predicted by [Che89]. The S, P and D phases at 314.9 keV predicted on the basis of effective range expansions of the phases calculated in [Hut83b], [Kie94, Kie95a, Kie95b] and [Che89] are given in Table 4.13.

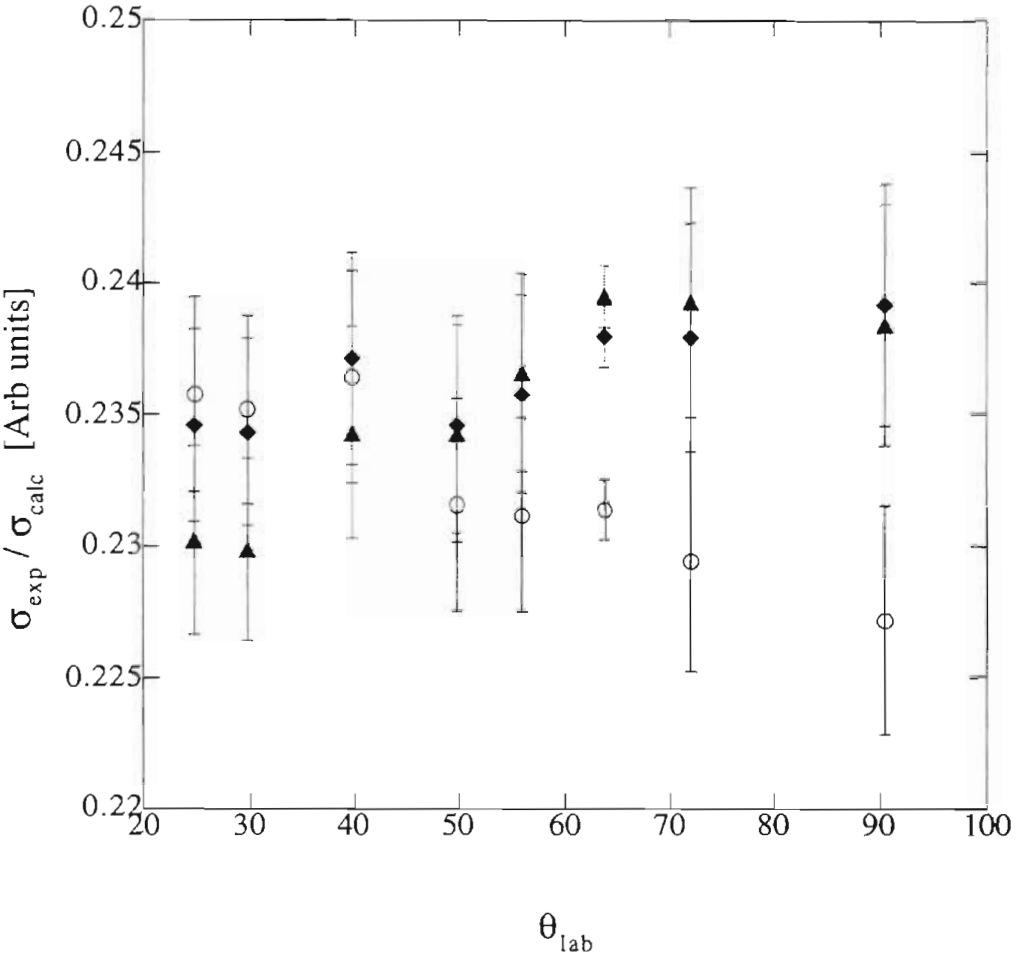

Figure 4.10 Ratio of the p–d angular distribution to calculated values of the differential cross section at E_p = 314.9 keV. The diamonds represent ratios calculated using the effective range parameters of [Hut83b]. The circles were calculated using the effective range parameters of [Hut83b], but with the S-wave phases replaced by those of [Che89]. The ratios calculated using effective ranges extracted from the phases of [Kie94, Kie95a, Kie95b] are denoted by triangles. The data are unnormalized.

Table 4.13 Theoretical and phenomenological phase shifts at E_p = 314.9 keV

	[Hut83b] (deg)	[Kie94, Kie95a, Kie95b] (deg)	[Che89] (deg)
$^2S_{1/2}$	–5.767	–1.818	–2.123
$^4S_{3/2}$	–14.293	–16.042	–16.264

$^4P_{5/2}$	2.205	1.877	—
$^4P_{3/2}$	2.210	2.009	—
$^4P_{1/2}$	2.142	1.735	—
$^2P_{3/2}$	–0.367	–0.703	—
$^2P_{1/2}$	–0.371	–0.707	—
$^4D_{5/2}$	–0.041	–0.071	—
$^4D_{3/2}$	–0.041	–0.066	—
$^4D_{1/2}$	–0.041	–0.059	—
$^2D_{5/2}$	0.549	0.034	—
$^2D_{3/2}$	0.549	0.034	—

The P-wave and D-wave quartet phases extracted from the Pisa calculations and the Giessen phase shift analysis are in fairly good agreement, although the quartet S-wave phases are quite different. The doublet phases predicted by the Pisa group are all in disagreement with the phenomenological phases. The S-wave phases predicted by [Che89] are consistent with those extracted from the calculations of [Kie94, Kie95a, Kie95b].

Figure 4.11 shows the ratio of experimental angular distribution to calculated differential cross sections for three different cases. The cross section using the Pisa phases are shown as triangles. Diamonds represent the cross section calculated using the S-wave phases of [Hut83b]: All other phases are the same as the Pisa predictions. Finally, the ratio was calculated using all of the Pisa phases except for the doublet S-wave phase shift, which was given by the Giessen phenomenological parameters. This ratio is denoted by circles.

As expected, the back-angle data are especially sensitive to the S-wave phase shifts. An intriguing interpretation of Figure 4.11 is that the measured angular distribution can be fairly well described with the $^2S_{1/2}$ phase shift of [Hut83b], all other phases being taken from the calculations of [Kie94, Kie95a, Kie95b]. If a complete phase shift

analysis bears out this conclusion, this would be quite an interesting result. The dependence of the cross section on the P-waves and D-waves is fairly complicated and small, being roughly 2–3%.

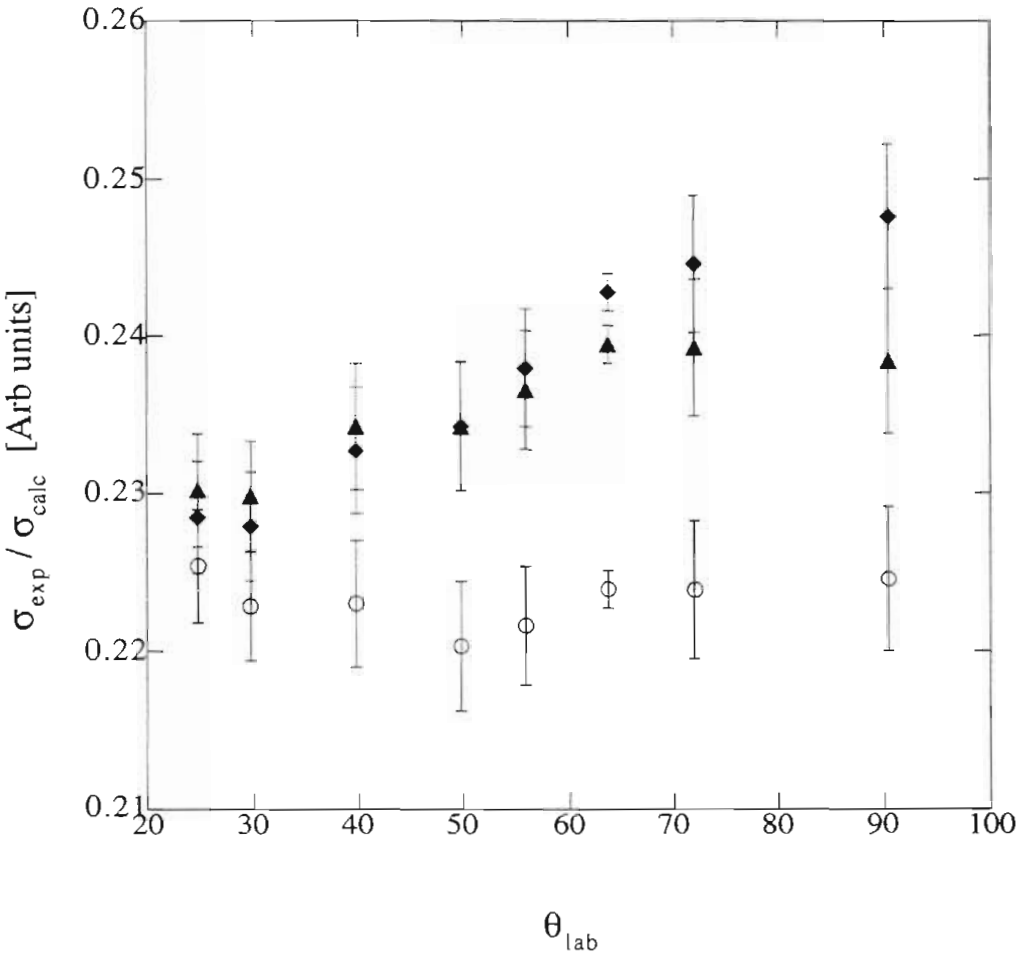

Figure 4.11 Ratio of p-d angular distributions to calculated cross sections at E_p = 314.9 keV using three different combinations of S-wave phase shifts. The plotting symbols are explained in the text.

Figure 4.12 exhibits the sensitivity of the differential cross section to P and D waves. The ratio depicted by triangles is the same as that of figure 4.11. Diamonds and circles represent the ratios calculated using the Pisa phase shifts at E_p = 314.9 keV, with the P-wave and D-wave phase shifts of [Hut83b], respectively, substituted for their Pisa analogs.

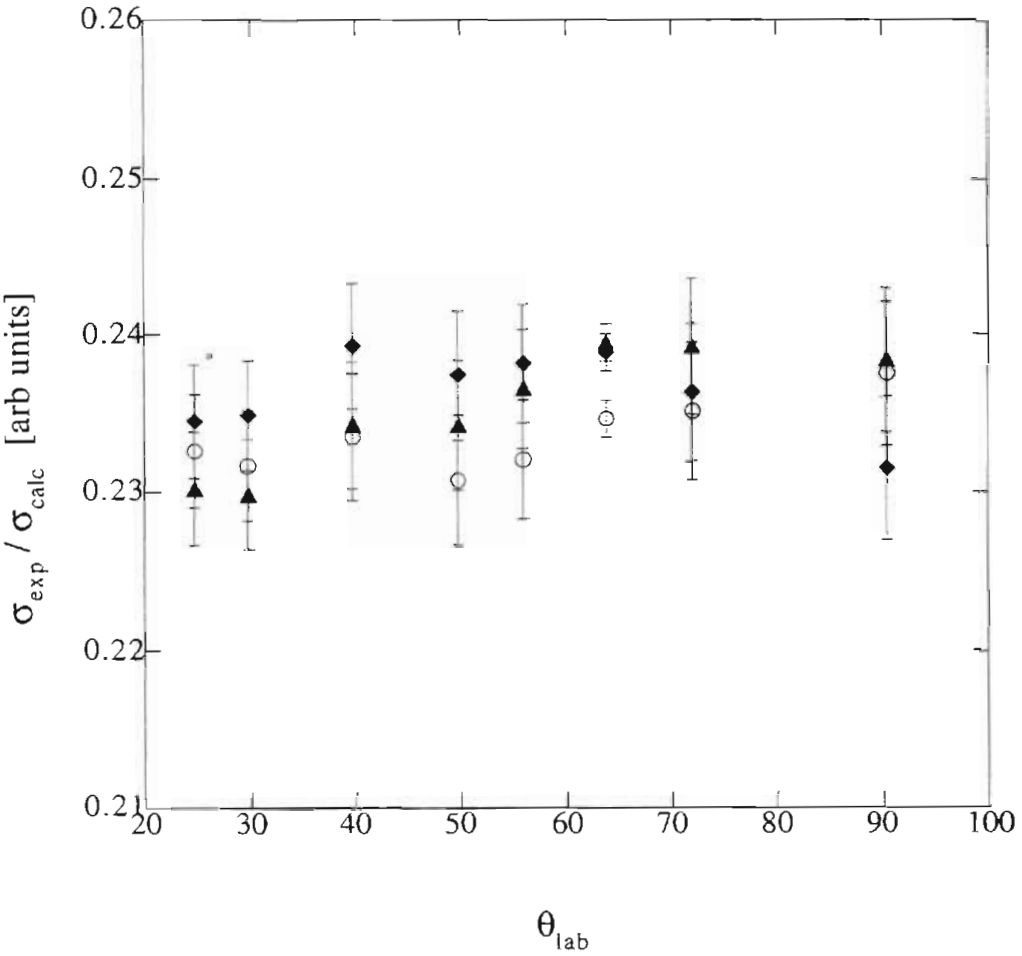

Figure 4.12 Sensitivity of experimental to calculated p–d angular distribution ratios to P-wave and D-wave phases at E_p = 314.9 keV.

4.5.2 Other measurements

Relative cross sections have already been measured at $E_p \approx 250$ keV. Analysis of this data should be completed shortly. Given the strong dependence of the shape of the cross section on the S-waves, this data, in conjunction with the measurements at 314.9 keV, ought to be sufficient to reach fairly strong conclusions regarding the S-wave parameters, when incorporated into an energy dependent phase shift analysis. But the low-energy data set for the p–d elastic scattering reaction is by no means complete. It would be useful, for instance, to obtain an absolute determination of the differential cross section at one or two angles between θ_{lab} = 25°–40° as near as possible to 314.9 keV

(reaction energy) and at the energy of the second data set. This determination would be most valuable if the accuracy were better than 1%. If the absolute accuracy were not better than 2%, it might not be worth measuring.

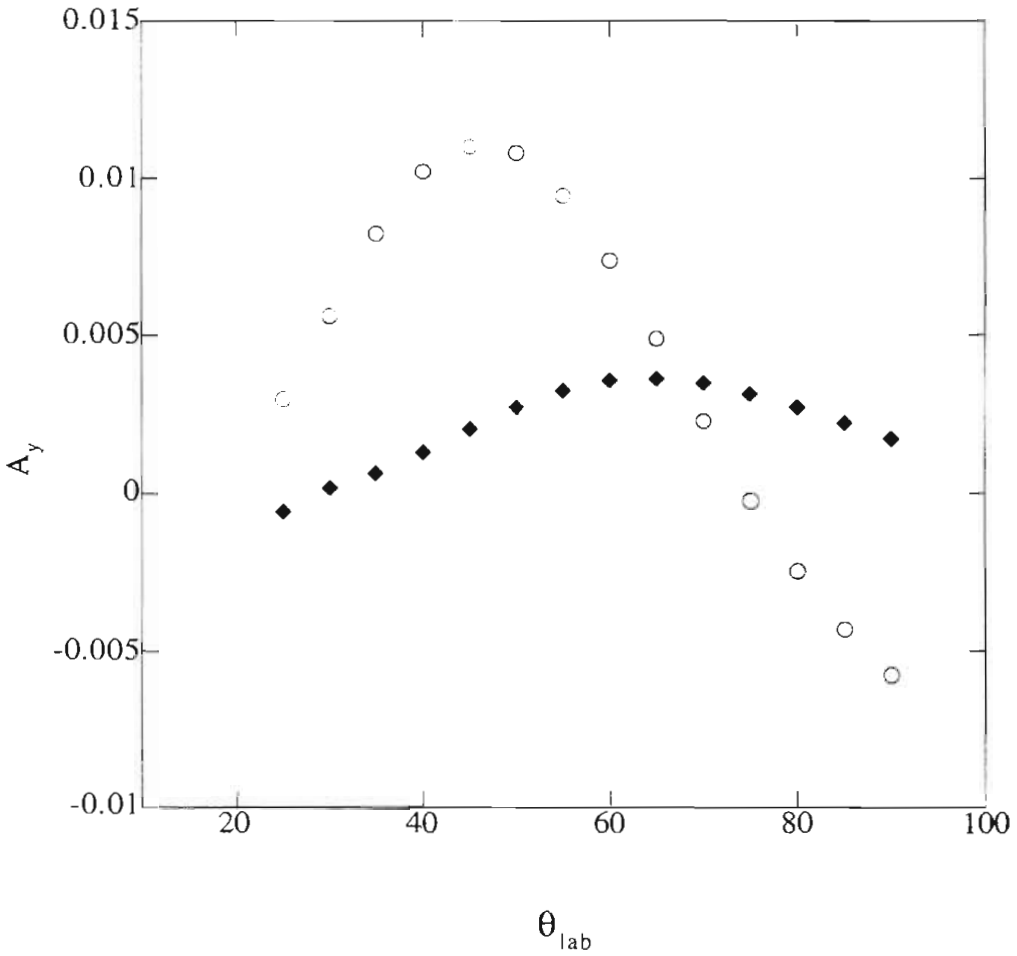

Figure 4.13 Predicted proton analyzing power at E_p = 600 keV using phase shifts extracted from the calculations of [Kie94, Kie95a, Kie95b] and with the P-wave phase shifts of Kievsky, et al. replaced by those of [Hut83b]. The former are plotted as diamonds, the latter as circles.

It has also been suggested that measurements of the proton analyzing power at low energy would be interesting. Figure 4.13 shows A_y at 600 keV calculated under two conditions; with the phases extracted from the calculations of [Kie94, Kie95a,Kie95b], and with the P-wave phase shifts of [Hut83b] replacing those of Kievsky, et al. Clearly, the

two predictions are quite distinct, although the analyzing powers themselves are quite small. Also, it must be recalled that the analyzing power is very sensitive to the P-wave spin-mixing parameter $\varepsilon^{(-)}$. For this reason, it is very important to incorporate the correct threshold behavior for the spin-mixing angles into the phase shift parameterization. Otherwise, the phase shifts may be forced to take on incorrect values in order to compensate.

4.5.3 Phase shift analysis

A Monte Carlo sampling-based inference code has been written to perform the energy dependent phase shift analysis, using the effective range theory. Since the influence of the higher partial waves is relatively small, it seems reasonable, at least in the initial phase of the calculation, to restrict the search of parameter space to those regions that have the greatest theoretical support. For the doublet S-wave effective range parameters, this is problematic. The regions of parameter space corresponding to the phenomenological and theoretical predictions for this phase shift are disjunct. Furthermore, very small changes in the pole parameter cause enormous changes in the effective range function. These changes can be compensated in large measure by correspondingly large changes in the effective range parameter.

It is a very tricky matter to perform this analysis in a numerically stable manner that nonetheless fairly evaluates all physically plausible combinations of parameters. It is anticipated that the phase shift analysis will be completed soon. Prior to that time, it would be premature to draw strong specific conclusions, but one can make some general remarks on the basis of a consideration of Figures 4.10—4.12.

The data at 314.9 keV are about equally consistent with the calculations of the Pisa group and the phenomenological predictions of [Hut83b], but are not overwhelmingly consistent with either. The data seem to rule out the adoption of the Giessen S-wave phase shifts in combination with the higher partial wave predictions of [Kie94, Kie95a, Kie95b]. However, the data are completely consistent with the particular

set of the doublet S-wave phase shift of [Hut83b] and all other phases taken from Kievsky, et al.

It is very difficult to justify, on theoretical grounds, the phenomenological predictions for the quartet S-wave and it would be gratifying if it were the case that the phenomenological prediction is incorrect. It might be a good exercise to fix all of the quartet parameters at their theoretical values and examine the range of possible values for the doublet phases. The chances are good that the true parameterization is a subset of this group of values. The addition of the lower energy data set will naturally permit a further narrowing of the possibilities.

I think that the sampling-based approach that has been taken with regard to the phase shift analysis will yield some interesting results. The output of this type of analysis, which has the form of marginal posterior distribution functions, can provide tremendous insight into the nature of the parameter space and hence, into the physical system itself. This sort of insight simply cannot be acquired from a set of "most likely" predictions. Thus, the analysis of this data will unquestionably leave us much better informed as to the nature of the p–d system.

APPENDIX A: FORMAL SCATTERING THEORY

The aim of this appendix is to elucidate certain issues from the theory of two and three-particle scattering which are relevant to the p–d elastic scattering reaction below the deuteron breakup threshold. The formalism developed here is, for the most part, sufficiently general so as to accommodate a description of multichannel systems, with the single-channel theory taken as a special case. The treatment is neither comprehensive nor exceptionally rigorous. All properties of the short-range nuclear interaction that are required to hold so that the system constitutes a "scattering system", as defined in [New82] are assumed to hold. The quantum scattering theory presented here is a personal synthesis of concepts developed and expounded in the following references: "Theory of Time-dependent Scattering for Multichannel Processes" by H. Ekstein [Eks56], and "Scattering Theory of Waves and Particles" by R. G. Newton [New82]. It is assumed throughout that the non-relativistic approximation is valid.

A.1 Formal quantum scattering theory

Quantum mechanical scattering theory represents a means of re-casting the dynamics contained in the Schrödinger equation into the form of an integral equation which, for a large class of interaction potentials, automatically satisfies appropriate boundary conditions. Furthermore, fundamental assumptions like causality and unitarity that organically provide strong constraints on the scattering amplitudes and observables are embedded within its structure. The formal problem of comparing the results of a scattering experiment to theory is resolved as follows:

Space is divided into two regions. In general, the boundary between these regions is diffuse, but the exact location of the boundary is irrelevant. The innermost region—the interaction region—is defined by the radius of the short-range nuclear interaction. The wavefunction in this region, $\psi'(r, t)$, satisfies the Schrödinger equation

$$\left(i\hbar\frac{\partial}{\partial t} - H\right)\psi'(r, t) = 0$$

where the full interaction Hamiltonian, $H = V + H_0$, is the sum of a short-range interaction V that falls off rapidly outside the interaction region and a long-range part H_0 that is assumed to permeate all of space.

Assuming that the interaction Hamiltonian is independent of the time, the retarded (+) and advanced (–) Green's function solutions of the interaction region Schrödinger equation can be written explicitly as

$$\mathcal{G}^+(t) = \begin{cases} -i \exp\left\{\frac{-iHt}{\hbar}\right\} & t > 0 \\ 0 & t < 0 \end{cases}$$

and

$$\mathcal{G}^-(t) = \begin{cases} 0 & t > 0 \\ i \exp\left\{\frac{-iHt}{\hbar}\right\} & t < 0 \end{cases}$$

so that $\psi'(r, t)$ evolves in time according to

$$\psi'(r, t) = i\mathcal{G}^+(t - t')\,\psi'(r, t') \qquad \text{for } t > t'$$

and

$$\psi'(r, t) = -i\mathcal{G}^-(t - t')\,\psi'(r, t') \qquad \text{for } t < t'.$$

The wavefunction of the scattering system in the asymptotic region, $\psi_0(r, t)$, both prior and subsequent to the scattering event, is taken to be an appropriate superposition of eigenstates $\phi(r, t)$ of the asymptotic Hamiltonian H_0:

$$\psi_0(r, t) = \sum_\alpha a_\alpha\,\phi_\alpha(r, t).$$

One can implicitly define an interaction representation by expressing the eigenstates $\phi_\alpha(r, t)$ in terms of Green's function operators, $G_0^{\pm}(t)$ which solve the equation

$$\left(i\hbar\frac{\partial}{\partial t} - H_0\right)G_0^{\pm}(t) = \hbar\delta(t).$$

They are

$$G_0^{+}(t) = \begin{cases} -i\exp\left\{\frac{-iH_0t}{\hbar}\right\} & t > 0 \\ 0 & t < 0 \end{cases}$$

and

$$G_0^{-}(t) = \begin{cases} 0 & t > 0 \\ i\exp\left\{\frac{-iH_0t}{\hbar}\right\} & t < 0 \end{cases} .$$

Then the basis states, $\phi_\alpha(r, t)$ can be written as

$$\phi_\alpha(r, t) = \begin{cases} iG_0^{+}(t - t')\,\phi_\alpha(r, t') & t > t' \\ -iG_0^{-}(t - t')\,\phi_\alpha(r, t') & t < t' \end{cases}$$

and a particular choice of the interaction representation can be made by choosing t'. Since the set $\phi_\alpha(r)$ is assumed to be complete, every wavepacket that is a solution of the Schrödinger equation in the asymptotic region, for any time t, can be written as a superposition of the form

$$\psi_0(r, t) = \sum_\alpha \pm i\, a_\alpha G_0^{\pm}(t)\,\phi_\alpha(r).$$

Two such solutions are of particular interest: the solution that in the remote past equaled the wavefunction that solves the interaction region Schrödinger equation, and the solution that will be equal to the

interaction region wavefunction in the remote future. More precisely, these solutions must converge in the norm (converge strongly) to solutions of the interaction region Schrödinger equation in the limits as the time t goes to $\pm\infty$. Hence, the "in" and "out" states are related to the interaction region solution by

$$\psi_{in}(r, t) = \lim_{t' \to -\infty} iG_0^+(t - t')\, \psi'(r, t')$$

and

$$\psi_{out}(r, t) = \lim_{t' \to +\infty} -iG_0^-(t - t')\, \psi'(r, t')$$

and also

$$\psi'(r, t) = \lim_{t' \to -\infty} i\mathcal{G}^+(t - t')\, \psi_{in}(r, t')$$

$$= \lim_{t' \to +\infty} -i\mathcal{G}^-(t - t')\, \psi_{out}(r, t') .$$

The boundary conditions expressed in the last two equations are as follows: In the infinite past, the scattering wavefunction was equal to a particular solution of the asymptotic region Schrödinger equation. In the infinite future, it will be equal to another, generally different, particular solution of the asymptotic region Schrödinger equation. In practical experimental situations, the quantum labels of the "in" state are fixed by the experimenter who prepares the incident beam in a given manner. Various quantum labels, discrete and continuous, of the "out" state are measured by the detection apparatus. All of the information that can be inferred about the dynamics in the interaction region on the basis of a scattering experiment is contained in the mapping which transforms the "in" state to the "out" state at any given time. This mapping, which in the single channel case is a quantum operator, is the $\mathcal{S}$-matrix.

A.2 The Scattering Matrix

The relation between the "in" and "out" states for different times is

$$\psi_{out}(r, t) = \lim_{t' \to +\infty} \lim_{t'' \to -\infty} G_0^-(t - t')\, \mathcal{G}^+(t' - t'')\, \psi_{in}(r, t'')$$

so that the equal time relationship is

$$\psi_{out}(r, t) = \lim_{t' \to +\infty} \lim_{t'' \to -\infty} -iG_0^-(t - t')\, \mathcal{G}^+(t' - t'')G_0^-(t'' - t)\, \psi_{in}(r, t)\ .$$

This can be used to define the scattering operator $\mathcal{S}$ by means of the relation

$$\psi_{out}(r, t) \equiv \mathcal{S}\psi_{in}(r, t).$$

The scattering operator $\mathcal{S}$ maps the superposition coefficients of $\psi_{in}(r, t)$ onto those of $\psi_{out}(r, t)$, for arbitrary times t. In particular, for $t = 0$, if

$$\psi_{in}(r, 0) = \sum_{\alpha} \pm i\, a_\alpha^{(in)} \phi_\alpha(r)$$

and

$$\psi_{out}(r, 0) = \sum_{\beta} \pm i\, a_\beta^{(out)} \phi_\beta(r)\ ,$$

the orthonormality of the eigenstates of the asymptotic Hamiltonian implies that

$$a_\beta^{(out)} = \sum_{\alpha} \mathcal{S}_{\beta\alpha}\, a_\alpha^{(in)}.$$

But it is also the case that

$$a_\beta^{(out)} = \sum_{k} \int dr\, \phi_\beta^*(r) \lim_{t' \to +\infty} \lim_{t'' \to -\infty} -iG_0^-(-t')\mathcal{G}^+(t' - t'')G_0^+(t'')a_\alpha^{(in)}\phi_\alpha(r),$$

so that the representation of $\mathcal{S}$ in the basis of eigenstates of the asymptotic Hamiltonian is

$$S_{\beta\alpha} = -i \lim_{\substack{t' \to +\infty \\ t'' \to -\infty}} \int dr\, \phi_\beta{}^*(r)\, G_0{}^-(-t')\, \mathcal{G}^+(t' - t'')\, G_0{}^-(t'')\, \phi_\alpha(r)\ .$$

Using the fact that $\left(G_0{}^{\pm}(t)\right)^\dagger = G_0{}^{\mp}(-t)$ and $\left(\mathcal{G}^{\pm}(t)\right)^\dagger = \mathcal{G}^{\mp}(-t)$, the S-matrix can be written as

$$S_{jk} = \lim_{\substack{t' \to +\infty \\ t'' \to -\infty}} \left\langle \mathcal{G}^-(-t')\, G_0{}^+(t')\phi_\beta(r),\, \mathcal{G}^+(-t'')\, G_0{}^-(t'')\, \phi_\alpha(r) \right\rangle,$$

or alternately as

$$S_{\beta\alpha} = \lim_{\substack{t' \to +\infty \\ t'' \to -\infty}} \left\langle \exp\left\{\frac{i}{\hbar}(H - H_0)t'\right\}\phi_\beta(r),\, \exp\left\{\frac{i}{\hbar}(H - H_0)t''\right\}\phi_\alpha(r) \right\rangle\ . \qquad (A.1)$$

Using the definition of the Møller operators [New82],

$$\Omega^{(\pm)} \equiv \lim_{t \to \mp\infty} \exp\left\{\frac{i}{\hbar}(H - H_0)t\right\}$$

and their action on the in and out states;

$$\psi'^{(+)}_{\alpha}(r) = \Omega^{(+)}\psi_{in}(r)$$

and

$$\psi'^{(-)}_{\beta}(r) = \Omega^{(-)}\psi_{out}(r),$$

one also has

$$S_{\beta\alpha} = \left\langle \Omega^{(-)}\psi_{out}(r),\, \Omega^{(+)}\psi_{in}(r) \right\rangle = \left\langle \psi'^{(-)}_{\beta}(r), \psi'^{(+)}_{\alpha}(r) \right\rangle \qquad (A.2)$$

where $\psi'^{(-)}_{\beta}(r)$ refers to the solution of the interaction region Schrödinger equation that will be equal to the asymptotic state $\psi_{out}(r)$ in the infinite future and $\psi'^{(+)}_{\alpha}(r)$ is that solution to the interaction region Schrödinger equation that was, in the infinite past, equal to the asymptotic state $\psi_{in}(r)$.

In operator form, $\mathcal{S} = \Omega^{(-)\dagger}\Omega^{(+)}$; it is sometimes defined by this equation. It has already been assumed that the interaction potential is time-independent. If one further assumes that the sets of basis states ψ_{in} and ψ_{out} are complete, then it is easy to show that

$$\psi_{in} = \Omega^{(+)\dagger}\Omega^{(-)}\psi_{out} = \mathcal{S}^{\dagger}\psi_{out} = \mathcal{S}^{\dagger}\mathcal{S}\psi_{in},$$

so that $\mathcal{S}$ is unitary. The time-independence of the potential and the completeness of the asymptotic states reflect the conservation of probability flux[29].

Since the operator $\mathcal{S}$ is independent of time, the $\mathcal{S}$-matrix in the time-independent theory can be formed by evaluating it according to equation (A.2) in a basis of time-independent states. Alternately, one can generate the $\mathcal{S}$-matrix from explicitly time-independent Møller operators. These latter are formed by taking the Fourier transform of the Møller operators, after multiplication by the convergence factor $\exp(-\varepsilon t)$. Using the mathematical identity,

$$\lim_{t \to \pm\infty} f(t) = \pm \lim_{\varepsilon \to +0} \varepsilon \int_0^{\pm\infty} \exp(\mp\varepsilon t) f(t)\, dt\,,$$

the Møller operators can be expressed as

---

29 Optical models of scattering systems may violate probability flux conservation and in this case, the non-completeness of the set of asymptotic states is related to the complex nature of the potential.

$$\Omega^{(\pm)} = \lim_{\varepsilon \to +0} \varepsilon \int_0^{+\infty} \exp(-\varepsilon t) \exp\{\mp \tfrac{i}{\hbar} (H - H_0)t\} \, dt$$

or

$$\Omega^{(\pm)} = \lim_{\varepsilon \to +0} \left[1 - (H - H_0 \mp i\varepsilon)^{-1}(H - H_0)\right]$$

In the time-dependent description, the quantum states characterizing the asymptotic and interaction states are wave-packets—superpositions of states of definite momentum—so that the expectation value of their displacement, $\langle r(t) \rangle$, propagates across the scattering region. In particular, these states are created at some finite time and also decay at some finite time. The states of definite momentum, which describe the wavefunctions in the time-independent or "steady-state" description, have an infinite extent in space and time, and for such states there is no physical meaning to the notion of the infinite past and infinite future, since the state of the system is identical for all eternity. Such a description is inherently acausal, and this lack of causality causes both formal and practical difficulties.

Causality can be re-introduced by forming "damped" wavefunctions that are generated by multiplying all time-dependent factors in the Fourier integrals by the convergence factor $\exp(\pm\varepsilon t)$, and subsequently taking the limit as ε goes to 0. Wavefunctions that propagate into the future from a given initial state must be damped in the future. These require a convergence factor of $\exp(-\varepsilon t)$ whose ε-limit is taken from above. Wavefunctions that propagate into the past from a given final state must be damped in the infinite past and thus require a convergence factor of $\exp(\varepsilon t)$ whose ε-limit is taken from below.

A practical description of scattering theory depends upon a steady-state representation in which the causality inherent in the time-dependent picture is preserved. Moreover, the use of dispersion relations and the description of the physical scattering process in terms of

the analytic properties of the solutions of the scattering equations in the complex momentum plane require that great care be taken in properly expressing causal boundary conditions in the time-independent description.

A.3 The Partial Wave Expansion

In general, the scattering matrix depends upon the momentum, the spin, the orbital angular momentum, the total angular momentum and the parity of the incident and final channels. Only the on-shell elements are relevant to elastic scattering in the single channel case. Since the nuclear Hamiltonian conserves parity and the total angular momentum is always conserved, it is sufficient to consider the on-shell sub-matrices $S^{j\pi}_{\ell's',\ell s}(k)$; labeled by the orbital angular momentum indices ℓ' and ℓ, the channel spin indices s′ and s, the total angular momentum j and the parity π. Assuming that the nuclear potential is time-reversal invariant and is Hermitian; e.g., time-symmetric and time-independent, and that no external fields are present, then the S-matrix is symmetric with respect to exchange of the quantum numbers of its basis states. Hence,

$$S^{j\pi}_{\ell's',\ell s}(k) = S^{j\pi}_{\ell s,\ell's'}(k) \ .$$

The basis states for representing the sub-matrix $S^{j\pi}_{\ell's',\ell s}(k)$ can be written

$$|Q\rangle = \sum_m |\ell,s,j,m\rangle|k\rangle,$$

where m is the projection of j onto some quantization axis. Since space is presumably isotropic, the elements of the S-matrix are independent of m.

This is a convenient basis in which to express theoretical parameters. However, it is not such a good basis in which to represent the experimental observations. The quantum states j, ℓ, and π are not observable, although they can sometimes be inferred. By contrast, since

the beam is typically prepared as a mixture of definite spin states, and detected as an expectation over some spin-dependent interaction[30], the $\mathcal{S}$-matrix should be expressed in a representation in which the quantum basis states depend upon the channel spin s, the channel spin projection ν, and the momentum unit vector **k**, but not on the unobservable labels j, ℓ, and π. This basis can be written schematically as $|\mathcal{Z}\rangle = |s,\nu\rangle|\mathbf{k}\rangle$.

According to the standard prescription, the relation between the $|\mathcal{Z}\rangle$ basis and the $|\mathcal{Q}\rangle$ basis is

$$\langle \mathcal{Z}' | \mathcal{S} | \mathcal{Z} \rangle = \sum_{\mathcal{Q}} \sum_{\mathcal{Q}} \langle \mathcal{Q} | \mathcal{S} | \mathcal{Q} \rangle \langle \mathcal{Z}' | \mathcal{Q} \rangle \langle \mathcal{Q} | \mathcal{Z} \rangle$$

so that $\langle \mathcal{Q} | \mathcal{Z} \rangle = \langle \ell,s,j,m | s,\nu,\mathbf{k} \rangle$ must first be determined.

The (ℓ,s,j,m) state can be expanded as

$$|\ell,s,j,m\rangle = \sum_{\mu,\nu} |s,\nu\rangle|\ell,\mu\rangle \Big[\langle \ell,\mu | \langle s,\nu | \Big] | \ell,s,j,m \rangle$$

$$= \sum_{\mu,\nu} |s,\nu\rangle|\ell,\mu\rangle C(s\ell j;\mu\nu m)$$

where $C(s\ell j;\mu\nu m)$ is the Clebsch-Gordan vector coupling coefficient. Projecting this onto the basis $\langle s',\nu',\mathbf{k}|$, the transformation coefficients between the (ℓ,s,j,m) basis and the $(s',\nu',\mathbf{k})$ basis are

$$\langle s',\nu',\mathbf{k} | \ell,s,j,m \rangle = \sum_{\mu,\nu} \delta_{s,s'} \delta_{\nu,\nu'} C(s\ell j;\mu\nu m) \langle \mathbf{k} | \ell\ \mu \rangle$$

---

30 If the outgoing spins are not observed, one has the special case of averaging over the outgoing spin distribution.

$$= \sum_{\mu,\nu} \delta_{s,s'}\delta_{\nu,\nu'} C(s\ell j;\mu\nu m) i^{-\ell}\, Y_{\ell\mu}(\theta,\varphi)$$

The angles θ and φ refer to the polar and azimuthal angles of the unit vector **k** with respect to some quantization direction **z**, which are taken to be the direction of the incident beam. In order to preserve symmetry with respect to spatial reflections, the spherical harmonic functions $Y_{\ell\mu}(\theta,\varphi)$ are multiplied by the factor i^{ℓ}. The angle-dependent and spin-dependent representation, corresponding to incident directions θ and φ and final directions θ' and φ', is then

$$\mathcal{S}^{j\pi}_{s'\nu',s\nu}(k;\theta',\varphi';\theta,\varphi) = \sum_{j,m}\sum_{\ell,\ell'\mu',\mu}\sum (i)^{\ell-\ell'} C(s'\,\ell'\,j;\,\mu'\nu'm)\, C(s\,\ell\,j;\,\mu\nu m)$$
$$\mathcal{S}^{j\pi}_{\ell's',\ell s}(k)\; Y_{\ell'\mu'}(\theta',\varphi')\; Y^{*}_{\ell\mu}(\theta,\varphi)\,.$$

One has the freedom, except perhaps in a double or triple scattering experiment, to choose $\theta = \varphi = 0$. Furthermore, it is usually the case that the scattered beam is observed only in one plane, according to which one may also set $\varphi' = 0$. Using the definitions of [Tho94] for the spherical harmonics, these particular choices give

$$Y_{\ell\mu}(0,0) = \sqrt{\frac{2\ell+1}{4\pi}}\,\delta_{\mu,0}$$

and

$$Y_{\ell'\mu'}(\theta',0) = (-1)^{\mu'}\sqrt{\frac{(2\ell'+1)(\ell'-\mu')!}{4\pi(\ell'+\mu')!}}\,P^{\mu'}_{\ell'}(\cos\theta') \qquad \text{for } m \geq 0.$$

where $P^{\mu'}_{\ell'}(\cos\theta')$ is the Legendre function. The spherical harmonic for $\mu < 0$ is defined by

$$Y_{\ell\,-|\mu|}(\theta,\varphi) \equiv (-1)^{\mu}\, Y^{*}_{\ell\,|\mu|}(\theta,\varphi).$$

The spin-dependent partial wave expansion for the S–matrix is then

$$S^{j\pi}_{s'\nu',s\nu}(k;\theta',\varphi';\theta,\varphi) =$$

$$\sum_{j,m}\sum_{\ell,\ell'\mu',\mu}\sum (i)^{\ell-\ell'}\sqrt{\frac{2\ell+1}{4\pi}}C(s'\ \ell'\ j;\ \mu'\nu'm)C(s\ \ell\ j;\ \mu\nu m)$$
$$\times \delta_{\mu,0}S^{j\pi}_{\ell's',\ell s}(k)\ Y_{\ell'\mu'}(\theta',0)\ .$$

It is possible to simplify this expression further by taking sums over m, μ' and μ, and by imposing some restrictions implied by the symmetry of the *S*-matrix and the parity-conserving properties of the nuclear interaction.

A.4 The T-matrix

For forward-propagating waves, the Schrödinger equation can be written as

$$i\hbar\frac{\partial}{\partial t'}\left\{ G_0^+(t-t')\psi(t')\right\} = -i\hbar\left\{\frac{\partial}{\partial t'}G_0^+(t-t')\right\}\psi(t') + i\hbar G_0^+(t-t')\frac{\partial}{\partial t'}\psi(t')$$

$$= -\hbar\delta(t-t')\psi(t') + G_0^+(t-t')V\psi(t')\ .$$

After dividing through by $-\hbar$ and integrating both sides of this equation from $t' = -\infty$ to $+\infty$, if the limit at $t' = -\infty$ is chosen so that

$$G_0^+(t-(-\infty))\psi(t-\infty) = \psi_{in}(-\infty),$$

then by definition $\psi(t) = \psi^{(+)}(t)$ is the solution for the full Hamiltonian at time t, and it is given by the integral equation

$$\psi^{(+)}(t) = \phi_{in}(t) + \frac{1}{\hbar}\int_{-\infty}^{t} dt'\ G_0^+(t-t')V\psi^{(+)}(t')\ .$$

The upper limit of the integral is truncated at t, since the forward-propagating Green's function vanishes for negative values of its argument. A similar expression for $\psi^{(+)}(t)$ can be obtained by working through the integral of the partial derivative $i\hbar\frac{\partial}{\partial t'}\left\{ \mathcal{G}^{+}(t - t')\phi(t') \right\}$, where the boundary conditions are chosen so that $\psi(-\infty) = \psi_{in}$. Thus,

$$\psi^{(+)}(t) = \psi_{in}(t) + \frac{1}{\hbar}\int_{-\infty}^{t} dt'\ \mathcal{G}^{+}(t - t')V\psi_{in}(t') .$$

Completely analogous expressions for the backward-propagating solutions can also be obtained.

By the Fourier convolution theorem, the integral is directly expressed in terms of the product of the Fourier transforms of the time-dependent quantities. Hence, one has the time-independent operator equations for the forward (+) and backward (–) propagating solutions to the full interaction Hamiltonian,

$$\psi^{(\pm)}(E,\alpha) = \psi_{\substack{in\\out}}(E,\alpha) + G_0^{(\pm)}(E)V\psi^{(\pm)}(E,\alpha) \qquad (A.3)$$

and

$$\psi^{(\pm)}(E,\alpha) = \psi_{\substack{in\\out}}(E,\alpha) + \mathcal{G}^{(\pm)}(E)V\psi_{\substack{in\\out}}(E,\alpha) . \qquad (A.4)$$

where

$$\psi_{\substack{in\\out}}(E,\alpha) = \int_{-\infty}^{+\infty} dt\ \exp\left\{\frac{iEt}{\hbar}\right\}\psi_{\substack{in\\out}}(t,\alpha),$$

$$\psi(E,\alpha) = \int_{-\infty}^{+\infty} dt\ \exp\left\{\frac{iEt}{\hbar}\right\}\psi(t,\alpha),$$

$$G_0^{(\pm)}(E) = \int_{-\infty}^{+\infty} dt \exp\left\{\frac{iEt}{\hbar}\right\} \exp\left\{ \mp \varepsilon t \right\} G_0^{(\pm)}(t) = (E - H_0 \pm i\varepsilon)^{-1}$$

and

$$\mathcal{G}^{(\pm)}(E) = \int_{-\infty}^{+\infty} dt \exp\left\{\frac{iEt}{\hbar}\right\} \exp\left\{ \mp \varepsilon t \right\} \mathcal{G}^{(\pm)}(t) = (E - H \pm i\varepsilon)^{-1}$$

in which the limit $\varepsilon \rightarrow \pm 0$ is formally taken after all integrations are completed. Equations (A.3) and (A.4) are the Lippmann–Schwinger equations.

Now consider the action of the operator $\mathcal{A} = \Omega^{(+)} - \Omega^{(-)}$ on the arbitrary initial state $\varphi_\alpha(E)$. The operator $\Omega^{(+)}$ transforms it into the forward-propagating solution to the full Schrödinger equation, whereas the operator $\Omega^{(-)}$ transforms it into the solution to the full Schrödinger equation which is will be equal to $\varphi_\alpha(E)$ in the distant future. Therefore,

$$\mathcal{A}\varphi_\alpha(E) = \Omega^{(+)}\varphi_\alpha(E) - \Omega^{(-)}\varphi_\alpha(E) = \psi_\alpha^{(+)} - \psi_\alpha^{(-)} \qquad (A.5)$$

represents a particular solution to the full Schrödinger equation whose boundary conditions are such that, asymptotically, the incident wave from which the first term evolved has been subtracted. The "in" label has been suppressed here, since the label α implies that φ_α and $\psi_\alpha^{(+)}$ converge in the initial state and likewise that φ_α and $\psi_\alpha^{(-)}$ converge in the final state. Operating on equation (A.5) from the left by $\{\Omega^{(-)}\}^\dagger$ generates the transition, or $\mathcal{T}$-operator. This operator maps solutions of the full Schrödinger equation to the solutions of the asymptotic Schrödinger equation into which they will evolve in the far future. The on-shell $\mathcal{T}$-operator is defined by

$$-2\pi i\mathcal{T} \equiv \{\Omega^{(-)}\}^{\dagger}\{\Omega^{(+)} - \Omega^{(-)}\}.$$

It has the following on-shell representations:

$$-2\pi i\mathcal{T}_{\beta\alpha}(E) = \left\langle \varphi_{\beta}(E),\, \mathcal{S}_{\beta\alpha}(E)\varphi_{\alpha}(E) \; - \delta_{\beta\alpha}\varphi_{\alpha}(E) \right\rangle ,$$

and

$$-2\pi i\mathcal{T}_{\beta\alpha}(E) = \left\langle \psi_{\beta}^{(-)}(E),\, \psi_{\alpha}^{(+)}(E) - \psi_{\alpha}^{(-)}(E) \right\rangle .$$

By using the Lippmann–Schwinger equation, it can also be seen that

$$\psi_{\alpha}^{(+)}(E_{\alpha}) - \psi_{\alpha}^{(-)}(E_{\alpha}) = \left(\mathcal{G}^{(+)}(E) - \mathcal{G}^{(-)}(E) \right) V\varphi_{\alpha}(E_{\alpha}) ,$$

so that

$$-2\pi i\mathcal{T}_{\beta\alpha} = \left\langle \left(\left\{ \mathcal{G}^{(+)}(E) \right\}^{\dagger} - \mathcal{G}^{(+)}(E) \right) \psi_{\beta}^{(-)}(E_{\beta}),\, V\varphi_{\alpha}(E_{\alpha}) \right\rangle$$

$$= \left\langle \left((E - H - i\varepsilon)^{-1} - (E - H + i\varepsilon)^{-1} \right) \psi_{\beta}^{(-)}(E_{\beta}),\, V\varphi_{\alpha}(E_{\alpha}) \right\rangle$$

$$= \left\langle \psi_{\beta}^{(-)}(E_{\beta}),\, V\varphi_{\alpha}(E_{\alpha}) \right\rangle .$$

This last set of equalities make use of the identity

$$(x - x_0 \pm i\varepsilon)^{-1} = \mathcal{P}(x - x_0)^{-1} \mp i\pi\delta(x - x_0),$$

where $\mathcal{P}$ is the Cauchy principal value. It can also be shown, by the same method, that

$$\mathcal{T}_{\beta\alpha} = \left\langle \varphi_{\beta}(E_{\beta}),\, V\psi_{\alpha}^{(+)}(E_{\alpha}) \right\rangle .$$

where $E_\alpha = E_\beta$ on the energy shell. The scattering amplitude, $M_{\beta\alpha}$, is related to the $\mathcal{T}$-matrix by

$$M_{\beta\alpha}(E) = -\frac{(2\pi)^2}{k}\,\mathcal{T}_{\beta\alpha}(E).$$

Like the $\mathcal{S}$-matrix, the $\mathcal{T}$-matrix generally depends upon the spin, the orbital angular momentum, the total angular momentum and the total parity, in addition to its dependence on the energy. The same basis states can be used in transforming the scalar $\mathcal{T}$-matrix into the three-dimensional spin dependent representation as were used for the $\mathcal{S}$-matrix in the partial-wave expansion.

APPENDIX B: LONG-RANGE INTERACTIONS

B.1 Introductory remarks

A fundamental assumption of elementary scattering theory is that at some time following the scattering event that is small compared to the time interval between scattering and detection, the wavefunction of the scattered particle converges in the norm to an eigenfunction of the free-field Schrödinger equation. If this assumption is valid, then two principle aims of scattering theory are satisfied. This first is that the radial dependence of the detection probability is purely geometric; i.e., it goes as r^{-2}. The second is that such a system is inherently causal and therefore it is possible to construct a time-independent theory whose operators have well-defined analytic properties. For the purposes of scattering theory, a long-range interaction is one whose scattering solutions violate the convergence condition. Thus, while it is possible to solve the Schrödinger equation for a large class of long-range potentials, it is not possible to describe scattering through these potentials with the formal scattering theory.

In general, the dynamics underlying the long-range interaction are known, so that the wavefunction for the particle scattering solely through the long-range potential is also known. In this case, the scattering through a combination of long and short range interactions can be described using the so-called "two-potential" method. Formally, this method solves the long-range plus short-range problem for all bounded long-range forces and all short-range forces that, in isolation, would give rise to a scattering system as defined in [New82].

The standard two-potential method implicitly describes a system in which all interactions, short and long-range, are binary interactions between the fragments that constitute the initial and final states of the scattering system. If such fragments are truly elementary with respect to the interactions described by the dynamical theory, then the two-potential method solves the scattering problem exactly without modification. In the microscopic few-nucleon theory, however, the short-range forces are

typically nucleon-nucleon interactions, while the asymptotic fragments are nuclei—composite systems of the nucleons between which the elemental forces act. Each such interaction is part of the scattering problem, especially as the final state may represent a re-arranged configuration of the nucleons that comprise the initial state.

The long-range interactions present in realistic nucleus–nucleus scattering problems, of which nucleon–nucleus scattering is a special case, are typically isospin-dependent interactions that, like the short-range forces, act between the constituent nucleons rather than between the projectile and target nuclei. The effect of this combination of long-range and short-range binary interactions is to couple the short and long range forces, generating long-range pseudo-three-body interactions. For example, even at large proton-deuteron separations, the interaction between the neutron and the proton in the deuteron is influenced by the Coulomb interaction between the two protons.

Formally, problems of this nature can be solved also. Specializing to the case of the three-nucleon scattering system with binary Coulomb interactions, Noble has developed a generalized "two-potential" formalism for the Coulomb plus nuclear interaction [Nob67]. This formalism is computationally challenging, however. In addition, it is not clear how to retain an effective range-type description of a system in which every particle degree of freedom is explicitly included.

It has been proposed that the dominance of nucleon exchange in the proton-deuteron interaction at low energies should permit an adequate description of p-d scattering to be obtained by retaining only the leading term in the Coulomb contribution [Ben72, Eyr77]. This contribution consists merely of the usual Coulomb force between the center of mass of the two asymptotic fragments, whose sole manifestation is Coulomb distortion of the relative-motion wavefunction. This approximation is most valid for those states in which the exchange interaction is repulsive; i.e., the spin-quartet even-parity states and the spin-doublet odd-parity states [Eyr77]. For states in which the exchange interaction is attractive, the nucleons may interact at shorter range and hence, the coupling of

electrostatic to nuclear forces is relatively strong. It is therefore clear that the presumption upon which this description is based may falter for the doublet S-wave and quartet P-wave scattering states. In other words, the difference between experiment and a theory which supposes only long-range Coulomb-distortion effects will be most clearly manifest in discrepancies in the ^{2}S and ^{4}P-wave phase shifts.

Recent calculations of the proton-deuteron phase shifts and mixing parameters at a number of energies [Kie94a, Kie94b, Kie95] have included the first correction due to Coulomb distortion of the deuteron. These calculations do not use the Faddeev method, but instead rely on variational solution of the Schrödinger equation. The electrostatic deuteron distortion is required to vanish at infinity. The applicability of this boundary condition within the context of effective range theory, as well as other issues arising from the use of effective range theory in the presence of long-range interactions, is discussed in chapter two.

The remainder of this appendix is devoted to a description of the two-potential formalism under the assumption that Coulomb forces act only between the centers-of-mass of the asymptotic fragments. This special case is of fundamental importance because an effective range theory for short-range forces in the presence of generic long-range interactions is not currently practical. Electrostatic distortion effects in the three-nucleon effective range theory are treated as perturbations of the short-range forces and only two-body Coulomb forces are allowed to act in the asymptotic region. This description is known to fail at threshold [Ben85] but has been shown to give accurate results at experimentally accessible energies [Ben87].

B.2 Nuclear scattering in the presence of static monopole Coulomb forces

In order to evaluate the Coulomb-modified T-matrix, one can formally consider the Coulomb potential as a short-ranged interaction with a sharp cutoff radius, taken in the limit as the cutoff radius goes to infinity. The justification for this procedure is that, in reality, the

Coulomb interaction is screened at large distances by the electron cloud surrounding the nucleus.

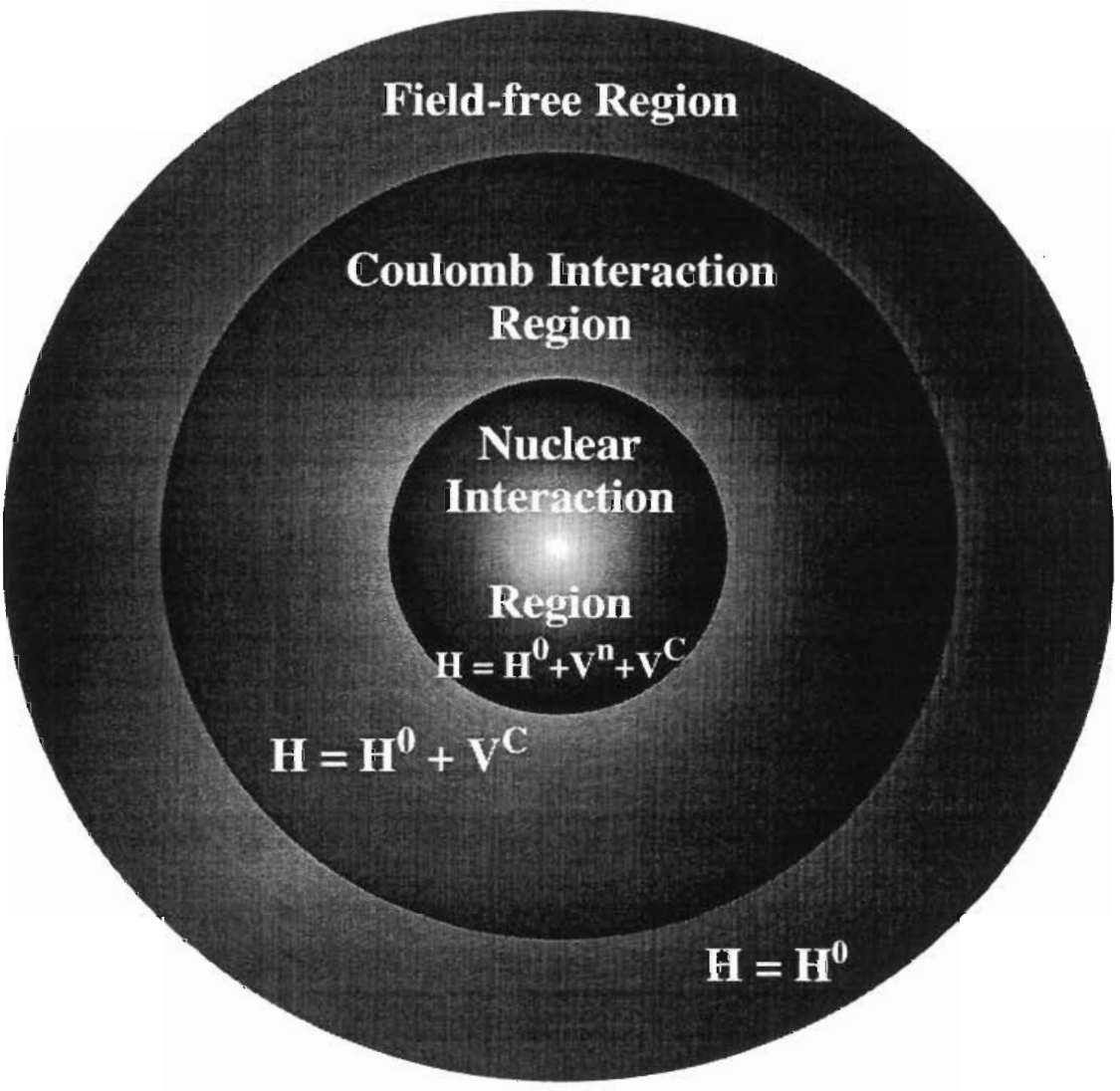

Figure B.1 Schematic diagram of relevant scattering regions for the two-potential problem

One can then construct the problem in the same fashion as for the purely short-range interaction, except that the forward-propagating solution to the Coulomb plus free-wave Hamiltonian, which converges in the remote past to the free-field "in" state, is now the "in" state for the full Hamiltonian. Likewise, the backward-propagating solution to the Coulomb plus free wave Hamiltonian, which converges to the free-field

"out" state, serves as the "out" state for the scattering problem in the nuclear interaction region.

Denoting the Møller operators for the Coulomb interaction relative to the free-field as $\Omega_C^{(\pm)}$ and the Møller operators for the Coulomb modified interaction relative to the Coulomb field as $\Omega_{N,C}^{(\pm)}$, the Møller operators for the full scattering system, $\Omega_F^{(\pm)}$, are

$$\Omega_F^{(\pm)} = \Omega_{N,C}^{(\pm)} \Omega_C^{(\pm)} .$$

Defining a reduced transition operator by $T = -2\pi i \mathcal{T}$, then

$$T_F = \left(\Omega_F^{(-)}\right)^\dagger \Omega_F^{(+)} - \left(\Omega_F^{(-)}\right)^\dagger \Omega_F^{(-)}$$

$$= \left(\Omega_C^{(-)}\right)^\dagger \left(\Omega_{N,C}^{(-)}\right)^\dagger \Omega_{N,C}^{(+)} \Omega_C^{(+)} - \mathbf{I}$$

$$= \left(\Omega_C^{(-)}\right)^\dagger \left(1 + T_{N,C}\right) \Omega_C^{(+)} - \mathbf{I}$$

$$= T_C + \left(\Omega_C^{(-)}\right)^\dagger T_{N,C}\, \Omega_C^{(+)} \quad .$$

where $T_C = \left(\Omega_C^{(-)}\right)^\dagger \Omega_C^{(+)} - \left(\Omega_C^{(-)}\right)^\dagger \Omega_C^{(-)}$

and $T_{N,C} = \left(\Omega_{N,C}^{(-)}\right)^\dagger \Omega_{N,C}^{(+)} - \left(\Omega_{N,C}^{(-)}\right)^\dagger \Omega_{N,C}^{(-)}$.

On the basis of free-field states, the reduced Coulomb-modified nuclear transition operator is

$$T_{\beta\alpha}^{(C,N)}(k) = \left\langle \phi_\beta \middle| \left(\Omega_C^{(-)}\right)^\dagger T_{N,C}\, \Omega_C^{(+)} \middle| \phi_\alpha \right\rangle ,$$

so that the full transition operator is

$$\mathcal{T}_{\beta\alpha}(k) = \mathcal{T}^{(C)}_{\beta\alpha}(k) + \mathcal{T}^{(C,N)}_{\beta\alpha}(k).$$

The first term on the RHS, $\mathcal{T}^{(C)}_{\beta\alpha}(k)$, is the T-matrix attributable to the Coulomb interaction alone. The second term on the RHS, $\mathcal{T}^{(C,N)}_{\beta\alpha}(k)$, is the Coulomb-modified nuclear T-matrix.

To explicitly construct the full $\mathcal{T}$-matrix, the Coulomb $\mathcal{T}$-matrix and phase shift must be determined. The problem is typically solved in the parabolic coordinate system, which is related to the more familiar cylindrical coordinate system by $\xi = r - z$, $\zeta = r + z$; the azimuthal angle φ is the same. Because the Coulomb potential is spherically symmetric, the azimuthal dependence can be separated from the radial dependence. The radial Schrödinger equation is

$$\left[\frac{-4}{\xi+\zeta}\left(\frac{\partial}{\delta\xi}\xi\frac{\partial}{\partial\xi} + \frac{\partial}{\partial\zeta}\zeta\frac{\partial}{\partial\zeta}\right) - \frac{1}{\xi\zeta}\frac{\partial^2}{\partial\varphi^2} + \frac{\eta k}{\xi+\zeta} - k^2\right]\psi^+ = 0\,,$$

where $\eta = \dfrac{Z_1 Z_2 e^2 \mu}{k}$ is the Coulomb parameter and $\mu = \dfrac{m_{proj}\, m_{targ}}{m_{proj} + m_{targ}}$ is the reduced mass.

If one assumes a solution of the form $\psi^+ = e^{ikz} f(\xi)$, then the standard result is that [Abr70]

$$f(\xi) = C_1 F_1(-i\eta; 1; ik\xi)$$

where ${}_1F_1(-i\eta; 1; ik\xi)$ is the confluent hypergeometric function, or Kummer's function, which is regular at $ik\xi = 0$. This solution can be expanded as $|ik\xi| \to \infty$, so that the solution to the Schrödinger equation normalized to unit incident flux is

$$\psi^+ = \left\{\exp(ikz + \eta \ln[k(r - z)])\right\}\left[1 - \frac{\eta^2}{ik(r - z)} + \cdots\right]$$

$$+\frac{\mathcal{A}_C(\theta)}{r}\exp(i[kr-\eta\ln\{2kr\}])\left[1-\frac{(1+i\eta)^2}{ik(r-z)}+\cdots\right]\Bigg\}$$

where

$$\mathcal{A}_C(\theta)=\frac{-\eta}{2k\sin^2\left(\frac{\theta}{2}\right)}\exp(-2i\eta\ln[\sin\left(\tfrac{\theta}{2}\right)]+2i\sigma_0)\ =-\frac{(2\pi)^2}{k}\mathcal{T}_C,$$

is the Coulomb amplitude and

$$\sigma_0=\arg\Gamma(1+i\eta)$$

is the Coulomb S-wave phase shift. This solution does not have the form of a plane wave plus an outgoing spherical wave. This is a consequence of the fact that the Coulomb interaction has an infinite range—both the incident and outgoing waves are distorted by the Coulomb potential for all radial separations.

For sufficiently small observation angles, $r \approx z$ and the series expansion fails to converge. Rapid convergence requires that

$$\left|\frac{\eta^2}{k(r-z)}\right| \ll 1.$$

This is not a problem, though: $|\mathbf{r}-\mathbf{z}| \approx r\sqrt{1-\cos\theta}$, and at energies typical of this experiment, $\frac{\eta^2}{k} < 1$ fm. The typical detection radius is $r \approx 1$ m, so that convergence requires that $\theta \ll 10^{-15}$. This condition is readily met in practice.

If the electron screening radius is taken to be infinite, the distortion of the incident wave induces a Coulomb phase shift of

$$\delta_S=-\eta\ln(2kr),$$

which diverges as $r \to \infty$. If the screening is arbitrarily cut off at some finite radius R_S, then the Coulomb phase shift is

$$\delta_S = -\eta \ln(2kR_S).$$

For finite screening, the Coulomb shift depends upon the radial dependence of the boundary. However, neither the shape of the boundary—whether the cutoff is sharp, exponential, or has some other form—nor the actual value of R_S, is generally known. So long as we are interested only in the nuclear phase shift relative to the Coulomb phase shift, the actual shape and location of the boundary are, to a good approximation, irrelevant. The approximation becomes exact as the wavelength λ becomes very small compared to the screening radius. For a screening radius of roughly $R_S = 0.1$ nm, and typical proton momentum $k \approx 0.08$ fm^{-1}, this condition is fairly well satisfied, since $\frac{\lambda}{R_S} \approx 10^{-4}$.

This all assumes that we don't attempt measurements at very forward angles. In the unscreened "point-Coulomb" model that we use to analyze the data, every particle that is not actually heading away from the target will be scattered by it through some angle. For an infinite-range central potential such as the Coulomb interaction, a large impact parameter translates into small angle scattering, whereas small impact parameters mean large angle scattering.

The comparison of measured to theoretically predicted yield will be compromised if a substantial fraction of particles actually "miss" the target when, according to the fictional "infinite-range" Coulomb potential model, they should have been scattered. The criterion for this effect to be negligible is that $\theta > \frac{2\eta}{kR_S}$ [Lan90]. At energies typical of this experiment, the critical angle is roughly $\theta_C = 0.006°$ so clearly this phenomenon can be neglected.

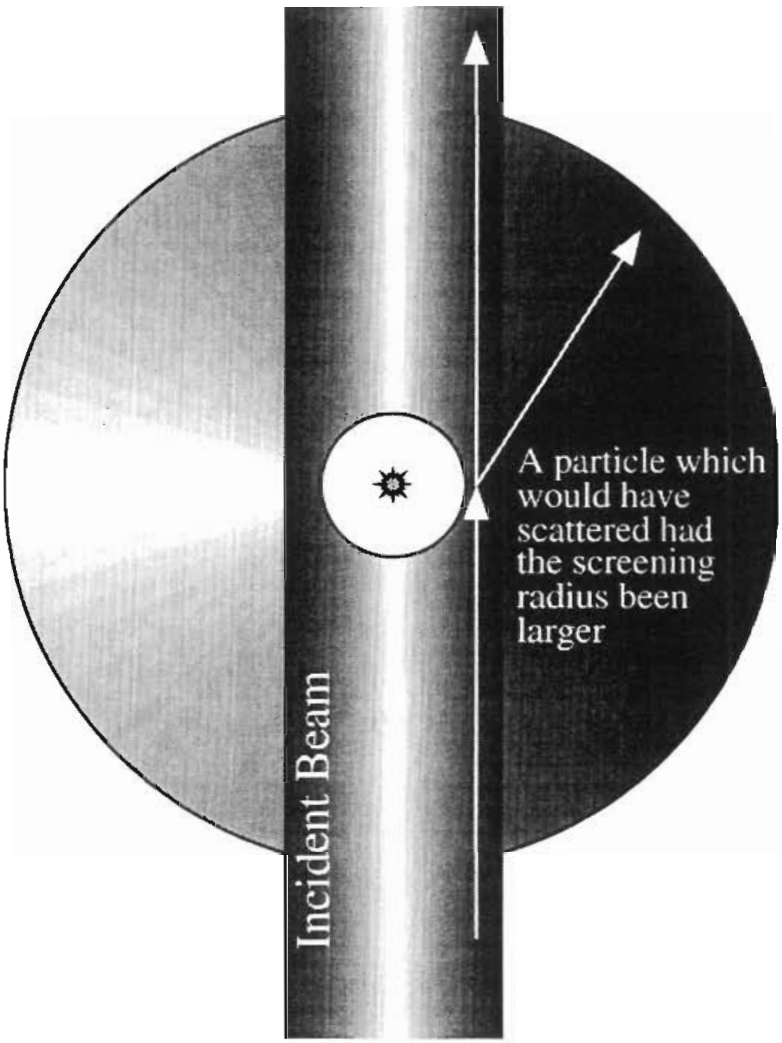

Figure B.2 Diagrammatic representation of the finite-range anomaly for small-angle Coulomb scattering

The Coulomb phase shifts for orbital angular momentum $\ell > 0$ are determined by matching the solution found from solving the Schrödinger equation in parabolic coordinates to a partial wave expansion of the regular solution to the same equation expressed in spherical coordinates. These are found to be [Sch68]

$$\sigma_\ell = \arg\Gamma(\ell + 1 + i\eta) ,$$

in terms of which the partial wave Møller operators are

$$\Omega_{\ell}^{\pm} = \exp(\pm i\sigma_{\ell}).$$

so that the full $\mathcal{T}$-matrix is

$$\mathcal{T}_F = \mathcal{T}_C + e^{i\Sigma}\,\mathcal{T}_{N,C}\,e^{i\Sigma}.$$

where $e^{i\Sigma}$ is the Coulomb Møller operator, whose matrix elements are

$$\langle \ell \mid e^{i\Sigma} \mid \ell' \rangle = \exp(i\sigma_{\ell})\delta_{\ell,\ell'}$$

It is useful to multiply the full $\mathcal{T}$-matrix by the scalar $\exp(-i\sigma_0)$, so that one has, up to an unobservable phase,

$$\mathcal{T}_F = \tfrac{1}{2}(\pi)^{-3/2}\,C(\theta) + e^{iW}\mathcal{T}_{N,C}e^{iW}$$

where

$$C(\theta) = \frac{\eta}{2\sqrt{\pi}\,\sin^2\left(\frac{\theta}{2}\right)}\exp(-2i\eta\ln[\sin\left(\tfrac{\theta}{2}\right)]),$$

and the matrix elements of e^{iW} are

$$\langle \ell \mid e^{iW} \mid \ell' \rangle = \exp(i\omega_{\ell})\delta_{\ell,\ell'}.$$

The Coulomb phase shifts, $\omega_{\ell} = \sigma_{\ell} - \sigma_0$, are easily determined by the recursion formula

$$\omega_{\ell} - \omega_{\ell-1} = \arctan\left(\frac{\eta}{\ell}\right) \quad \text{for } \ell > 0,$$

with $\omega_0 = 0$.

Both coming and going, each Coulomb-modified nuclear wavefunction "surfs" along on the Coulomb wave. Because the Coulomb potential is spherically symmetric and has a convergent partial wave expansion, it is possible to partition the transition matrix and directly extract an angle-dependent term which represents the action of the Coulomb field in the absence of nuclear forces. The Coulomb-modified nuclear phase shifts are *not*, however, the nuclear phase shifts that would be observed absent the Coulomb force. The distortion of the incoming and outgoing wavefunctions by the electrostatic field, represented mathematically by the Coulomb phase shifts, alters the dynamical context in which the nuclear scattering occurs. Only to the extent that such alterations are negligible—at high energy, for example—are the Coulomb-modified nuclear phase shifts a good approximation to the nuclear phase shifts in the absence of electrostatic forces.

APPENDIX C: THE OBSERVABLES IN THE SPIN-1 ⊕ SPIN-1/2 SYSTEM

C.1 The scattering amplitude in the channel-spin basis

It was noted in Appendix A that the dynamically relevant quantum labels for the scattering wavefunction were taken to be the total channel spins s and s′, and total channel orbital angular momentum ℓ and ℓ', coupled to states of definite total angular momentum j and parity π. Theoretical predictions for scattering are therefore given in terms of S-matrix elements expressed in the $(\ell \oplus s) = j^{\pi}$ basis.

It was further noted that particle states could neither be prepared nor detected in such states. Rather, incident particle states are prepared as statistical ensembles of states of definite channel spin and spin projection along an appropriate quantization axis. This is done by selectively populating certain spin states of the incident beam, the target, or both. Likewise, the detection of final-state polarization typically involves taking the expectation value of the final-state wavefunction's spin distribution, integrated over some known spin-dependent interaction.

By contrast, the amplitudes for the various orbital angular momentum components of the initial state are fixed by the presumed boundary conditions and the nature of the nucleon-nucleon interaction. Likewise, no single measurement at a given angle is sufficient to infer the distribution of orbital angular momenta in the final state. The orbital angular momentum ℓ, unlike the channel spin and spin projection, is not an experimental variable. Furthermore, since the absolute orientation of the experiment in space is irrelevant, none of the dynamical quantities occurring in the scattering amplitude depend upon the magnetic sub-state quantum numbers m, which label the projection of the total angular momentum j onto the quantization axis[31]. Therefore, in order to compare experimental observables with theory, the dynamical quantities calculated

---

31 Conventional definitions for the quantization axes in spin-dependent scattering measurements are given in [Mad70].

in the (ℓ,s,j,m) basis[32]; in which the channel orbital angular momentum ℓ and channel spin s are coupled to the total angular momentum j, with projection m along the quantization axis, and parity $\pi = (-1)^{\ell}$; must be re-expressed in the basis (s, ν), where s is the channel spin and ν labels the spin projection along the quantization axis.

Using the definitions of the Coulomb amplitude, Coulomb phase shifts and spherical harmonics given in Appendix A, the scattering amplitude in the (s,ν) representation is therefore

$$\langle s',\nu'|\mathbf{M}|s,\nu\rangle = \frac{\sqrt{\pi}}{k}\Bigg\{ -C(\theta)\,\delta_{s',s}\delta_{\nu',\nu} +$$

$$\sum_{j,m,\ell',\ell,\mu'\mu} (i)^{1+\ell-\ell'}\sqrt{2\ell+1}\; C(s'\;\ell'\;j;\mu'\;\nu'\;m)C(s\;\ell\;j;\mu\;\nu\;m)\delta_{\mu,0}$$

$$\times \exp(2i\{\omega_{\ell'}+\omega_{\ell}\})\left(\delta_{s',s}\delta_{\ell',\ell} - S^{j\pi}_{\ell's',\ell s}(k)\right)Y_{\ell'\mu'}(\theta',0)\Bigg\}. \quad \text{(C.1)}$$

The order of coupling of ℓ and s to j can be chosen arbitrarily, but it is not irrelevant: interchange of the order of coupling introduces a phase factor. Using the symmetries of the 3-j coefficients and their relation with the Clebsch-Gordan coefficients, given in [Tho94], it can be shown that for the spin-$(1\oplus\frac{1}{2})$ scattering system, if the orbital angular momenta in the incident and final states are constrained so that either $\ell' = \ell$, or $\ell' = \ell \pm 2$, then the different coupling schemes are related by

$$C(s'\;\ell'\;j;\nu'\;\mu'\;m)C(s\;\ell\;j;\nu\;\mu\;m) = \Gamma C(\ell'\;s'\;j;\mu'\;\nu'\;m)C(\ell\;s\;j;\mu\;\nu\;m)$$

where

$$\Gamma = \begin{cases} 1 & \text{if } s' = s \\ -1 & \text{if } s' \neq s \end{cases} \quad \text{(C.2)}$$

---

32 The quantum label for the parity is suppressed, since it is implied by ℓ.

The expression for the scattering amplitude given by equation (C.1) can be further simplified by summing over the projection quantum numbers μ, μ', and m. Then

$$\langle s',\nu'|\mathbf{M}|s,\nu\rangle = \frac{\sqrt{\pi}}{k}\Big\{ -C(\theta)\,\delta_{s',s}\delta_{\nu',\nu} +$$

$$i\sum_{j,\ell',\ell}(i)^{\ell-\ell'}\sqrt{2\ell+1}\;C(s'\;\ell'\;j;\,(\nu-\nu')\;\nu'\;\nu)C(s\;\ell\;j;\,0\;\nu\;\nu)$$

$$\times\exp(2i\{\omega_{\ell'}+\omega_{\ell}\})\Big(\delta_{s',s}\delta_{\ell',\ell}-S^{j\pi}_{\ell's',\ell s}(k)\Big)Y_{\ell'\,\nu-\nu'}(\theta',0)\Big\}. \quad (C.3)$$

C.2 The density matrix for the spin $(1 \oplus \frac{1}{2})$ scattering system

The initial-state density matrix ρ_{in} can be decomposed into a sum of spherical tensor operators describing the statistical distribution of spins for an arbitrary initial spin state[33]. The spherical tensor operators satisfy the symmetries of the rotation group implied by the tensor rank of the operator [Tho94]. The decomposition in terms of the spherical tensor operators can be explicitly written as[34]

$$\rho_{in} = \sum_{K,Q} t_{KQ}\mathbf{T}_{KQ}$$

---

33 The significance and utility of spherical tensor operators is not limited to applications in spin-dependent scattering, nor does the present application exhaust thier possibilities even within this sub-discipline. A more complete discussion of the general properties and various applications of spherical tensor operators is found in [Tho94].

34 Unfortunately, the notation prescribed by the Madison convention [Mad70], uses the same symbol "T" to describe the analyzing powers in the spherical basis as the corresponding spherical tensor operators that describe the initial spin state giving rise to these analyzing powers. To minimize confusion, I will use boldface both for the operators and for the elements of the operators as expressed in a particular representation, and will reserve the standard typeface for the analyzing powers.

where the $\mathbf{T}_{KQ}$ are spherical tensor operators of rank K. The index Q labels the elements of the tensor[35]. The coefficients t_{KQ}, called the polarization coefficients, describe the admixture of the spin tensor $\mathbf{T}_{KQ}$ into the spin density matrix.

The spherical tensor operators for a spin-j particle are constructed from the corresponding vector spin operators. Thus, from the Cartesian spin-1 operators:

$$S_x = \frac{1}{\sqrt{2}} \begin{pmatrix} 0 & 1 & 0 \\ 1 & 0 & 1 \\ 0 & 1 & 0 \end{pmatrix},$$

$$S_y = \frac{1}{\sqrt{2}} \begin{pmatrix} 0 & -i & 0 \\ i & 0 & -i \\ 0 & i & 0 \end{pmatrix},$$

$$S_z = \begin{pmatrix} 1 & 0 & 0 \\ 0 & 0 & 0 \\ 0 & 0 & -1 \end{pmatrix},$$

the vector spherical operators are, up to a normalization, equal to the spin-1 operators expressed in the spherical basis. Since

$$S_{\pm 1} = \mp \frac{1}{\sqrt{2}}(S_X \pm iS_Y)$$

and

$$S_0 = S_Z ,$$

the spin-1 spherical spin vectors are [Mad70]

---

35 In general, each element is itself a matrix.

$$\mathbf{T}_{10}^{(1)} = \sqrt{\tfrac{3}{2}}\,S_Z = \sqrt{\tfrac{3}{2}}\begin{pmatrix} 1 & 0 & 0 \\ 0 & 0 & 0 \\ 0 & 0 & -1 \end{pmatrix}$$

$$\mathbf{T}_{11}^{(1)} = \sqrt{\tfrac{3}{2}}\,S_1 = -\sqrt{\tfrac{3}{2}}\begin{pmatrix} 0 & 1 & 0 \\ 0 & 0 & 1 \\ 0 & 0 & 0 \end{pmatrix}.$$

The scalar element, $\mathbf{T}_{00}^{(1)}$, is just the 3×3 identity matrix. Up to a normalizing factor, the second-rank spin-tensors are constructed from the "building-up" formula [Tho94]:

$$\mathbf{T}_{2Q}^{(1)} \propto \sum_{q_1,q_2} \mathbf{T}_{1q_1}^{(1)}\mathbf{T}_{1q_2}^{(1)} C(1\ 1\ 2;\ q_1\ q_2\ Q)$$

so that the second rank spherical tensor operators for spin-1 particles are

$$\mathbf{T}_{20}^{(1)} = \frac{1}{\sqrt{2}}\,(3S_z^2 - 2I_1) = \frac{1}{\sqrt{2}}\begin{pmatrix} 1 & 0 & 0 \\ 0 & -2 & 0 \\ 0 & 0 & 1 \end{pmatrix}$$

$$\mathbf{T}_{21}^{(1)} = \sqrt{\tfrac{3}{2}}\,(S_z\,S_{\pm 1} + S_{\pm 1}\,S_z) = -\sqrt{\tfrac{3}{2}}\begin{pmatrix} 0 & 1 & 0 \\ 0 & 0 & -1 \\ 0 & 0 & 0 \end{pmatrix}$$

$$\mathbf{T}_{22}^{(1)} = \sqrt{3}\,S_1^2 = \sqrt{3}\begin{pmatrix} 0 & 0 & 1 \\ 0 & 0 & 0 \\ 0 & 0 & 0 \end{pmatrix}$$

where the symmetry property

$$\mathbf{T}_{kq} = (-1)^q\,\mathbf{T}_{k-q}^{\dagger}$$

can be used to define the $\mathbf{T}_{k\text{-}q}$.

The proton spherical tensor operators are defined in an analogous manner in terms of the (Cartesian) Pauli matrices

$$\sigma_X = \begin{pmatrix} 0 & 1 \\ 1 & 0 \end{pmatrix},$$

$$\sigma_Y = \begin{pmatrix} 0 & -i \\ i & 0 \end{pmatrix},$$

and

$$\sigma_Z = \begin{pmatrix} 1 & 0 \\ 0 & -1 \end{pmatrix},$$

and the 2×2 identity

$$I_{1/2} = \begin{pmatrix} 1 & 0 \\ 0 & 1 \end{pmatrix},$$

so that the spin-$\frac{1}{2}$ operators in the spherical basis are the identity, $I_{1/2}$, and the three operators:

$$\sigma_{\pm 1} = \mp \frac{1}{\sqrt{2}} (\sigma_X \pm i\sigma_Y)$$

$$\sigma_0 = \sigma_Z ,$$

Then the spin-$\frac{1}{2}$ spherical operators are

$$\mathbf{T}_{00}^{(1/2)} = I_{1/2} = \begin{pmatrix} 1 & 0 \\ 0 & 1 \end{pmatrix}$$

$$\mathbf{T}_{10}^{(1/2)} = \sigma_0 = \begin{pmatrix} 1 & 0 \\ 0 & -1 \end{pmatrix}$$

$$\mathbf{T}_{11}^{(1/2)} = \sigma_1 = -\sqrt{2}\begin{pmatrix} 0 & 1 \\ 0 & 0 \end{pmatrix}$$

and

$$\mathbf{T}_{1\text{-}1}^{(1/2)} = \sigma_{-1} = \sqrt{2}\begin{pmatrix} 0 & 0 \\ 1 & 0 \end{pmatrix}.$$

The spherical spin operators in the coupled channel spin basis are formed from the spin-1 and spin-$\frac{1}{2}$ spherical operators by coupling the spin-1 and spin-$\frac{1}{2}$ basis states to the channel spin states labeled by (s, ν). Since none of the data involve measurements for which both the proton and deuteron were polarized in the incident channel, the deuteron spin-observables are given by

$$\langle s',\nu'|\mathbf{T}_{jk}^{(1\oplus 1/2)}(\vec{d})|s,\nu\rangle = \sum_{m_1',m_1,m_{1/2}} \langle 1,m_1'|\mathbf{T}_{jk}^{(1)}|1,m_1\rangle$$

$$\times C(1,\tfrac{1}{2}\, s';\, m_1' m_{1/2}\nu')\, C(1,\tfrac{1}{2},s;\, m_1 m_{1/2}\nu)$$

and the proton spin-observables are given by

$$\langle s',\nu'|\mathbf{T}_{jk}^{(1\oplus 1/2)}(\vec{p})|s,\nu\rangle = \sum_{m_1,m_{1/2},m_{1/2}'} \langle \tfrac{1}{2},m_{1/2}'|\mathbf{T}_{jk}^{(1/2)}|\tfrac{1}{2},m_{1/2}\rangle$$

$$\times C(1,\tfrac{1}{2}\, s';\, m_1 m_{1/2}'\nu')\, C(1,\tfrac{1}{2},s;\, m_1 m_{1/2}\nu)$$

The non-zero Clebsch-Gordan vector coupling coefficients appearing in these equations, can be readily computed[36]. They are given in Table C.1 below

Table C.1 Non-zero spin-$(1\oplus\frac{1}{2})$ Clebsch-Gordan coefficients

s	m_1	$m_{1/2}$	v	$C(1,\frac{1}{2}\ s;\ m_1,m_{1/2},v)$
$\frac{3}{2}$	1	$\frac{1}{2}$	$\frac{3}{2}$	1
$\frac{3}{2}$	1	$-\frac{1}{2}$	$\frac{1}{2}$	$\sqrt{\frac{1}{3}}$
$\frac{3}{2}$	0	$\frac{1}{2}$	$\frac{1}{2}$	$\sqrt{\frac{2}{3}}$
$\frac{3}{2}$	0	$-\frac{1}{2}$	$-\frac{1}{2}$	$\sqrt{\frac{2}{3}}$
$\frac{3}{2}$	-1	$\frac{1}{2}$	$-\frac{1}{2}$	$\sqrt{\frac{1}{3}}$
$\frac{3}{2}$	-1	$-\frac{1}{2}$	$-\frac{3}{2}$	1
$\frac{1}{2}$	1	$-\frac{1}{2}$	$\frac{1}{2}$	$\sqrt{\frac{2}{3}}$
$\frac{1}{2}$	0	$\frac{1}{2}$	$\frac{1}{2}$	$-\sqrt{\frac{1}{3}}$
$\frac{1}{2}$	0	$-\frac{1}{2}$	$-\frac{1}{2}$	$\sqrt{\frac{1}{3}}$
$\frac{1}{2}$	-1	$\frac{1}{2}$	$-\frac{1}{2}$	$-\sqrt{\frac{2}{3}}$

The symmetry property for the Clebsch-Gordan coefficients upon exchanging the order of coupling is [Tho94]

$$C(j_1\ j_2\ j_{12};\ m_1\ m_2\ m_{12}) = (-1)^{j_1+j_2-j_{12}}\ C(j_2\ j_1\ j_{12};\ m_2\ m_1\ m_{12})$$

from which it is easily deduced that, for the spin-$(1\oplus\frac{1}{2})$ density matrix, the sign of the coupled spin-tensor element changes upon interchange of coupling order if $s' \neq s$, and stays the same if $s' = s$. In the following,

---

36 Algebraic expressions in which the smallest of j_1, j_2 and j_{12} is 1/2 or 1 and numerical expressions for arbitrary values of the arguments, are given for the Clebsch-Gordan coefficients in [Abr72] and for the related 3-J coefficients in [Tho94].

wherever a matrix element has two signs, the upper sign refers to the $(1\oplus\frac{1}{2})$ coupling, and the lower sign refers to the $(\frac{1}{2}\oplus 1)$ coupling.

The deuteron spin-tensors in the channel-spin representation are therefore:

$$\mathbf{T}_{11}(\vec{d}) = \begin{Bmatrix} 0 & -1 & 0 & 0 & (\pm)\frac{1}{\sqrt{2}} & 0 \\ 0 & 0 & -\frac{2}{\sqrt{3}} & 0 & 0 & (\pm)\frac{1}{\sqrt{6}} \\ 0 & 0 & 0 & -1 & 0 & 0 \\ 0 & 0 & 0 & 0 & 0 & 0 \\ 0 & 0 & (\mp)\frac{1}{\sqrt{6}} & 0 & 0 & -\frac{2}{\sqrt{3}} \\ 0 & 0 & 0 & (\mp)\frac{1}{\sqrt{2}} & 0 & 0 \end{Bmatrix}$$

$$\mathbf{T}_{20}(\vec{d}) = \begin{Bmatrix} \frac{1}{\sqrt{2}} & 0 & 0 & 0 & 0 & 0 \\ 0 & -\frac{1}{\sqrt{2}} & 0 & 0 & (\pm)1 & 0 \\ 0 & 0 & -\frac{1}{\sqrt{2}} & 0 & 0 & (\mp)1 \\ 0 & 0 & 0 & \frac{1}{\sqrt{2}} & 0 & 0 \\ 0 & (\pm)1 & 0 & 0 & 0 & 0 \\ 0 & 0 & (\mp)1 & 0 & 0 & 0 \end{Bmatrix}$$

$$\mathbf{T}_{21}(\vec{d}) = \left\{ \begin{array}{cccccc} 0 & -1 & 0 & 0 & (\pm)\frac{1}{\sqrt{2}} & 0 \\ 0 & 0 & 0 & 0 & 0 & (\mp)\sqrt{\frac{3}{2}} \\ 0 & 0 & 0 & 1 & 0 & 0 \\ 0 & 0 & 0 & 0 & 0 & 0 \\ 0 & 0 & (\mp)\sqrt{\frac{3}{2}} & 0 & 0 & 0 \\ 0 & 0 & 0 & (\pm)\frac{1}{\sqrt{2}} & 0 & 0 \end{array} \right\}$$

$$\mathbf{T}_{22}(\vec{d}) = \left\{ \begin{array}{cccccc} 0 & 0 & 1 & 0 & 0 & (\mp)\sqrt{2} \\ 0 & 0 & 0 & 1 & 0 & 0 \\ 0 & 0 & 0 & 0 & 0 & 0 \\ 0 & 0 & 0 & 0 & 0 & 0 \\ 0 & 0 & 0 & (\pm)\sqrt{2} & 0 & 0 \\ 0 & 0 & 0 & 0 & 0 & 0 \end{array} \right\}$$

and the proton spin-tensor is

$$\mathbf{T}_{11}(\vec{p}) = \left\{ \begin{array}{cccccc} 0 & -\sqrt{\frac{2}{3}} & 0 & 0 & (\mp)\frac{2}{\sqrt{3}} & 0 \\ 0 & 0 & -\frac{2\sqrt{2}}{3} & 0 & 0 & (\mp)\frac{2}{3} \\ 0 & 0 & 0 & -\sqrt{\frac{2}{3}} & 0 & 0 \\ 0 & 0 & 0 & 0 & 0 & 0 \\ 0 & 0 & (\pm)\frac{2}{3} & 0 & 0 & \frac{\sqrt{2}}{3} \\ 0 & 0 & 0 & (\pm)\frac{2}{\sqrt{3}} & 0 & 0 \end{array} \right\}.$$

The superscript indicating that these are coupled spin operators has been suppressed.

It is customary that Cartesian, rather than spherical, vector analyzing powers are reported in case the incident proton beam is polarized. The proton Cartesian spin operator, $\mathbf{A}_Y(\vec{p})$, is related to the spherical operator by

$$\mathbf{A}_Y(\vec{p}) = \sigma_Y = \frac{i}{\sqrt{2}}\left(\mathbf{T}_{11}(\vec{p}) + \mathbf{T}_{1-1}(\vec{p})\right).$$

so that

$$\mathbf{A}_Y(\vec{p}) = \begin{Bmatrix} 0 & -\sqrt{\frac{1}{3}} & 0 & 0 & (\mp)\sqrt{\frac{2}{3}} & 0 \\ \sqrt{\frac{1}{3}} & 0 & -\frac{2}{3} & 0 & 0 & (\mp)\frac{\sqrt{2}}{3} \\ 0 & \frac{2}{3} & 0 & -\sqrt{\frac{1}{3}} & (\mp)\frac{\sqrt{2}}{3} & 0 \\ 0 & 0 & \sqrt{\frac{1}{3}} & 0 & 0 & (\mp)\sqrt{\frac{2}{3}} \\ (\pm)\sqrt{\frac{2}{3}} & 0 & (\pm)\frac{\sqrt{2}}{3} & 0 & 0 & \frac{1}{3} \\ 0 & (\pm)\frac{\sqrt{2}}{3} & 0 & (\pm)\sqrt{\frac{2}{3}} & -\frac{1}{3} & 0 \end{Bmatrix}.$$

C.3 Computation of the cross sections and analyzing powers

The expectation values of the spin-polarized scattering cross-sections are obtained by taking the trace of the product of the initial-state spin density matrix ρ_{in} with the square of the scattering amplitude. The spin-dependent cross section is therefore given by

$$\left\langle \vec{\sigma}(\theta) \right\rangle = \frac{\mathrm{Tr}\left\{ \mathbf{M}\rho_{in}\mathbf{M}^{\dagger} \right\}}{\mathrm{Tr}\{\rho_{in}\}}.$$

Since the operators $\mathbf{T}_{KQ}$ are traceless if K and Q are not both equal to zero, the differential cross section is then

$$\sigma(\theta) = \frac{\mathrm{Tr}\left\{\mathbf{M}\mathbf{T}_{00}\mathbf{M}^{\dagger}\right\}}{\mathrm{Tr}\{T_{00}\}} = \frac{1}{6}\mathrm{Tr}\{\mathbf{M}\mathbf{M}^{\dagger}\}$$

and the tensor analyzing powers are

$$T_{KQ} = \frac{1}{6}\mathrm{Tr}\left\{\mathbf{M}\mathbf{T}_{KQ}\mathbf{M}^{\dagger}\right\}.$$

A like expression for the Cartesian analyzing power is

$$A_Y = \frac{1}{6}\mathrm{Tr}\left\{\mathbf{M}\mathbf{A}_Y\mathbf{M}^{\dagger}\right\}.$$

The matrix elements of the scattering amplitude are not all independent. The general reciprocity relation for the scattering amplitude elements in the channel spin representation,

$$\langle \mathbf{k}',s',\nu'|\mathbf{M}|\mathbf{k},s,\nu\rangle = (-1)^{s+s'+\nu+\nu'}\,\langle \mathbf{k},s,-\nu|\mathbf{M}|\mathbf{k}',s',-\nu'\rangle$$

is a consequence of the parity and time-reversal symmetries of the $\mathcal{S}$-matrix [New82]. Using the Clebsch-Gordan symmetry property that

$$C(j_1\, j_2\, j_{12};\, m_1\, m_2\, m_{12}) = (-1)^{j_1+j_2-j_{12}}\, C(j_1\, j_2\, j_{12};\, -m_1\, -m_2\, -m_{12}),$$

and the fact that $(-1)^{2j} = (-1)^{2s'} = (-1)^{2s}$, conservation of parity implies that

$$\langle s',-\nu'|\mathbf{M}|s,-\nu\rangle = (-1)^{s'-s+\nu-\nu'}\,\langle s',\nu'|\mathbf{M}|s,\nu\rangle.$$

Use of this symmetry alone reduces the number of independent matrix elements of the scattering amplitude from 36 to 18. Use of the time-reversal symmetry provides another six equations relating the

matrix elements. However, these equations are not very useful for a number of reasons; they are complicated, and they may provide numerically unstable results depending upon the magnitude of the various matrix elements being related. In the calculations I have incorporated into this work, time-reversal symmetry was not invoked.

The symmetry properties of the Clebsch-Gordan coefficients, referenced throughout this appendix, arise from very general considerations of the transformation of geometric objects in a rotationally invariant space. A detailed treatment is found in [Tho94]. From a group theoretic point of view, the symmetries of the Clebsch-Gordan coefficients can be concisely summarized using the spin and orbital angular momentum spaces as a paradigm. The generators of spin and orbital angular momentum transformations represent covariant and contravariant rotations—active and passive transformations in the Hilbert space, respectively—embedded in a space which is isotropic with respect to real spatial rotations. If the label J is attached to the generator of real spatial rotations, it can be seen that we require that $J = L + S$, which is nothing more than saying that allowed Hilbert space vectors must transform like real space vectors with angular momentum J, under combined transformations in the spin and angle space.

The Clebsch-Gordan coefficients are therefore the elements of the metric that preserve this property under the Hilbert space transformations. If the particles are spinless, then of course $J = L$ and the metric is Euclidean, so that the Clebsch-Gordan coefficients have the form δ_{ij}. The symmetries of the Clebsch-Gordan coefficients arise from the requirement that the Hilbert space vectors rotate like J-vectors in real space under various transformations in L and S space: alternately, they constrain the transformations in L and S space so that the isotropy of J space is preserved. These particular symmetries have nothing to do with the dynamics under consideration; whether, for example, the interaction violates parity conservation or time-reversal symmetry.

It may accidentally be the case, however, that some geometric symmetry associated with the Clebsch-Gordan coefficients has the same

form as a dynamical symmetry or otherwise appears to mimic some dynamical phenomenon. It has already been noted that the order of coupling introduces a non-negligible phase relationship between diagonal and off-diagonal elements for both the scattering amplitudes and the spherical tensor operators that describe spin-dependent scattering.

The unpolarized cross sections are unaffected, but variations in the coupling order may lead to profound changes in the apparent values of the analyzing powers. Every observable has the form

$$O = \sum \langle s,\nu|\mathbf{M}|s',\nu'\rangle \langle s',\nu'|\mathbf{T}|s'',\nu''\rangle \langle s'',\nu''|\mathbf{M}^{\dagger}|s,\nu\rangle$$

where the sum extends over all spin and projection labels. All terms for which $s' = s''$ will be unaffected by changes in the coupling order of either ℓ and s, or the proton and deuteron spins. If $s' \neq s''$, then either $s' = s$, or $s'' = s$. Changing the coupling order of the spin and orbital angular momentum will therefore change the sign of one of the **M** factors but not the other. This sign change is then directly compensated by changing the coupling order of the proton and deuteron spins, which changes the sign of **T** for all the off-diagonal matrix elements. Furthermore, it can be shown that either of these changes in coupling order is equivalent to changing the sign of both the η and ζ mixing parameters, but not that of the ε mixing parameter. This last fact greatly simplifies the comparison of analyses in which different coupling orders were assumed.

APPENDIX D: CHARGE EXCHANGE

In heteronuclear systems—those in which the ionic species and the (atomic) target species are different—the electron capture cross section typically has a single maximum for those energies at which the relative velocity of the ion and target are slightly less than the Bohr velocity of the electron in the target material [Bra92]. As the binding energy of the valence electrons increases, so does the energy at which the maximum is located. On the other hand, since the requirements of energy balance strongly discriminate against capturing an electron from a tightly bound state, the cross section at the maximum for such states is much smaller in general than the cross section for capture from loosely bound atomic states.

The target material can also strip electrons from the projectile. Electrons stripped from the projectile need not be captured into a bound state of the target material. It is sufficient that they be lost into the continuum in such a fashion that it is unlikely that they will re-combine either with the projectile that suffered the loss, or with another projectile.

After transiting a length of material of microscopic—though not atomic—dimensions, an ion may have suffered many hundreds or thousands of atomic collisions. The charge state of the beam is determined by the relative probability of electron loss from and electron capture to the projectile. It is assumed that each such interaction is independent. Furthermore, since the beam can be considered diffuse, the particle is not influenced by the previous passage of other ions.

At ion energies above several tens of keV, the formation of negative ions can be neglected and a simple diffusion equation expresses the positively charged and neutral fraction of the beam at any point in the target along the beampath [Fun93].

$$\frac{1}{\rho}\frac{df^{+}(z)}{dz} = \sigma_l f^{0}(z) - \sigma_c f^{+}(z)$$

where σ_l is the cross section for electron loss, σ_c is the capture cross section , $f^+(z)$ is the positive fraction at penetration z into the target, $f^0(z)$ the neutral fraction, and ρ is the film's atomic density. Under the equilibrium condition, one has $\frac{df^+(z)}{dz} = 0$, and so,

$$\frac{f^+(z)}{f^0(z)} = \frac{\sigma_l}{\sigma_c}$$

A number of experimental determinations of the relative fractions of positive and neutral components of a stripped beam have been conducted for protons (and deuterons) in carbon, as well as in a number of other materials. It has been found that there is no isotopic dependence in the energy range of interest to us, so that the charge fractions depend only on the ion velocity. Therefore, the exit equilibrium charge fractions can be expressed in terms of the variable (E/A) = [Energy/amu] without reference to isotopic identity. Data are somewhat sparse for ion energies between 80 and 200 keV, but those that exist are consistent. A parametric fit to some of these data gives the neutral charge fraction, Φ_0, for atomically clean surfaces [Kre81] as

$$\ln\Phi_0 = a[g(v)]^2 + bg(v) + c$$

where

$$g(v) = \ln(1 + 0.7v^2)$$

The velocity v is in units of the Bohr velocity, $v_0 = 2.19 \times 10^6$ m/s. In terms of the energy, the conversion factors for protons and deuterons are, respectively, $\frac{v_p}{v_0} = 0.1999\sqrt{E}$ and $\frac{v_d}{v_0} = 0.1414\sqrt{E}$ where E is in keV. The constants a, b and c, valid over the energy range of 50 keV to 230 keV, are given in Table D.1 for three target materials.

Table D.1: Fitting coefficients for hydrogen ion neutral charge fraction

Target material	a	b	c
Carbon	–1.07	0.69	4.08
Aluminum	–0.90	0.35	4.17
Gold	–0.23	–0.89	4.70

The authors of [Kre81] noted that the condition of the surface influences the neutral charge fraction. For contaminated surfaces, the neutral charge fraction is independent of the composition of the bulk of the stripper film and is generally lower than for atomically clean surfaces. This observation confirmed the findings of an earlier investigation [Phi55]. Positive, neutral and negatively charged fractions of transmitted hydrogen ions were reported in [Phi55] for a large number of target materials, though not for carbon. Some of these data are abstracted in Table D.2. The stripper foils used in the p–d experiment should be regarded as "contaminated".

Table D.2: Equilibrium charge fractions for hydrogen ions from [Phi55].

Energy [keV]	Contaminated [%]			Aluminum [%]			Gold [%]			Silver [%]		
	+	0	–	+	0	–	+	0	–	+	0	–
10	25.0	72.7	2.3	14.2	81.8	4.0	16.5	80.0	3.5	19.3	78.0	2.8
50	57.0	42.5	0.46	64.0	35.6	0.37	59.5	40.1	0.4	58.3	41.4	0.27
100	79.9	20.0	0.10	87.9	12.0	0.06	80.4	19.5	0.09	81.5	18.4	0.07
150	91.2	8.8	0.02	95.5	4.5	0.04	87.6	13.4	0.05	91.2	8.8	0.02
190	96.0	4.0	—	98.2	1.8	—	91.5	8.5	—	94.5	5.5	—

It is not certain that the stripper foils used in the p–d experiment were thick enough that equilibrium charge fractions were obtained. The equilibrium charge fraction represents an upper limit to the practically attainable positive charge fraction if the incident ions are negatively charged. According to a semi-empirical determination [Bet83], the equilibrium path length z_∞ can be given to within a factor of 3 by the simple linear function

$$z_{\infty} \approx 8 \text{ (E/A)} \text{ [}\mu\text{g/cm}^2\text{]}$$

where (E/A) is MeV/amu. For 200 keV protons, $0 < z_{\infty} < 4.8$ μg/cm^2. The stripper foils used in the Minitandem during the experiment were always less than or equal to 3.0 μg/cm^2 in thickness. This might explain a couple of "anecdotal" observations. The first is that the analyzed positive fraction has seemed to be "larger" when thicker stripper foils have been used. Also, it has been observed that stripper foils may become "weak" over time, that is, they lose potency even though no punctures or tears in the film are apparent. It may well be the case that as the collodion coating which is used to strengthen the carbon film is burned off in the beam, the resulting foil is so thin that the equilibrium charge state is not achieved.

APPENDIX E: STATISTICAL INFERENCE

E.1 Bayes' Theorem

A fundamental canon of the Bayesian statistical theory is the definition of probability as a measurable degree of belief in the truth of an assertion. This implies a particular interpretation of the associative hypothesis for conditional probabilities,

$$P(A|\,B) = \frac{P(B|\,A)\,P(A)}{P(B)}\,. \qquad (E.1)$$

The interpretation may be read as, "the probability (measurable degree of belief) assigned to assertion A conditional on the certain truth of assertion B, is equal to the probability of assertion B conditional on the certain truth of assertion A times the probability that assertion A is true, divided by the probability that assertion B is true."

For the case wherein A refers to an hypothesis—which may have the form of a set or vector of parameters describing a state of nature—and B refers to a set of experimental data that are relevant in assessing the validity of A, special names are used to refer to the various factors in equation (E.1). The factor P(A) is termed the prior probability of A, or just "the prior" and P(B) is called "the evidence". The factor P(B| A), denoted "the likelihood", is most often taken from a model of the physical process, although one can sometimes utilize empirical distributions in case it is possible to acquire knowledge of the dependence of B on specific choices of A. P(B| A) is also chosen in many cases for the convenience of the analyst. The appropriateness of this type of choice depends critically on the nature of the phenomenon under investigation. P(A|B), called the posterior probability, or just "the posterior", is then the probability of the truth of hypothesis A, given the data B.

Equation (E.1) completely specifies the inferential problem. To have solved it for all A it to have extracted the maximum amount of information contained in the data B. It is generally not necessary to do

this, however. It is usually sufficient to solve it for some statistically relevant observable related to the distribution of P(A| B). This can be the mean or the mode of P(A| B), as well as some measure of the uncertainty in the identification of the statistic with a nominal value—typically the variance is given.

The most common modern method of finding a reportable solution to equation (E.1) is to use a gradient search computer routine to find the modal value A of the distribution P(A| B). "Pure" gradient search routines do not actually find the mode of P(A| B), but rather locate the local minimum of the χ^2 distance between the data and simulations of the data calculated using the various possible values of the hypothesis A, which usually has the form of a set of parameters for the assumed form of the distribution P(B| A). The word "local" in this context refers to the stationary point in the parameter space nearest to the starting point of the search. For this reason, gradient searches are often critically dependent upon the given starting values of the parameters used to generate the simulated data. More sophisticated hybrid routines temper this difficulty by initially performing Monte Carlo sampling of the χ^2 space to locate promising regions for undertaking a more directed search.

The χ^2 statistic is a quadratic score function[37] [Ber94] whose absolute minimum represents the point in parameter space wherein the simulated data are statistically indistinct from the observed data. Note that the absolute minimum may or may not be a point. It may be a compact region in χ^2 space, or even a set of disjoint regions. The absolute minimum of χ^2 might not actually be found within the allowed search range of the parametric variables, either because the search range is excessively restricted, or because the chosen parametric form does not adequately represent the physical model describing the data sample.

Because gradient searches rely on finding the local "direction of steepest descent", it must be possible for the code to rapidly calculate the local derivative of the χ^2 function with respect to variations in the

---

37 Also called a quadratic loss function.

hypothesis. Furthermore, the number of allowed variational parameters may be restricted. MINUIT, the fitting program in use at TUNL, permits no more than 32 free parameters to be varied.

E.2 Substitution sampling

The "substitution algorithm" is a well-known technique for solving certain types of integral equations [Gel90]. The Born series solution to the Lippmann-Schwinger equation is a well-known example. The eventual convergence of this algorithm, which involves successive substitution into the equation of the results of the previous iteration of the substitution series, depends upon the properties of the integral kernel and not, in general, upon the initial estimate used to initiate the series, presuming that the initial estimate is a "reasonable" solution to the equation. Many iterations can be eliminated and convergence thereby accelerated, by choosing initial solutions that are believed to be as near as possible to the true solution of the integral equation.

A version of the substitution algorithm applicable to probability functions was developed by Tanner and Wong, who demonstrated its utility in solving various types of inference problems, including those arising from incomplete data [Tan87]. A statement of the substitution algorithm is as follows:

Let $P(\theta|\mathbf{Y})$ be the probability of a parametric vector θ conditional on a data vector $\mathbf{Y}$ and $P(\mathbf{Y}|\theta)$ be the probability of $\mathbf{Y}$ conditional on θ. Let $P(\theta)$ and $P(\mathbf{Y})$ be the marginal distributions of θ and $\mathbf{Y}$. According to the definition of marginal probabilities,

$$P(\theta) = \sum_{\{\mathbf{Y}\}} P(\theta|\mathbf{Y})\, P(\mathbf{Y}) \qquad \text{(E.2)}$$

and

$$P(\mathbf{Y}) = \sum_{\{\theta\}} P(\mathbf{Y}|\theta)\, P(\theta). \qquad \text{(E.3)}$$

Substitution of (E.3) into (E.2) gives

$$P(\theta) = \sum_{\{\mathbf{Y}\}} P(\theta|\mathbf{Y}) \sum_{\{\theta'\}} P(\mathbf{Y}|\theta') P(\theta') \qquad \text{(E.4)}$$

One can solve this equation iteratively, denoting, for example, the m^{th} iterative approximation of $P(\theta)$ as $P_{(m)}(\theta)$, so that

$$P_{(m)}(\theta) = \sum_{\{\mathbf{Y}\}} P(\theta|\mathbf{Y}) \sum_{\{\theta'\}} P(\mathbf{Y}|\theta') P_{(m-1)}(\theta') \qquad \text{(E.5)}$$

Suppose now that the data set **Y** is not complete, in the sense that the true aim of the experiment that yields **Y** is to extract information regarding some degree of freedom to which the detection apparatus is insensitive. This degree of freedom might be, for example, the spin of an outgoing particle, or it might be the identity of the reaction that produced the detected particle.

Such a latent data vector **Z** was not actually observed but it is presumed that one can somehow formulate a probability law, which need not be expressible in closed form, that determines the conditional probability $P(\mathbf{Z}|\mathbf{Y})$ of observing the vector **Z**, given that the vector **Y** was actually observed. Assuming that the probability of observing the latent data set **Z** is some function of a parametric vector φ, a complete solution to the inference problem, given data **Y**, consists of determining the conditional probability distribution $P(\varphi|\mathbf{Y})$.

The general case discussed in [Tan87] conceives of **Z** as a data set that *augments* **Y**, so that a complete data set consists of **Y** and **Z** jointly. In the spectral analysis problem posed by the p–d experiment, it turns out that **Z** *supplants* **Y**, so that **Y** is a well-defined, though as yet unspecified function of **Z**; $\mathbf{Y} = f(\mathbf{Z})$. A connection between the two conceptions is readily established by considering the latent data of [Tan87] as a set of data **W** that, jointly with **Y**, uniquely determines and is determined by the latent data **Z** of this work. The derivation presented in the following generally follows that of Tanner, but is specific to the case of interest,

wherein **Y** is a projection of **Z** onto some particular subspace. The result does not depend, however, upon the distinction noted above, since the mapping between the joint vector (**W**,**Y**) of [Tan87] and the vector **Z** of this work is isomorphic.

In contrast to the algorithm of equations (E.2) – (E.5), conditional, rather than marginal, probabilities are to be sampled. An expression for the solution, the probability $P(\varphi|\mathbf{Y})$ that φ is the true parameter vector, given the observed data **Y**, is

$$P(\varphi|\mathbf{Y}) = \sum_{\{\mathbf{Z}'\}} P(\varphi|\mathbf{Z}')\, P(\mathbf{Z}'|\mathbf{Y})\,, \qquad \text{(E.6)}$$

and the probability of observing **Z** given **Y** is

$$P(\mathbf{Z}|\mathbf{Y}) = \sum_{\{\varphi'\}} P(\mathbf{Z}|\varphi',\mathbf{Y})\, P(\varphi'|\mathbf{Y})\,. \qquad \text{(E.7)}$$

Substitution of (E.7) into (E.6) gives

$$P(\varphi|\mathbf{Y}) = \sum_{\{\mathbf{Z}'\}} P(\varphi|\mathbf{Z}') \sum_{\{\varphi'\}} P(\mathbf{Z}'|\varphi',\mathbf{Y})\, P(\varphi'|\mathbf{Y}), \qquad \text{(E.8)}$$

which can be iteratively solved as in equation (E.5).

Convergence of the algorithm depends upon the specific properties of the transformation kernel,

$$K_{\mathbf{Y}}(\varphi,\varphi') = \sum_{\{\mathbf{Z}'\}} P(\varphi|\mathbf{Z}')\, P(\mathbf{Z}'|\varphi',\mathbf{Y})\,.$$

Besides being bounded and continuous, it is required that there exists an open neighborhood of every point in the parameter space such that whenever φ and φ' inhabit that neighborhood, the kernel is positive, which means only that it is non-vanishing, since the factors are both non-negative. A sufficient, though not necessary, condition for this criterion is to require both factors in the kernel equation to be everywhere positive

in the allowed event space, which can generally be arranged. In order to ensure the existence of an open neighborhood about each point in the parameter space, it is sufficient to exclude the boundary of the space from consideration. More general conditions are discussed in [Tan87].

Given that these readily satisfied criteria on the transition kernel are met, the following convergence result obtains: Let $G(\varphi) = P(\varphi|\mathbf{Y})$ be the true posterior distribution of the parameter vector φ conditional on the data $\mathbf{Y}$ and let $G_{(m)}(\varphi)$ be the m^{th} iteration of equation (E.8). Then given that $G(\varphi)$ is non-vanishing[38], $G_{(m)}(\varphi)$ converges linearly in the mean to the true posterior distribution $G(\varphi)$; e.g.,

$$\|G_{(m+1)}(\varphi) - G(\varphi)\| \leq \alpha^m \|G_{(0)}(\varphi) - G(\varphi)\| \qquad (E.9)$$

for some constant $0 < \alpha < 1$.

This algorithm is called the "data augmentation algorithm". The solution, equation (E.6), requires calculating the full conditional distribution of the latent data $\mathbf{Z}$, via (E.7). An estimated distribution can be calculated by means of Monte Carlo sampling, but for cases in which the number of plausible sets of latent data $\mathbf{Z}$ are large, even an estimated distribution of this nature is impossibly time-consuming to generate.

Equations (E.6) – (E.8) can be re-written with the conditional dependence on the true data suppressed, so that

$$P(\varphi) = \sum_{\{\mathbf{Z}'\}} P(\varphi|\mathbf{Z}')\, P(\mathbf{Z}')\,, \qquad (E.10)$$

$$P(\mathbf{Z}) = \sum_{\{\varphi'\}} P(\mathbf{Z}|\varphi')\, P(\varphi')\,, \qquad (E.11)$$

and

---

38 This is tantamount to requiring that the problem is meaningful; i.e., the parameters are actually sensitive to the data.

$$P(\varphi) = \sum_{\{\mathbf{Z}'\}} P(\varphi|\mathbf{Z}') \sum_{\{\varphi'\}} P(\mathbf{Z}'|\varphi')\, P(\varphi') \,. \qquad \text{(E.12)}$$

The m^{th} iteration of equation (E.12) is then

$$P_{(m)}(\varphi) = \sum_{\{\mathbf{Z}\}} P(\varphi|\mathbf{Z}) \sum_{\{\varphi'\}} P(\mathbf{Z}|\varphi')\, P_{(m-1)}(\varphi') \,. \qquad \text{(E.13)}$$

Nothing essential has been changed, since none of the expressions involve a predictive probability for $\mathbf{Y}$.

First, draw one sample of the complete set $\varphi^{(0)}$ from the marginal distribution $P(\varphi)$. Next draw the vector $\mathbf{Z}^{(1)}$ from $P(\mathbf{Z}|\varphi^{(0)})$. Then sample the vector $\varphi^{(1)}$ from $P(\varphi|\mathbf{Z}^{(1)})$. Comparison of the samples performed in this first cycle with equation (E.13) reveals that $\varphi^{(1)}$ is a sample from $P_1(\varphi)$. Repeating the cycle again yields a vector $\varphi^{(2)}$ drawn from $P_2(\varphi)$. After n such cycles, one samples a vector $\varphi^{(n)}$ from the distribution $P_n(\varphi)$ that, according to the convergence result expressed in equation (E.9), is closer to the true posterior distribution than was the original by at least a factor of α^n, where α is between zero and one.

This iterative scheme is called the substitution sampler algorithm. It is not completely satisfactory, because it requires drawing complete parametric vectors φ and $\mathbf{Z}$ on every cycle. The conditional distribution $P(\varphi|\mathbf{Z})$ that appears in the spectral analysis problem cannot reasonably be sampled that way, because of the difficulty of numerically evaluating the distribution. Only some form of acceptance/rejection sampling method is practical. However, since the dimensions of both φ and $\mathbf{Z}$ are very large, sampling the complete vectors is inefficient, since the rejection rate is likely to be very large. It is preferable to sample each element of φ and $\mathbf{Z}$ separately, conditional on all the others. A variation of the substitution sampler that permits this freedom is the Gibbs Sampler.

E.3 The Gibbs Sampler

Suppose that the parameter vector ζ consists of the K elements of φ and the L elements of **Z**, so that ζ is a J = (K+L)-dimensional vector. The solution to the inference problem consists of determining the distribution $P(\zeta)$, where the conditional dependence on the vector **Y** has been suppressed. Starting with an initial vector whose elements are given by the set $(\zeta_1^{(0)}, \zeta_2^{(0)}, \zeta_3^{(0)}, \ldots, \zeta_J^{(0)})$, and whose joint density is given by $P(\zeta_1^{(0)}, \zeta_2^{(0)}, \zeta_3^{(0)}, \ldots, \zeta_J^{(0)})$, each component can be sampled according to the following scheme:

$$\zeta_1^{(1)} \sim (\zeta_1 | \zeta_2^{(0)}, \zeta_3^{(0)}, \ldots, \zeta_J^{(0)})$$

$$\zeta_2^{(1)} \sim (\zeta_2 | \zeta_1^{(1)}, \zeta_3^{(0)}, \ldots, \zeta_J^{(0)})$$

$$\vdots$$

$$\zeta_J^{(1)} \sim (\zeta_J | \zeta_1^{(1)}, \zeta_2^{(1)}, \ldots, \zeta_{J-1}^{(1)})$$

At the end of m such cycles, one obtains a sample from the joint density $P(\zeta_1^{(m)}, \zeta_2^{(m)}, \zeta_3^{(m)}, \ldots, \zeta_J^{(m)})$.

It was shown by Geman and Geman that under appropriate conditions the density $P(\zeta^{(m)}|\mathbf{Y})$ converges to the true posterior distribution $P(\zeta^{(\text{true})}|\mathbf{Y})$ as $m \rightarrow \infty$ [Gem84]. Moreover, it was shown in [Gel90] that under the requirement that each site was visited on every repetition, the Gibbs sampler was formally equivalent to the J-dimensional substitution sampler. This implies that one can invoke the simple requirements stated in [Tan87] to assure convergence. An important property of the Gibbs sampler transition operator T_G, implicitly defined by

$$P(\zeta^{(m+1)}|\mathbf{Y}) = T_G(\zeta^{(m+1)}, \zeta^{(m)}) P(\zeta^{(m)}|\mathbf{Y}) ,$$

is that it is a Markov operator. This means that neither the asymptotic rate of convergence, nor the fact of convergence itself, depend upon the initial parameter vector $\zeta^{(0)}$.

REFERENCES

[Abr72] M. Abramowitz and I. A. Stegun, *Handbook of Mathematical Functions* (Dover Publications, New York, 1972).

[Adh82] S. K. Adhikari and J. R. A. Torreão, Phys. Lett. 119B, 245 (1982).

[Ajz87] F. Ajzenberg–Selove, Nucl. Phys. A475, 1 (1987).

[Alb83] S. Albeverio, D. Bollé, F. Gesztesy, R. Høegh–Krohn and L. Streit, Ann. Phys. 148, 308 (1983).

[And77] H. H. Andersen and J. F. Ziegler, *Hydrogen Stopping Powers and Ranges in All Elements* (Pergamon Press, New York, 1977).

[And79] L. P. Andersson, S. Berg, N. Norström and R. Olaison, Thin Solid Films, 63, 155 (1979).

[Arv74] J. Arvieux, Nucl. Phys. A221, 253 (1974).

[Ben72] Gy. Bencze, Nucl. Phys. A196, 135 (1972).

[Ben85] Gy. Bencze and C. Chandler, Phys. Lett. 163B, 21 (1985)

[Ben87] Gy. Bencze, C. Chandler, J. L. Friar, A. G. Gibson and G. L. Payne, Phys. Rev. C35, 1188, (1987).

[Ber65] R. O. Berger and L. Spruch, Phys. Rev. 138, B1106, (1965).

[Ber86] G. H. Berthold and H. Zankel, Phys. Rev. C34, 1203 (1986).

[Ber94] J. M. Bernardo and A. F. M. Smith, *Bayesian Theory* (John Wiley & Sons, Chichester, (1994).

[Bet83] H. D. Betz, *Heavy Ion Charge States* in *Applied Atomic Collision Physics, Vol. 4*, ed. S. Datz, (Academic Press, New York, (1983).

[Bla49] J. M. Blatt and J. D. Jackson, Phys. Rev. 26, 18 (1949).

[Bla52] J. M. Blatt and L. C. Biedenharn, Rev. Mod. Phys. 24, 258 (1952).

[Bla93] T. C. Black, B. E. Hendrix, E. R. Crosson, K. A. Fletcher, H. J. Karwowski and E. J. Ludwig, Nucl. Instr. Meth. A333, 239 (1993).

[Bol85] D. Bollé, F. Gesztesy and W. Schweiger, J. Math. Phys. 26, 1661 (1985).

[Bra92] B. H. Bransden and M. R. C. McDowell, *Charge Exchange and the Theory of Ion–Atom Collisions* (Clarendon Press, Oxford, 1992).

[Bru95] C. R. Brune, Triangle Universities Nuclear Laboratory internal report, (1985).

[Che86] C. R. Chen, G. L. Payne, J. L. Friar and B. F. Gibson, Phys. Rev. C33, 401 (1986).

[Che89] C. R. Chen, G. L. Payne, J. L. Friar and B. F. Gibson, Phys. Rev. C39, 1261 (1989).

[Che91] C. R. Chen, G. L. Payne, J. L. Friar and B. F. Gibson, Phys. Rev. C44, 50 (1991).

[Chr53] R. S. Christian and J. L. Gammel, Phys. Rev. 91, 100 (1953).

[Cle95] T. B. Clegg, H. J. Karwowski, S. K. Lemieux, R. W. Sayer, E. R. Crosson, W. M. Hooke, C. R. Howell, H. W. Lewis, A. W. Lovette, H. J. Pfutzner, K. A. Sweeton and W. S. Wilburn, Nucl. Instr. Meth. A357, 200 (1995).

[Del58] L. M. Delves, Nucl. Phys. 8, 358 (1958).

[Del60] L. M. Delves, Phys. Rev, 118, 1318 (1960).

[Des94] L. Deshayes, M. Charbonnier, M. Romand, T. Petit, N. Chevarier and A. Chevarier, Thin Solid Films 241, 264 (1994).

[Dil71] W. Dilg, L. Koester and W. Nistler, Phys. Lett. B36, 208 (1971).

[Efi88] V. Efimov and E. G. Tkachenko, Few-Body Systems 4, 71 (1988).

[Eks56] H. Ekstein, Phys. Rev. 101, 880 (1956).

[El-H88] F. M. El–Hossary, D. J. Fabian and C. J. Sofield, Thin Solid Films, 157, 29 (1988).

[Eyr77] D. Eyre, A. C. Phillips and F. Roig, Nucl. Phys. A275, 13 (1977).

[Fle93] K. A. Fletcher, Ph.D. Thesis, University of North Carolina at Chapel Hill, 1993. (unpublished). Available from University Microfilms International, Dissertation Services, Box 58, 300 N. Zeeb Rd. Ann Arbor, Michigan 48106–1346.

[Fri83] J. L. Friar, B. F. Gibson and G. L. Payne, Phys. Rev. C28, 983 (1983).

[Fri84] J. L. Friar, B. F. Gibson, G. L. Payne and C. R. Chen, Phys. Rev. C30, 1121 (1984).

[Fri90] J. L. Friar, B. F. Gibson, G. L. Payne and C. R. Chen, Phys. Lett. B247, 197 (1990).

[Fun93] H. O. Funsten, B. L. Barraclough and D. J. McComas, Nucl. Instr. Meth. B80/81, 49 (1993).

[Gal82] J. L. Gallant and P. Dmytrenko, Nucl. Inst. Meth. 200, 1 (1982).

[Gel90] A. E. Gelfand and A. F. M. Smith, J. Amer. Stat. Assoc. 85, 398 (1990).

[Gem84] S. Geman and D. Geman, IEEE Trans. Patt. Anal. Mach. Intelligence 6, 721 (1984).

[Gib88] B. F. Gibson and B. H. J. McKellar, Few Body Systems, 3, 143 (1988).

[Has70] W. K. Hastings, Biometrika 57, 97 (1970).

[Hol78] L. Holland, Vacuum 28, 437 (1978).

[Hol79] L. Holland and S. M. Ojha, Thin Solid Films 58, 107 (1979).

[Hüc81] B. Hück, E. Jaeschke, W. Kratschmer, R. Repnow and H. Wirth, Nucl. Instr. Meth. 184, 215 (1981).

[Hut83a] E. Huttel, W. Arnold, H. Berg, H. H. Krause, J. Ulbricht and G. Clausnitzer, Nucl. Phys. A406, 435 (1983).

[Hut83b] E. Huttel, W. Arnold, H. Baumgart, H. Berg and G. Clausnitzer, Nucl. Phys. A406, 443 (1983).

[Kar90] V. F. Karchenko, M. A. Navrotsky and S. A. Shadchin, Nucl. Phys. A512, 294 (1990).

[Kar93] V. F. Karchenko, M. A. Navrotsky and P. A. Katerinchuk, Nucl. Phys. A552, 378 (1993).

[Ker87] D. B. Kerwin, I. L. Spain and R. S. Robinson, Thin Solid Films 148, 311 (1987).

[Kie94] A. Kievsky, M. Viviani and S. Rosati, Nucl. Phys. A577, 511 (1994).

[Kie95a] A. Kievsky, Few Body Systems Suppl. 99, 1 (1995)

[Kie95b] A. Kievsky, M. Viviani and S. Rosati, private communication.

[Kre81] S. Kreussler and R. Sizmann, Phys. Rev. B26, 520 (1981).

[Lan44] L. Landau and J. Smorodinsky, J. Phys. U.S.S.R. 8, 154 (1944).

[Lan90] R. H. Landau, *Quantum Mechanics II*, (Wiley–Interscience, New York, (1990).

[Lan58] A. M. Lane and R. G. Thomas, Rev. Mod. Phys. 30, 257 (1958).

[Lea82] J. Leavitt, P. W. Rathmann, S. Shojaee and S. Bashkin, Nucl. Inst. Meth. 202, 349 (1982).

[Len90] W. N. Lennard, S. Y. Tong, G. R. Massoumi and L. Wong, Nucl. Instr. Meth. B45, 281 (1990).

[Lev90] F. S. Levin, in *Trends in Theoretical Physics, Vol. 1*, ed. P. J. Ellis, Y. C. Tang (Addison–Wesley, New York, 1990).

[Mad70] *Proc. of the Third Int. Symp. on Polarization Phenomena in Nucl. Reactions*, Madison, WI, 1970. ed. H. H. Barschall, W. Haeberli (Univ. of Wisconsin Press, 1971).

[Mak69] L. M. Makosky and C. Hojvat, Nucl. Inst. Meth. 74, 342 (1969).

[Mar67] J. B. Marion and B. A. Zimmerman, Nucl. Inst. Meth. 51, 93 (1967).

[Mey76] H. O. Meyer, G. R. Plattner and I. Sick, Z. Physik A279, 41 (1976).

[Mey77] H. O. Meyer, G. R. Plattner and I. Sick, Z. Physik A282, 240 (1977).

[Mey94] H. O. Meyer, private communication.

[Mey80] B. S. Meyerson and F. W. Smith, J. Non-Crystalline Sol. 35/36, 435 (1980).

[New82] R. G. Newton, *Scattering Theory of Particles and Waves* (Springer–Verlag, New York, 1982).

[Nob67] J. V. Noble, Phys. Rev. 161, 945 (1967).

[Phi77] A. C. Phillips, Rep. Prog. Phys. 40, 905 (1977).

[Phi55] J. A. Phillips, Phys. Rev. 97, 404 (1955).

[Pou86] J. J. Pouch, S. A. Alterovitz and J. D. Warner, Mat. Res. Soc. Symp. Proc. Vol. 68., 211 (1986).

[Rei69] A. S. Reiner, Phys. Lett. B28, 387 (1969).

[Rev93] D. Revelle, L. Mulestagno, S. Lin and B. J. Feldman, Sol. State Comm. 86, 235 (1993).

[Sch47] J. Schwinger, Phys. Rev. 72, 742A (1947).

[Sch68] L. I. Schiff, *Quantum Mechanics* (McGraw–Hill, New York, 1968).

[Sey69] R. G. Seyler, Nucl. Phys. A124, 253 (1969).

[Sof82] C. J. Sofield, C. J. Woods, N. E. B. Cowern, L. B. Bridwell, J. M. Butcher and J. M. Freeman, Nucl. Instr. Meth. 203, 509 (1982).

[Tai80] N. R. S. Tait, D. W. L. Tolfree, P. John, I. M. Odeh, M. J. K. Thomas, M. J. Tricker and J. I. B. Wilson, Nucl. Instr. Meth. 176, 433 (1980).

[Tai81] N. R. S. Tait, Nucl. Instr. Meth. 184, 203 (1981).

[Tan87] M. A. Tanner and W. H. Wong, J. Am. Stat. Soc. 82, 528 (1987).

[Tan91] K. Tanaka, M. Okada, T. Kohno, M. Yanokura and M. Aratani, Nucl. Instr. Meth. B58, 34 (1991).

[Tei51] T. Teichmann, Phys. Rev. 83, 141 (1951).

[Tei52] T. Teichmann and E. P. Wigner, Phys. Rev. 87, 123 (1952).

[Tho92] W. J. Thompson, Comp. in Phys. 6, 386 (1992).

[Tho94] W. J. Thompson, *Angular Momentum* (Wiley–Interscience, New York, 1994).

[Tho95] W. J. Thompson, private communication.

[Tol82] D. W. L. Tolfree, Nucl. Instr. Meth. 200, 15 (1982).

[Tom87] L. Tomio, A. Delfino and S. K. Adhikari, Phys. Rev. C35, 441 (1987).

[Uhr85] M. Uhrmacher, K. Pampus, F. J. Bergmeister, D. Purschke and K. P. Lieb, Nucl. Instr. Meth. B9, 234 (1985).

[Van67] W. T. H. Van Oers and K. W. Brockman, Nucl. Phys. A92, 561 (1967).

[Whi79] D. S. Whitmell, B. H. Armitage, D. W. L. Tolfree and N. R. S. Tait, Nucl. Instr. Meth. 159, (1979).